Diffuse reflectance endoscopic imaging for bladder early-stage cancer and pre-cancer diagnosis: instrumentation, modelling and experimental validation

Nina Kalyagina

Ecole doctorale IAEM Lorraine
DFD Automatique et Production Automatisée
Université de Lorraine

Аспирантура Института Общей Физики им. А. М. Прохорова
Российская Академия Наук

A. M. PROKHOROV GENERAL PHYSICS INSTITUTE RUSSIAN ACADEMY OF SCIENCES

Diffuse Reflectance Endoscopic Imaging for Bladder Early-Stage Cancer and Pre-Cancer Diagnosis: Instrumentation, Modelling and Experimental Validation

THESIS

Defended on 30 March 2012 ('behind closed doors')

for receiving the

Doctoral Degree of University of Lorraine at the speciality:

Automatic Control, Computing and Signal Processing

and

Candidate Degree on Physics and Mathematics of Prokhorov General Physics Institute of Russian Academy of Sciences at the speciality:

Laser Physics

by

Nina KALYAGINA

Jury composition:

Reviewers:	**Rudolf Steiner**	UU, Ulm, Germany
	Fabrice Mériaudeau (Jury President)	IUT – Le2i, Le Creusot, France
Examiners:	**Victor Loshchenov** (Thesis Director)	GPI RAS, Moscow, Russia
	Didier Wolf (Thesis Director)	CRAN, Nancy, France
	Ismaël Didelon	SD-Innovation, Frouard, France
	Walter Blondel (Thesis Co-Director)	CRAN, Nancy, France
Invited:	**Christian Daul**	CRAN, Nancy, France
	François Guillemin	CAV, Nancy, France

Centre de Recherche en Automatique de Nancy
UMR 7039 Nancy-Universite - CNRS
2 av. de la foret de Haye, 54516 Vandoeuvre-les-Nancy, France

A. M. Prokhorov General Physics Institute of Russian Academy of Sciences
Vavilov Str. 38, 119991, Moscow, Russia

NSC GPI RAS

This thesis was performed within the international cooperation of two Institutions: A. M. Prokhorov General Physics Institute of Russian Academy of Sciences (GRI PAS), in the Laser Biospectroscopy Laboratory of the Natural Sciences Center, and University of Lorraine, in the Center of Research on Automation of Nancy (CRAN).

Foremost I would like to express my gratitude to my thesis supervisors Prof. Victor Loschenov, and Prof. Didier Wolf for giving me the opportunity to realize this thesis, for providing me with a stimulating atmosphere, and for being my advisors during all my studies.

I would like to thank also my thesis co-supervisor Prof. Walter Blondel, and Prof. Christian Daul for their guidance, advices and assistance.

I also thank a Junior Research Scientist of the Laser Biospectroscopy Laboratory of the GPI RAS Tatiana Savelieva for many useful suggestions and support.

I am gratefully acknowledging all members of the two laboratories have been helpful and supportive during this project.

I would like to express my gratitude to the thesis reviewers Prof. Rudolf Steiner and Prof. Fabrice Mériaudeau for their acceptance being experts of my thesis.

And I give special thanks to my family and friends, encouraging me during all my studies ☺!

"In my sleep I thought today that the shortest expression of the meaning of life might be this: the world moves, perfects itself; the main task of man is to take part in this movement, to submit himself to it, and to help it."

L. N. Tolstoy

.

Table of Contents

List of Figures

List of Tables

Publications and Conference Papers

International Journal Articles

1. N. Kalyagina, V. Loschenov, D. Wolf, C. Daul, W. Blondel, T. Savelieva**, "**Experimental and Monte Carlo investigation of visible diffuse reflectance imaging sensitivity to diffusing particle size changes in an optical model of a bladder wall", Applied Physics B, vol.105(3), pp. 631-639, 2011.
2. Savelieva T.S., Ryabova A.V., Andreeva I.V., Kalyagina N.A., Konov V.I. and Loschenov V.B., "Combined spectroscopic method for determining the fluorophore concentration in highly scattering media", Bulletin of the Lebedev Physics Institute, 38(11), pp. 334-338, 2011.

International Articles in Conference Proceedings

Tatiana A. Savelieva, Nina Kalyagina, Maria Kholodtsova, Aleksandr Potapov, Sergey Goryainov, Victor B. Loschenov, "Numerical modelling and in vivo analysis of fluorescent and laser light backscattered from glial brain tumours", SPIE Proceedings, BiOS Photonics West conference, 2012.

International Conference Papers

1. N. Kalyagina, W. Blondel, C. Daul, T. Savelieva, D. Wolf and V. Loschenov, "Diffuse-reflectance spectroscopic and imaging diagnostic methods for urinary bladder", 19th International Conference on Advanced Laser Technologies – 2011 p. 38-39.
2. N. Kalyagina, T. Savelieva, V. Loschenov, W. Blondel, C. Daul, D. Wolf, "Analytical Study of Surface Diffuse-Reflectance Signals From Thin Biological Media", Saratov Fall Meeting – 2011 (online version).
3. Tatiana Savelieva, Nina Kalyagina, Maxim Loschenov, "Quantification of structural and biochemical changes in glial tumors with multimodal spectroscopic measurements and multispectral visualization", Saratov Fall Meeting – 2011 (online version).
4. N.A. Kalyagina, V.B. Loschenov, D. Wolf, C. Daul, W. Blondel, "Experimental investigation of Diffuse Reflectance Imaging sensitivity to diffusing particle size changes in an optical model of Bladder Mucosa", 18th International Conference on Advanced Laser Technologies – 2010 p. 55.
5. N. A. Kalyagina, V. B. Loschenov, D. Wolf, C. Daul, W. Blondel, "Experimental investigation and mathematical modeling of diffuse-reflectance in thin biological layers", Saratov Fall Meeting – 2010 (online version).
6. N.A. Kalyagina, V.B. Loschenov, C. Daul, D. Wolf, W. Blondel, "Development of a Light Diffusion Investigation Method in Thin Layers of Biological Tissues", International Symposium on Laser Medical Applications – 2010 p. 121-122.

National Conference Papers

N.A. Kalyagina, V.B. Loschenov, K. V. Rodionov, D. Wolf, W. Blondel, C. Daul, "Diffuse-Reflection Signals from nano- and micro- scattering particles on the phantoms of the Urinary Bladder", Russian Biotherapeutical Journal № 4, vol. 9 - 2010, p. 16 (in russian).

Participation in Conferences

International Conferences

1. SPIE Photonics West conference (San Francisco, USA) – 2012 (oral).
2. International Conference on Advanced Laser Technologies (Varna, Bulgary) – 2011(oral).
3. Saratov Fall Meeting (international school for young scientists on optics, laser and bio physics) (Saratov, Russia) – 2011 (oral).
4. International Conference on Advanced Laser Technologies (Egmond-aan-Zee, the Netherlands) – 2010 (oral).
5. International Symposium on Laser Medical Applications (Moscow, Russia) – 2010 (oral).
6. Saratov Fall Meeting (international school for young scientists on optics, laser and bio physics) – 2010 (Saratov, Russia) (oral).

National Conferences

National Conference on Nanotechnologies in Oncology (Tumen, Russia) – 2010 (oral).

Awards

Second award in “Best Young Scientist” competition of the 19th International Conference on Advanced Laser Technologies 2011.

INTRODUCTION

The health care side of the human being has taken the leading position in the life since ancient times, being the integral part of the qualitative life. Modern medical progress has considerably increased the average lifetime. Nowadays, most of clinical equipment can be hardly imagined without video systems (allowing to perform internal operations), laser jets (making it possible to diagnose at early stages of disease), and mathematical treatment (providing and speeding up results processing). The variety of clinical diagnostic and therapeutic techniques for bladder cancer [1-6] highlights the interest of the medical community to improve the quality of the diagnostic methods. Thereby, the global aim of the present work is to contribute to the improvement of biomedical systems, allowing for a non-invasive diagnosis of bladder cancerous and pre-cancerous tissues.

Clinical instruments are mostly based on optical systems and measure principles that suits to specific medical problems. Among the most popular in biomedical optics analytical and therapeutic methods are laser-based technologies, which are widely used at physics, biology, medicine and inter-disciplinary fields. Lasers can be implemented in different technical devices, diagnostics and research measurements and studies. Such a wide need of optical and laser systems makes the biomedical optics [7], [8] to be one of the main promising spheres to develop and improve.

The targets of the biomedical optical studies are biological molecules, cells and their components, intercellular matrices and tissues at macroscopic level [9], [10]. However, the complexity of biological tissues and of modifications, occurring in them under cancer formation, involves many diagnostic problems into biomedical optics that still have to be solved.

Laser light interaction with biological tissues can provide information on their structure characterizing its state at cellular, multicellular and molecular level. A laser wave, penetrated into a medium, changes its direction and intensity in a unique way due to unique tissue morphology: density and structure, absorption and concentration of the scattering elements inside the tissue. Light distribution in the tissue (or on its surface) can provide diagnostically useful information [11]. Thereafter, the optical techniques, based on the biological tissue interaction with the laser light are of considerable interest for *in vivo* diagnosis. This interest

formed one of main aims of this thesis - to detect early-cancerous tissue changes by analysis of surface back-scattered light signals.

Six chapters of the thesis are constructed to cover a wide range of important problems, relating to early cancer detection. They present a biomedical method of DR laser light analysis and its mathematical modelling for multi-layered media.

Motivations and problems of the optical laser diagnosis of bladder tissues are described in Chapter 1 of this thesis. Multi-layered structure of the bladder wall, and common tissue modifications under cancerous neoplasm formation are analysed. Main sub- and inter- cellular changes in bladder mucosa at dysplasia formed the “markers” for the surface light responses analysis. They also motivated us for multi-layers phantoms construction, mimicking five different states of bladder urothelium, by varying their scattering and absorption parameters. The principles of light-tissue interaction, namely reflection, absorption and scattering, and main features, advantages and disadvantages of modern optical diagnostic techniques, based on tissue-light interaction, are also discussed in the Chapter 1. This part of the thesis serves as a starting point for the development of an analytical method for detection and processing of diffuse-reflected (DR) light from bladder tissues and phantoms.

Chapter 2 represents an experimental part of this thesis. It describes an imaging method of *in vivo* measurements of surface back-scattered laser signals. In the first part of the Chapter 2 the sensitivity of the presented method to the sizes of the scattering particles in multi-layered phantoms was studied, and the most suitable and fast image processing algorithms were found. The second part of this Chapter describes five different types of multi-layered phantoms constructed in order to reveal the surface light signal dependence on different changes of the tissue. Furthermore, the presented technique was tested on the capability to discriminate the fluorescent signals from tissues with different level of the photosensitizer accumulation.

Mathematical analysis of the scattering process, occurring during the tissue-light interaction with bladder tissue and tissue-like models, is described in Chapter 3. Two computational approaches, based on the Mie theory [12], for calculations of tissue optical parameters are presented. The first approach describes the interaction of electromagnetic waves with spherical particles, the second one - with “coated spheres”. After the computation and literature analysis, tables with optical parameters for three layers of the biological phantoms and bladder tissues at five different states were composed.

Chapter 4 describes a stochastic mathematical approach (Monte Carlo method [13-15]) for modelling the light distributions of back-scattered light distribution on the surface of multi-layered media. Basing on the optical parameters, presented in the Chapter 3, the matrices of the light distributions on the surface of the phantoms and bladder tissue with different scattering parameters of the first layers were obtained. The results of matrices processing and analysis were compared with the experimental ones.

The clinical studies of the back-scattered laser and fluorescent light signals on the surface of healthy and pathological bladder tissues are described in Chapter 5. Mathematical estimations of scattering tissue parameters for the case of multi-wavelength excitation analysis are also presented.

Conclusions and future application of the method of detection and analysis of the surface DR laser light signals for pre-cancerous or early-stage cancerous bladder tissues are presented in Chapter 6. The main drawbacks and advantages are discussed.

References:

[1] Ohigashi T., Kozakai N., Mizuno R., Miyajima A., Murai M., Endocytoscopy: novel endoscopic imaging technology for in-situ observation of bladder cancer cells, J Endourol; 20 (9):698–701, 2006.

[2] Koljenovic S., B. Schut T. C., Wolthuis R., de Jong B., Santos L., Caspers P. J., and Puppels G. J., Tissue characterization using high wave number Raman spectroscopy. J Biomed Opt; 10:031116, 2005.

[3] Zysk A. M., Oldenburg A. L., Marks D. L., Nguyen F. T., Boppart S. A., Optical coherence tomography: a review of clinical development from bench to bedside. J Biomed Opt;12:051403, 2007.

[4] Wang Z., Lee C. S., Waltzer W. C., Liu J., Xie H., Yuan Z., Pan Y., In vivo bladder imaging with microelectromechanical-systems-based endoscopic spectral domain optical coherence tomography. J Biomed Opt;12(3): 034009, 2007.

[5] Burger M, Zaak D, Stief CG, Filbeck T, Wieland WF, Roessler W, Denzinger S.. Photodynamic diagnostics and noninvasive bladder cancer: is it cost-effective in long-term application? A Germany-based cost analysis. Eur Urol; 52(1): 142–7, 2007.

[6] Mitra AP, Cote RJ, Molecular pathogenesis and diagnostics of bladder cancer, Annu Rev Pathol.;4:251-85, 2009.

[7] Wang L. V. and Wu H., Biomedical optics: principles and imaging, Wiley and sons, New Jersey, 2007.

[8] Tuchin V. V. (ed.), Handbook of optical biomedical diagnostics, SPIE, Washington, 2002.

[9] Faretta M., Schue A., From Molecules to Tissues: Optical Tools for Cancer Research imaging & Microscopy, Vol. 10, Issue 1, pp. 44–46, 2008.

[10] Backman V., Gurjar R., Badizadegan K., Itzkan I., Dasari R. R., Perelman L. T., and Feld M. S., Polarized Light Scattering Spectroscopy for Quantitative Measurement of Epithelial Cellular Structures In Situ, IEEE Journal of Selected Topics in Quantum Electronics, Vol. 5, No. 4, 1999.

[11] Backman V. and Wax A. in Biomedical applications of light scattering by A. Wax and V. Backmann (eds), The McGraw-Hill Companies, US, 2010.

[12] Bohren C., Huffman D.: Absorpttion and scattering of light by small particles, John Wiley & Sons, New-York, 1998.

[13] Prahl S. A., Keijzer M., Jacques S. L. and Welch A. J., A Monte Carlo model of light propagation in tissue, Proc. SPIE 5, 102-111, 1989.

[14] Flock S. T., Wilson B. C., Wyman D. R. and Patterson M. S., Monte Carlo modeling of light propagation in highly scattering tissues – I: model prediction and comparison with diffusion theory, IEEE Trans. Biomed. Eng. 36, pp. 1162-1168, 1989.

[15] Jacques S. L. and Wang L.-H., Monte Carlo modeling of light transport in tissues, in: Optical thermal response of laser irradiated tissue, A. J. Welch and L. G; C. van Gemert (edts), plenum press, N.Y. pp. 73-99, 1995.

1

CHAPTER

Posing a Problem: Neoplasm Formation and Optical Diagnosis

"Have no fear of perfection - you'll never reach it."

S. Dali

1.1 Introduction

To form the base for the thesis, we first review some basic concepts of pathology formation in bladder epithelium. The optical diagnostic techniques, using the effects of tissue-light interactions, will also be introduced in this chapter. One of the most important fields of laser medical application is biomedical optics, where the laser light is often used for diagnostics, therapy, surgery procedures or prophylactic purposes. The essential aim of the optical diagnostic techniques is to detect the lesions at the early stage of disease, when the microscopic changes begin to occur in tissues. Such precise information about tissue state at a microscopic level can be revealed by the tissue biopsy, which is, however, an invasive method, and sometimes is taken randomly [1], [2]. Besides, such procedure often requires a waiting period of several hours to days. Due to the possible differences at the malignancy level of the tumour under investigation, the biopsy from one area of a lesion cannot be representative of the state of the entire lesion. Thus some of the malignant lesions can be overlooked [3]. Large neoplasms often require multiple biopsies, which leads to substantial tissue removal. The resemblance of tissue inflammation to pre-malignant mucosal alterations [4] often leads to random or repeated biopsies causing a strong discomfort to the patient. However, even though the optical techniques have limitations in diagnosing, especially at the early stages of neoplasm formation, they have a strong potential to be both, non-invasive and sensible enough to detect changes at the micrometric scale. With such advantages, optical techniques can be applied for *in vivo* determination of the tissue optical parameters [5].

One of the purposes of this thesis is to understand (by experimental studies and mathematical modelling), whether our optical diagnostic method of analysis of the surface diffuse reflection (DR), can be a non-invasive diagnostic imaging. The method is based on the irradiation of a tissue by a narrow collimated coherent laser beam, and collection of a surface back-scattered non-polarized light signal by a photodetector. A similar technique is described in [6], where the authors measured spatially resolved reflectance distribution for bladder and brain tissues *in vivo*. Their results of experimental studies and mathematical modelling show that the method and its mathematical simulation allow for determining the optical properties

of a tissue and may be applied for internal organs, such as urinary bladder (UB). In practice, this is implemented with the use of the laser light supplied by an optical fibre to the tissue, and analysis of the signal, acquired through the cystoscopic optical channel connected to a video camera. In this thesis we propose an optical non-invasive method, aiming to increase the specificity of the diagnostics by detecting different cellular and intercellular changes of the bladder epithelium. It is supposed that the proposed laser system and the analytical method can be used for biopsy navigation, or applied without the biopsy need for *in vivo* detection of the cancerous multifocal tissue neoplasms. Biological cells consist of different sub-structures (organelles) in a fluid (cytosol). The largest organelle is cell with its typical sizes of about 10-15 μm for the bladder tissue [7]. Each organelle has specific structure and role to play in the function of the cell and tissue in general.

Precancerous lesions of the UB mostly arise in the first, epithelial layer, which consists of 4-7 rows of densely-packed orbicular-shaped cells [8], and is about 200 μm thick. At a normal state each cell of the transitional epithelium has a nucleus of about 5-7 μm diameter. However, at the early stages of UB diseases, such as dysplasia, first metamorphoses occur in the cell nuclei, which influence the cell optical properties.

At dysplasia the cell nuclei undergo different changes [9], which contribute to the light scattering and absorption properties of the tissue. Thereafter the wave interaction with the epithelial layers at different stages of neoplasm formation, should be taken into a special consideration, and will be discussed below. The tissue scatterers are all the components of the biological tissue, influencing different scattering properties. Thus the impact of each scatterer on the tissue light distribution should be studied to understand whether it should be taken into account or not. Besides the biggest scatterer (nucleus), all the smallest cell organelles of about 20-100 nm contribute to the light diffusion in tissues. Such small cell organelles are, for example, endoplasmatic reticulum, component parts of Golgi apparatus, individual fibres, and less small organelles, as mitochondria, lysosomes and Golgi apparatus, which sizes can be compared to the wavelength of a visible light.

The scattering process is caused by the optical inhomogeneities, which are different in their shape and nature. The media with distinctive optical inhomogeneities are known as turbid media. In the visible-infrared wavelength range almost all the biological tissues are turbid media. The character of the light scattering depends primarily on the ratio of the wavelength and the size of scattering particles [10]. If the ratio of the linear dimensions of the scattering of particles smaller than 1/15 of the wavelength, then the scattering on such a

particle is called Rayleigh scattering. For large particle sizes, comparable to the wavelength, the scattering is called Mie scattering. Under the Rayleigh scattering the initial direction of the light is almost completely disrupted, while under the Mie scattering the direction of the light propagation is largely preserved. However, in that case the collimated beam becomes fuzzy and spreads to different directions inside the tissue. Penetrating inside a medium, the light is reflected, absorbed and scattered, thus it is partially backscattered or transmitted through the medium [11]. Light propagation in biological tissue is determined to have a greater degree of scattering process than of absorption process. It is noted that wider beams penetrate deeper into the tissue than the narrow beams.

The interaction of electromagnetic radiation with matter can be a many-sided process. Typically, there are three major effects that can interfere with free light diffusion: reflection and refraction, absorption and scattering. The relation between the reflection and refraction processes can be expressed by the Fresnel laws, which gives subject to classify them into one category of the processes. Due to absorption and scattering, it is difficult to control and detect the effect of refraction in the turbid media. Photons, neither reflected nor absorbed or scattered, pass through the media and contribute to the intensity of the transmitted light measured at the opposite side of the sample. The amount of reflected, absorbed and scattered light depends on the optical properties of the media and on the wavelength of the incident radiation, which is one of the most important parameters in the optical studies. The wavelength specifies the absorption and scattering coefficients and the index of refraction, determining the total reflectivity of the media.

Due to the multiple scattering and absorption, the laser beam changes its shape and intensity during the propagation in the tissue. The spatial scattering causes the spread of a significant proportion of the radiation in the opposite direction (back scattering). The absorbed light is converted into the heat, reemits as fluorescence or phosphorescence, or is spent to the photo-biochemical reactions. In the laser medicine, the knowledge of absorbing and scattering properties of the tissue, is important for a successful diagnosis or treatment. As the biological objects are usually complex and heterogeneous structures, various approximations are used to describe the interaction of the radiation light with the tissue. Below the above processes are discussed in a more detailed way.

1.2 Basic Concepts of Light Propagation into a Biological Medium

1.2.1 Reflection

In general, three main photophysical processes appear with light propagation in biological tissues: refraction, scattering and absorption [10]. As it was mentioned above, penetrating into the biological tissue, light can be reflected from the boundary of the medium, be absorbed by the tissue, and scattered on the tissue irregularities. Reflection is a process of return of the electromagnetic radiation from the surface on which it falls. Reflection of the incident wave from the surface of the medium occurs due to the difference of tissue optical properties (relating to the refractive index) between two media [12]. The refractive index depends on the nature of the medium, temperature, wavelength of the incident light and density. Even if this dependence is very weak in the visible range, it should be considered for an accurate understanding of light distribution in the tissue.

1.2.2 Absorption

In biomedical optics, another important outcome from the light interaction with a tissue is absorption. Absorption offers both diagnostic and therapeutic possibilities. The changes in the absorption properties lead to changes in the light distribution inside the tissue, providing valuable information for a diagnosis. It can also allow a laser or other light source to cause a curing or damaging (for cancer cells for example) effect on a tissue.

Absorption of the light photons is a consequence of the partial transition of the electromagnetic light energy into another form of energy, like thermal motion or vibration of the molecules [13]. The absorption occurs in a case of resonance caused by the concurrency of the oscillation frequencies of particles in the medium with the oscillation frequency of the incident wave. The ratio of the absorbed and incident intensities characterises the absorption capacity of the medium. Due to the absorption process, the intensity of the incident electromagnetic wave is attenuated while passing through the medium. When the energy of light penetrated into a medium is equal to the transmitted one, the media is considered to be

non-absorbing. And in opposite, the structures, in which the incident electromagnetic irradiation is almost completely attenuated, are highly-absorbing and scattering turbid media [11]. As the absorbing properties depend on the wavelength, one media can be transparent at one particular wavelength range, and, at the same time, highly absorbing at another one. In the case of white light (visible range of the wavelengths), the absorbing medium, independent of both, the wavelength (at a certain range) and the absolute temperature, appears black (when the absorption coefficient is about or equal to 1) or grey (when the absorption coefficient is less than 1). This behaviour arises due to the constant reduction on the same amount of signal intensity at all the wavelength region. In contrary, in case of selective absorption, when the magnitude of the white light is changed by non constant values, the surface of a body appears colourful, determining the reflectance properties and the penetration depth of the light inside the medium. The standard estimations of the penetration depth reflect the distance from the surface to a certain point, where the light intensity has reduced by the Euler's number. Typically for the bladder wall, visible laser light penetrates to a depth of 0.5 mm to about 2 mm [14].

In general, the capability to absorb the electromagnetic radiation is unique for each biological tissue, as it depends on many factors: internal tissue structure, concentration and of the type of absorbing centers, wavelength, thickness of the absorbing media, temperature and chemical composition. The optical absorption in biological tissues can be due to endogenous molecules such as haemoglobin or melanin, or exogenously delivered contrast agents. Common tissue chromophores absorb the light of ultraviolet (UV), visible and infrared (IR) wavelength regions [15], [16], [10]. In biological tissues the absorption in the visible-nearinfrared range is mainly performed by the water molecules and different biochromes. Thus, the colour of the pigments is determined by the presence of chromophoric groups, selectively absorbing the light in certain wavelengths. Examples of substances with such properties are porphyrins and porphyrin-like structures, which include biological pigments of porphyrin complex. Heme, a type of porphyrine, is a part of the prosthetic group and of compounds like haemoglobin, cytochrome, and others. Melanin is synthetized in melanocytes [17] and is the main pigment of the skin. It is also the main chromophore of the epidermis.

Another pigment of biological tissue is chromatin, which is always present at the nucleus. Due to the absorbing properties of the deoxyribonucleic acid (DNA) and the protein complex of which chromatin consists, it can be well-coloured by the basic alkaline dyes. In

histological images chromatin appears in the form of a dense substance inside the cell nucleus. During the mitotic cell division, chromatin condenses and takes the shape of spiral, forming the chromosomes. During the nuclear inactivation a progressive condensation of chromatin appears, and in opposite, in the activated nuclei the proportion of diffuse chromatin increases. Most of the studies on absorption properties of the bladder tissue revealed higher absorption in the cancerous tissue in comparison with normal tissues at the wavelength of visible range [18], [19]. For example, at the cancerous and pre-cancerous tissue states, the concentration of chromatin and total blood content grow [20], which can be reflected in the light distribution, and thus can be used for tissue diagnostics.

1.2.3 Scattering

Light scattering is an important process in the biomedical optics field. Such light-tissue interaction process is characterized by the process of redirection of light that occurs when an incident electromagnetic wave comes into collision with an obstacle or inhomogeneity. During such a collision the mismatch in the frequencies of the particle and those of the incident wave provokes changes in light spatial distribution [11], frequency and polarization. The phase and the speed of the wave differ from the ones of the incident wave so that the speed decreases after penetration of the wave into a denser medium. Under elastic scattering scattered light is emitted at the identical frequency of the incident light. Elastic scattering is commonly used in spectroscopy of biological tissues [21], [22]. It arises in biological tissues due to the presence of different cell components, extracellular structures (such as collagen elastin fiber networks), as well as intracellular structures (such as nuclei, mitochondria, Golgi apparatus, and other organelles) [23]. The properties of the scattered light depend also on the density of scattering particles, the particle size, and the ratio of the particle and medium refractive indices. Due to such variations in the biological scatterers, the scattered light wave becomes incoherent and unpolarized during its penetration into the tissue.

After multiple scattering some of the photons return back to the surface of the tissue under the random angles. Such light, which can be detected on the surface of the tissue, is called diffusely reflected light. Depending on the tissue properties, the proportions of such light may vary.

1.2.4 Fluorescence

Fluorescence analysis is based on the influence of light on the biological tissue with a photosensitive component. Most of the sensitizers have a singlet ground state. Fluorescence effect, induced by the laser light interaction with most of the sensitizers, corresponds to the emitting transition of electrons of photosensitizer molecules. This transition starts from the lowest singlet vibrational level of the excited state S_1 (in case of singlet transition), and finishes in the ground state S_0 (Fig. 1.1), which the molecule leaved after being excited by the absorbed light quantum. Usually the fluorescent spectra are located in the area of longer wavelengths in comparison to the wavelength of the excitation light. This phenomenon is due to a loss of the absorbed energy for the radiationless transitions from vibration levels of the excited state.

The fluorescent light generated by the emitting transition is commonly used for biomedical diagnostics. Such diagnostics are non-invasive, which is one of the most important advantages of the fluorescence methods. The fluorescence intensity is proportional to the photosensitive agent concentration and can be detected by a dedicated device. Most of the cancerous cells are submitted to the photosensitizer accumulation unlike the normal cells. Thus, by the measure of the fluorescence intensity, the tumour focuses and their borders can be defined, which lies on the base of the Photodynamic Diagnostics.

The conditions required for the fluorescence diagnostics of tumours are [24]:

- enough quantity of the photosensitizer;
- suitable wavelength of the excitation light (for each photosensitizer, depending on the absorption peaks);
- sufficient laser light power;
- optical system for contrast imaging of the fluorescence (like an optical filter).

Because of the light losses during the relaxation, the fluorescent signal from a tissue with therapeutic doses of the photosensitizer can be hardly detected by a video receiver without a special filter. The filter should be oriented for “cutting” or attenuation of the excitation wave, and for leaving visible the fluorescent range.

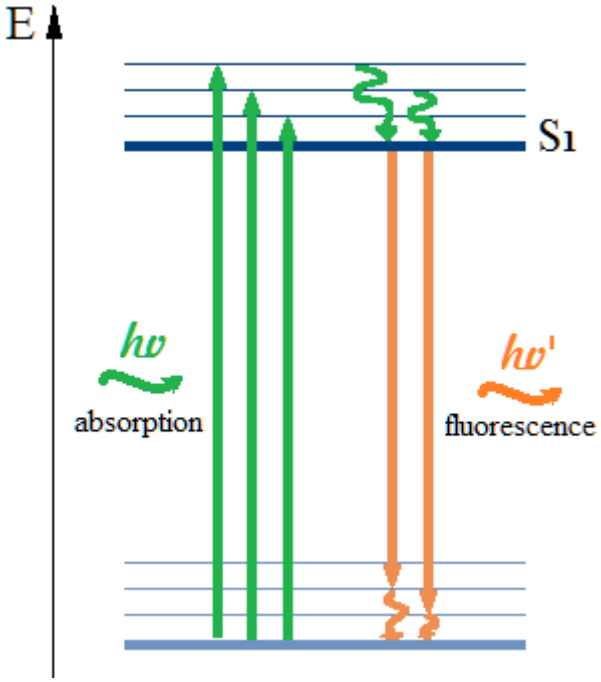

Figure 1.1 *Schematic illustration of the fluorescence excitation.*

1.3 Urinary Bladder Carcinogenesis

1.3.1 Structure of the Urinary Bladder Wall

Urinary bladder (UB) is an organ located in the pelvis. It serves for delivery and collection of the urine. After being formed in the kidneys, the urine comes into the bladder by the ureter and then leaves the body through the urethra. Bladder cancer is the most common cancer of the urinary tract (renal pelvis, ureter, bladder, and urethra), and transitional cell carcinoma represent more than 90% of malignant cancer of the bladder [25]. Due to its multi-layered structure, the UB wall is a turbid inhomogeneous medium. According to structural properties, it can be divided into three main layers: 1) mucous (transitional epithelium), 2) submucous, and 3) muscle [26].

1.3.1.1 Mucous

The surface layer of the UB wall of is the mucous membrane without blood or lymphatic vessels. It contains transitional epithelium tissue consisting of closely situated and relatively large cells (10-20 μm in diameter). In contrast to other stratified epithelia, the urothelium consists of five to seven cell layers of the large rounded epithelial cells (Fig. 1.2), and its thickness is about 200 μm. The property characterizing the bladder wall is the ability to stretch. This is an important capacity as the bladder contains variable volumes of liquid, and is filled and emptied several times per day. When the bladder wall is unstretched, the mucous cells are of a fairly round shape. When the tissue is stretched, the cells, especially those on the surface, become flat, which allows the bladder to change its shape without damaging the epithelial lining. The urothelium lies on a basal lamina, separating it from the underlying connective tissue - lamina propria. The basal lamina is formed by a layer of 50-80 nm thick, and serves as a selective barrier for the epithelial layer and provides a structural support.

Due to the similar features of the tissue characteristics, the neoplasm structure and stages of formation of some other mammalian organs reveal similar behaviour to those of the bladder tissue. For example, the oral cavity, UB and esophagus have all a mucosa as surface layer. Also, tissues with epithelial origin of neoplasm formation show similar properties of tumour structure. Such similarities make it possible to relate some results of studies on other internal organs to the ones for the UB tissue. However, all the differences in the tissue and tumour structures, and their significance and influence on the obtained results should be taken into account.

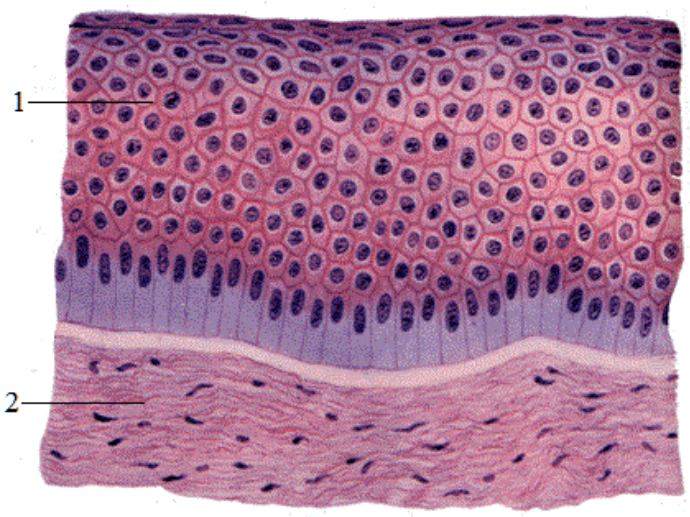

Figure 1.2 *1- mucous, and 2- submucous layers of the bladder wall (adapted from [http://nedomedic.ru/stroenie-perexodnogo-epiteliya.html]).*

1.3.1.2 Submucous

The submucous, also called submucosa or lamina propria, is a thin layer of about 700 μm of areolar tissue that is closely attached to the first layer (mucous), and connects it with the third layer (muscular). The submucosa of the urothelium mostly consists of an intercellular substance (main component), fibrillar connective tissue: collagen and elastin fibers, and small cellular matrix components. The intercellular substance is a gel-like consistence which is due to its composition. Its main ingredient is a highly hydrated gel, that is formed by high-molecular compounds forming up to 30% of the intercellular substance, whereas the remaining 70% of the gel is water. Generally speaking, water forms about 60% of connective tissue [27]. Elastin is a protein in connective tissue that is elastic and allows the bladder wall to take back its initial shape after stretching. Elastin is also an important base of the tissue for storing the mechanical energy. Collagen is the main component of connective tissue, and is the most abundant protein in mammals. Collagen fibers are bundles of elongated fibrils, typical for fibrous protein tissues. In general, collagen fibrils are combined in different ways and appear with different concentrations to provide tissues with various properties. Owing to its properties and structure, gelatine or agar-based phantoms are useful for simulating properties of the tissue [28], [29]. Gelatin itself (and collagen fibers at all) has a high

refractive index [30], [31]. However, gelatin, used for the liquid phantoms (being usually mixed with distilled water (or surrounded by other tissue components)), has a considerably decreased refractive index (see Section 3.6.4.2) [32].

Beneath the urothelium, there is a dense capillary plexus which, besides the vascular supply, serves as a barrier against the urine, penetrated through the epithelial layer. In a contrast to the urothelium, the submucous of the urinary bladder is not reach in the large cells. A tumour, which has spread to the submucous layer, can metastasize to the remaining part of the body via the lymphatics and blood vessels.

1.3.1.3 Muscular layer

The muscular layer of the bladder is formed by the detrusor smooth muscle fibers, arranged circularly and longitudinally. The capability to produce a shortening and thickening of the muscle during bladder contraction is provided by the myofibrils, moving across the smooth muscle. The full thickness of the muscular layer is about 3-5 mm.

The extracellular matrix of the muscular layer, lying between the muscle cells, contains an elastic connective tissue stroma of collagen and elastin. In the muscle tissue the collagen serves as a major component of the endomysium. The availability of the required amount of protein of connective tissue, smooth muscle cells and extracellular matrix is essential for the formation of elastic properties of the bladder wall.

1.3.2 Neoplasm Formation

It is well known that malignant neoplasmes of the UB mainly arise in the urothelial layer of a bladder wall [9]. Usually, pathological stages of epithelial tissues, such as dysplasia or carcinoma *in situ*, precede bladder cancer. Furthermore, at a microscopic visual aspect, dysplastic neoplasms do not differ much from the surrounding healthy tissue, which

complicates the clinical diagnosis [33]. At dysplasia, the main initial endogeneous changes of the tissue are: variations of the cell and nucleus shapes and sizes (increase of nuclear diameter), hyperchromicity [20] and growth of the blood concentration [18]. Besides, non-malignant dysplastic cells show often chaotic reproduction, leading to the increase in population density [34]. All these changes (see Fig. 1.3) contribute to the light distribution inside the tissue.

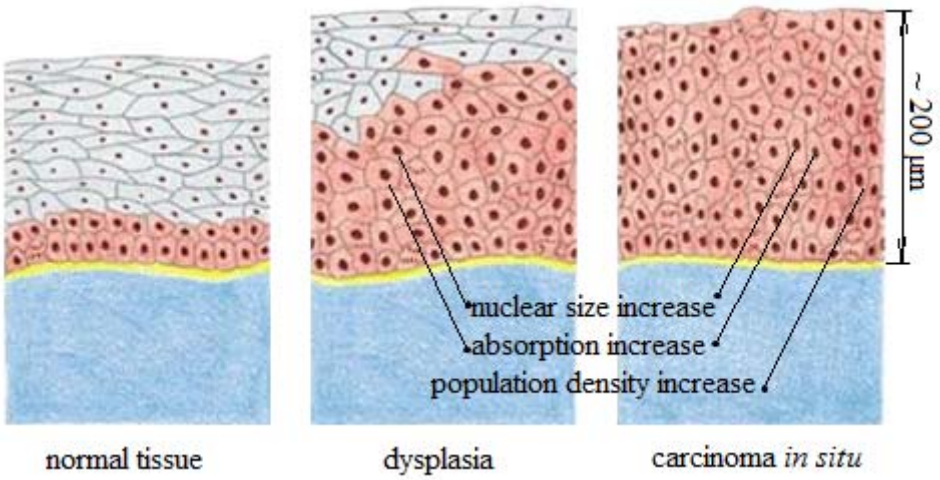

*(*Adapted from [35])

Figure 1.3 *Pathological epithelial changes under dysplasia.*

The changes are reflected in the absorption, elastic and inelastic scattering, fluorescence spectra of the tissue, and can be detected by a video camera on the tissue surface. Moreover, the presence of the photosensitizers in the pathological tissues influences on the diffuse-reflected spectroscopic signal of the fluorescent light. Such data allows to estimate the tissue alterations, by following the accumulations of the photosensible drug in the tissue. White light (WL) cystoscopy is the standard clinical examination for *in vivo* bladder cancer detection. During cystoscopy, targeted and random biopsies are performed for histopathologic analysis of tissue samples leading to final diagnosis. But this procedure has a poor sensitivity especially in the detection of invisible early precancerous tissue stages (limited number of "blind" biopsies) [1], [2], [20]. In many cases when an urothelial neoplastic lesion has been detected, because of its multi-focal nature [36], there is still a probability of unnoticed malignant focuses existence, up to 10% [2], [37], and of recurrence appearance, up to 70%

[38]. Recent works have demonstrated the additional value of fluorescence cystoscopy in improving the contrast between healthy and tumoral tissues *in vivo* [39], [40]. By guiding more efficiently the biopsies, fluorescent cystoscopy, combined to the WL modality, provides diagnostic sensitivity increase (90% instead of 60% with the WL alone). However, these methods still suffer from low specificity [41] due to high rates of false-positive results [2]. Complementary to the aforementioned fluorescence approach, the multiple diffusion of the light can be used to characterize tissue structure related to healthy and pathological stages [20].

1.4 Optical Diagnostic Methods

In this Section of the thesis, we give a brief overview of some optical methods for both, clinical practice and medical research.

Modern optical imaging and visualization of the bladder are based on endoscopic techniques, since the internal surface of the organ has to be studied [42]. The ability to localize effectively the area of interest depends on the sensitivity and specificity of the applied method. Optical diagnostic techniques can potentially greatly improve sensitivity and specificity of endoscopic imaging and therefore increase its diagnostic efficiency.

Biomedical optics are promising fast-evolutive and widely used medical modalities, involving developpments in the interdisciplinary fields. They can be applied at different forms and combinations, showing the corresponding advantages necessary for different healthcare diagnostics. For example, the diagnosis of internal organs requires a possibility to penetrate into the tissue and to visualize it, or to obtain any other diagnostically relevant information.

Covering a wide range of optical techniques and methods, biomedical optics can be based on all the optical phenomemon such as light absorption and scattering, polarisation, luminescence, coherence, reflectance and polarization with the respect to tissue light interaction, and thus to be applied for different tissues. Therefore the biomedical optical techniques, using the laser light, including Photodynamic Therapy [43.], [41], Spectroscopy Analysis [44], and Optical Imaging [45], [46], are commonly used for detection of UB neoplasms.

The information revealed by an optical method reflects the structural and biochemical composition of the tissue, providing a detailed morphological and biochemical analysis of the tissue. Besides, the technological progress makes it possible to combine multiple diagnostic techniques, thereby to improve the diagnostic potential by investigating different aspects of the target tissue, such as macro- and micro-structural tissue peculiarities or molecular composition. In general, the biomedical optical techniques aim to provide a high diagnostic accuracy combined with the information on the structural and functional tissue state.

1.4.1 Photodynamic Diagnosis

One of the new and fast-developing techniques for neoplasm diagnosis at the early-stages, is an imaging method, known as Photodynamic Diagnosis (PDD) [47], [48]. Based on the fluorescence phenomenon, PDD is aimed to detect mainly superficial and thin tumours, by using a combination of a photosensitizing drug and light. Such combination causes a selective change in the wavelength inside the tumorous target. To be efficient, the PDD technique requires the simultaneous presence of a photosensitizer and light. Due to certain properties of correlation of a photosensitive compound with the tissue structures (depending on the type and composition of a photosensitive drug), the photosensitizer is selectively accumulated in the malignant tissues. Once absorbed the energy of the illuminating light, the photosensitizer's molecules are excited to their higher energy level.

PDD is usually performed together with the Photodynamic Therapy (PDT), based on the same mechanism with addition of the oxygen, however requiring a higher light power density. For this therapy, the chemical reaction occurs when the irradiation starts: the photosensitizer molecule releases the excess of energy and after the interaction with the triplet oxygen molecules, produces singlet oxygen (Fig. 1.4). Thereafter toxicity, induced by this process, causes the destruction of biological macromolecules which leads to the cell death.

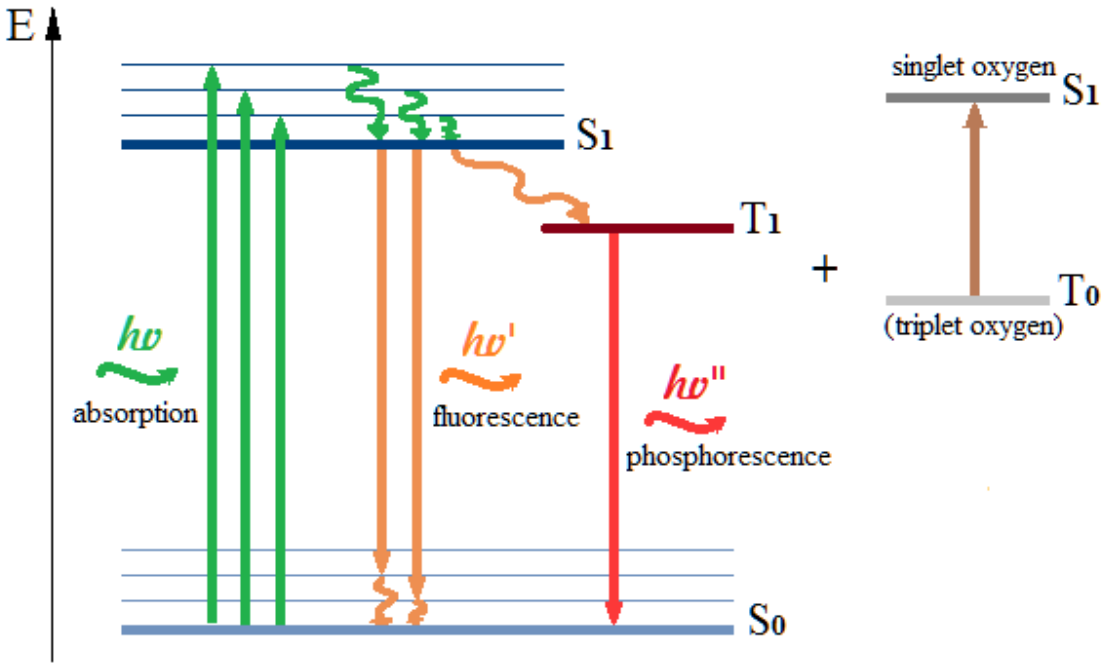

Figure 1.4 *Schematic representation of singlet oxygen formation under the light excitation.*

For an effective therapy, the tissue must contain enough amount of a photosensitizer and molecular oxygen. Moreover, the light photons also must provide the reaction, without overheating the surrounding healthy tissue. Several "generations" of photosensitizing drugs already exist. One of the most popular group of photosensitizers is based on porphyrins [49], [50], [51] allowing for the radiation at the larger wavelength, enabling a deeper treatment. An example of such PDD and PDT agent is aminolevulinic acid (ALA) [24], [52]. ALA induces the formation of the protoporphyrin IX (PpIX) in the cells, which is sensitive to the light at certain wavelengths.

The main advantages of PDD are non-invasiveness and high sensitivity. Zaak et al. reported that fluorescence cystoscopic diagnostic rate of bladder carcinoma was 56.8%, which is higher than that of white light cystoscopy [53]. Moreover, the fluorescence cystoscopy can detect carcinoma in situ with a very high rate of more than 90% [54]. Fluorescence cystoscopy examination has also a high sensitivity in detecting urothelial tumours (86-98%) [55], [56]. However, false-positive results mainly attributed to chronic inflammation of the bladder, simple urothelium hyperplasia and squamous metaplasia [57], can occur during the PDD, which reduces the specificity [58]. Moreover, such diagnostic techniques do not provide histopathologic information [5].

1.4.2 Optical Coherent Tomography

Optical Coherent Tomography (OCT) is another non-invasive diagnostic imaging modality utilizing the light scattering in tissue is. OCT is based on the coherence interferometry [59], occurring over a distance of micrometers. OCT enables for two- and three-dimensional imaging in biological tissues by detecting near infrared light distribution in the tissue, and measuring the reflected or backscattered intensity of light as a function of depth. The OCT technique provides a spatial resolution close to the cellular level. The structural tissue abnormalities influence on the scattering in the bladder wall, revealing the deviation from the normal images. Thus, at the neoplastic state, the mucosal layer can be thicker than at the normal state, and hardly distinguished from the other layers, sometimes shows complete loss of a regular structure [60]. The newest OCT technology allows for making in vivo diagnoses using optical fibers and cystoscopic biopsy channel. However, OCT cannot provide the screening of the entire bladder due to the difficulties in the navigation. For this reason it still has to be used in combination with other methods [5].

1.4.3 Laser Doppler Perfusion Imaging

Laser Doppler Imaging (LDI) is a non-invasive diagnostic method for optical measurement of tissue perfusion. LDI is based on the scattering contrast of moving and motionless tissue components, induced by a coherent light source. Due to the static state of the tissue surrounding the shifting blood cells, the light scattering caused by this tissue does not contribute to the Doppler shifted signal [61], [62]. The signals measured by the method are often related to flux, velocity and concentration of the moving blood cells [63]. The scanning laser Doppler perfusion imaging method acquires both single and multiple scattering from moving blood cells. The speckle phenomenon appears in the Doppler imaging in changes of the tissue optical properties in time and space, leading to the changes in the detected signal.

The major advantage of the laser Doppler techniques in general is its simple implementation in instruments, requiring only an optical probe, a source of coherent light, and

a camera or a receiving fiber. This method is non-invasive and allows to measure the perfusion in real time. However, the velocity distribution of red blood cells cannot be received in absolute blood flow values, since this depends on non-considered by LDI properties of photon interaction with red blood cells. Also the technique suffers from the noise from the outside motions.

1.4.4 Diffuse-Reflectance Imaging and Spectroscopy

Optical spectroscopy is a diagnostic technique allowing the detection in vivo biochemical and morphological changes that occur in tissue during neoplasm progression. Modern applications in optical biophotonics rely on the use of elastic scattering parameters to characterize the underlying architectural properties of biological tissue [64]. Cellular changes in sub-surface tissue layers, caused by dysplastic progression in epithelial tissues, affect the absorption, scattering and fluorescence properties of tissue. They also lead to diagnostically significant differences in the measured back-scattered spectral signals. The absorption properties of the tissue provide information on the concentration of various chromospheres, while the scattering properties are rather important for interpretation of the form, size, and the concentration of the scattering components in tissue. Since spectral measurements do not require tissue removal, the diagnostic information can be obtained non-invasively and in real-time, providing an objective and quantitative description of the tissue**.**

The spectroscopic techniques are easily applicable for the endoscopic diagnosis, as they are quite simple in their instrumentation: the spectral measurements are provided by an optical probe, and analysed by a spectrometer. A laser light beam illuminates the tissue, and the back-scattered light is collected by optical fiber.

Diffuse-reflectance imaging can be used in addition to spectroscopy or as a self-dependent technique for neoplasm diagnosis. In the case of implementation of the diffuse reflectance at an imaging mode, diffuse backscattered light is detected by means of a video camera. The technique can detect both, diffuse-reflected scattered and fluorescent light. Some of the optical properties can be obtained in vivo using this imaging and spectroscopic techniques [6], which allow to describe the tissue state.

Autofluorescence studies of the biological tissues are mostly based on the analysis of the endogenous fluorescing molecules [65]. Almost all biological tissues emit fluorescence when excited at appropriate wavelength in the UV or visible spectral range. A biological tissue consists of a complex matrix of fluorescing and non-fluorescing molecules. The major fluorescing tissue proteins are collagen and elastin, both present in the structural matrix of numerous tissues [65]. Due to the low autofluorescence intensity, the autofluorescence systems do not exhibit a sufficient contrast.

1.5 Conclusion and Problem Formation

Even though the disadvantages of the existing optical techniques for the bladder diagnosis are different, they can be still generalized. The main lack of all the techniques is that they are specified for a certain metamorphosis, not allowing the other tissue changes to be taken into account. Thereafter, detection of several tissue "markers" simultaneously can improve the diagnosis, by providing information on complex data of tissue state.

The DR light analysis can be used for different purposes by means of varying the type of the measurements and optical constructions. Non-polarized DR imaging or spectroscopy can be easily coupled to a WL endoscopic imaging in order to provide additional information for a precancerous and non-invasive tissue diagnosis. The principle of the non-polarized DR imaging associated to cystoscopy is to illuminate some areas on the tissue surface by means of the optical fibers, and to measure the spatial distribution of the back-scattered non-polarized light. The backscattered light, arising from illuminated tissues, is influenced by the changes in nuclear size, epithelium thickness and other tissue components, which can serve as "markers" for the neoplasm detection. Thereafter, the method of detection of non-polarized DR light has big potential to provide useful diagnostic information to specify the tissue changes of early neoplasms *in vivo* and non-invasively.

As modern techniques require a complex approach for soling diagnostic problems, then not only instrumentation has to be determined. Mathematical modelling is also a useful tool for modern diagnostic techniques. For multi-layered tissue-light interaction simulations, a Monte Carlo-based method can be used. Such mathematical description of tissue optical

properties can provide diagnostically useful information [66]. Forward and inverse problems are commonly used for the Monte Carlo problematic solutions [67]. The complete process of solving problems of tissue-state description by the diffuse reflected light analysis can be divided into the following parts:

- Theoretical (mathematical) modelling of the DR from the surface of the medium (forward problem);
- Experimental studies of the surface DR distribution;
- Calibration (comparison of the theoretical and experimental studies);
- Solving inverse problem.

In the forward problems, for which some input parameters are known, the process of the diffuse reflectance can be mathematically described with the use of the optical parameters of the medium. In the inverse problems, on the contrary, the unknown necessary parameters can be obtained from the DR light signals. This thesis describes forward experimental and mathematical (Monte Carlo based) methods of visualization of the DR light on a surface of 3-layered models of the UB wall (Fig. 1.5).

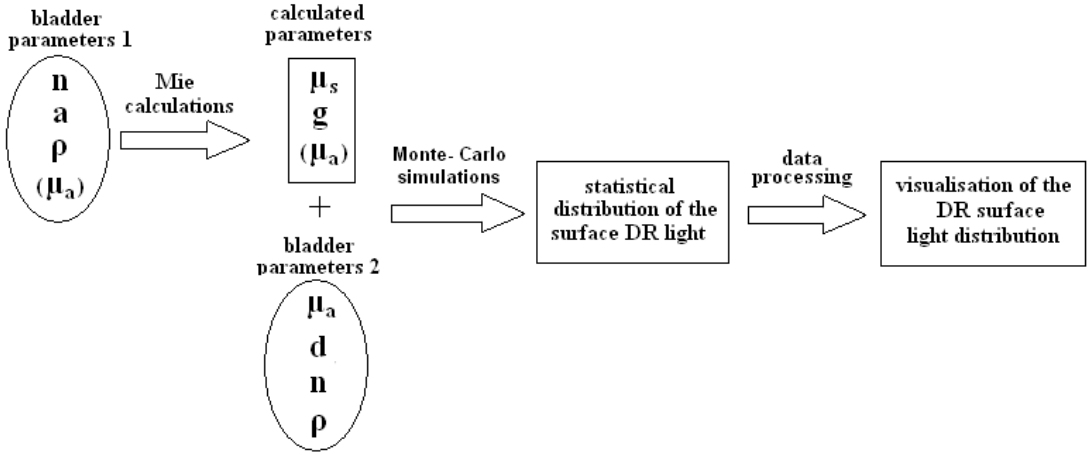

Figure 1.5 *Forward problem solution method: n - refractive index, a -size of a scatterer, ρ - population density of scatterers, μ_a - absorption coefficient, μ_s -scattering coefficient, g- anisotropy factor, d - thickness of a medium/layer.*

Thus, we expect our method of DR light detection to allow to analyse scattering and absorption tissue properties, and thereafter to make it possible to differentiate *in vivo* different tissue states at the early cancerous and pre-cancerous stages.

References:

[1] Babjuk M., Transurethral resection of non-muscle-invasive bladder cancer, Eur. Urol. Supplements 8, 542-548, 2009.

[2] Nese N., R. Gupta, M. Bui, M. Amin., Carcinoma in situ of the urinary bladder: review of clinicopathologic characteristics with an emphasis on aspects related to molecular diagnostic techniques and prognosis, Journal. of the Natl. Compr. Canc. Netw. 7 (1), pp. 48-57, 2009.

[3] Poh C. F., S. Ng, K. W. Berean, P. M. Williams, M. P. Rosin, L. Zhang, Biopsy and Histopathologic Diagnosis of Oral Premalignant and Malignant Lesions, J. Can. Dent. As-soc. 74(3), 283-288, 2008.

[4] Keshtkar A., R. Smallwood, Virtual bladder biopsy by electrical impedance measurements (62.5 Hz-1.5 MHz), IFMBE Proceedings, Volume 14, Part 27, 3911-3914, 2007.

[5] Cauberg E., D. de Bruin., D. Faber, T. van Leeuwen, J. de la Rosette, T.de Reijke, A New Generation of Optical Diagnostics for Bladder Cancer: Technology, Diagnostic Accuracy, and Future Applications, European Urology 56, 2009.

[6] Beck T. J., W. Beyer, T. Pongratz, W. Stummer, R. Waidelich, H. Stepp, S. Wagner, and R. Baumgartner, Clinical Determination of Tissue Optical Properties in vivo by Spatially Resolved Reflectance Measurements, Proceedings of SPIE-OSA Biomedical Optics, SPIE Vol. 5138, 2003.

[7] Jost S. P., J. A. Gosling and J. S. Dixon, The morphology of normal human bladder urothelium, J. Anat., 167, pp. 103-115, 1989.

[8] Perelman L. and V. Backman, in: V. Tuchin (ed.), Optical Biomedical Diagnostics 2, Fizmalit, Moscow, 2007, pp. 36-76, 2007.

[9] Backman V., M. Wallace, L. Perelman, J. Arendt, R. Gurjar, M. Müller, Q. Zhang, G. Zonios, E. Kline, J. McGilligan, S. Shapshay, T. Valdez, K. Badizadegan, J. Crawford, M. Fitzmaurice, S. Kabani, H. Levin, M. Seiler, R. Dasari, I. Itzkan, J. Van Dam, M. Feld, Detection of preinvasive cancer cells, Nature 406, 2000.

[10] Vo-Dinh T. (ed.), Biomedical Photonics Handbook, CRC Press, LLC, 2003.

[11] Niemz M. H., Laser-Tissue Interactions Fundamentals and Applications, 3d edition, Springer-Verlag Berlin Heidelberg, 2007.

[12] Mandelstam L. I., "Light Scattering by Inhomogeneous Media". Zh. Russ. Fiz-Khim. Ova. 58, 1926.

[13] Bohren C., D. Huffman: Absorpttion and scattering of light by small particles, Wiley & Sons, New-York, 1998.

[14] Alvarez R. D., T. C. Wright and O. D. Grp, “Effective cervical neoplasia detectrion with a novel optical detection system: A randomized trial”, Gynecologic Oncology 104 (2), 281-289, 2007.

[15] Prahl S., Molar extinction coefficients of oxy and deoxyhemoglobin, http://omlc.ogi.edu/spectra/hemoglobin/summary.html, 1998.

[16] Hale G. M., and M. R. Querry, Optical constants of water in the 200 nm to 200 µm wavelength region, Appl. Opt., 12, 555-563, 1973.

[17] Dunn K. J., Williams, B. O., Li, Y., Pavan, W. J.. Neural crest-directed gene transfer demonstrates Wnt1 role in melanocyte expansion and differentiation during mouse development, PNAS 97 (18): 10050-10055, 2000.

[18] Koenig F., R Larne, H. Enquist, F. J. McGovern, K. T. Schomacker, N. Kollias, and T. F. Deutsch, Spectroscopic measurement of diffuse reflectance for enhanced detection of bladder carcinoma, Urology 51 (2), 342-345, 1998.

[19] Van Staveren H. J., J. F Beek, J. W. H. Ramaekers, M. Keijzer and W. M Star, Integrating sphere effect in whole bladder wall photodynamic therapy: I. 532 nm versus 630 nm optical irradiation, Phys. Med. Biol. 39, pp. 947-959, 1994.

[20] Gurjar R. , V. Backman, L. Perelman, I. Georgakoudi, K. Badizadegan, I. Itzkan, R. Dasari, M. Feld, Imaging human epithelial properties with polarized light- scattering spectroscopy, Nature Medicine 7(11), 1245-1248, 2001.

[21] Mourant J. R., Irving J. Bigio, James Boyer, Tamara M. Johnson, JoAnne Lacey, Anthony G. Bohorfoush, and Mark Mellow, Elastic scattering spectroscopy as a diagnostic tool for differentiating pathologies in the gastrointestinal tract: preliminary testing, Journal of Biomedical Optics 1(2), 192–199, 1996.

[22] Lovat L, Bown S, Elastic scattering spectroscopy for detection of dysplasia in Barrett's esophagus, Gastrointest Endosc Clin N Am.;14(3):507-17, 2004.

[23] Lakowicz J. R., Principles of Fluorescence Spectroscopy, Kluwer Academics/Plenum Publishers, New York, 1999.

[24] Loschenov V. B., V. I. Konov, A. M. Prokhorov, Photodynamic therapy and Fluorescence diagnostics, Laser Physics vol. 10 No 6, pp. 1188-1207, 2000.

[25] Tanaka MF, Sonpavde G., Diagnosis and management of urothelial carcinoma of the bladder, Postgrad Med.;123(3):43-55, 2011.

[26] Feneis H., W. Danberg, Pocket atlas of human anatomy based on the international nomenclature, 4th edition, Thieme, 2000.

[27] Werner A. P. Luck, Water in biological systems, in Topics in Current Chemistry, Werner A. P. Luck, Vol. 64, pp. 114-180, 1976.

[28] Pogue B. W., Michael S. Patterson, Review of tissue simulating phantoms for optical spectroscopy, imaging and dosimetry, Journal of Biomedical Optics 11(4), pp. 041102-1 – 041102-16, 2006.

[29] Cubeddu R., Antonio Pifferi, Paola Taroni, Alessandro Torricelli and Gianluca Valentini, A solid tissue phantom for photon migration studies, Physics in Med. Biol., 42, 1971.

[30] Seeboth A., H. Hermel, "Gelatin films with embedded liquid crystals in the conoscopic ray," Thin solidfilms, 173, pp. L119-L129, 1989.

[31] Genina E., A. Bashkatov, K. Larin and V. Tuchin, Light tissue interaction at optical clearing, at “Laser Imaging and Manipulation in Cell Biology” by Francesco S. Pavone (ed.), John Wiley & Sons, Germany, 2010.

[32] BashkatovA. N. , Elina A. Genina, Vyacheslav I. Kochubey, Valery V. Tuchin, Effects of scattering particles concentration on light propagation through turbid media, Proceedings of SPIE Vol. 3917, 2000.

[33] Tuchin V., Optical Biomedical Diagnostics 2 Fizmalit, Moscow, 2007.

[34] Backman V.: Imaging human epithelial properties with polarized light scattering spectroscopy PhD Thesis, 2001.

[35] Alberts B., D. Bray, J. Lewis, M. Raff, K. Roberts, and J. D Watson,' Molecular Biology of the Cell, 3rd edition, New York: Garland Science, 1994.

[36] Kakizoi T., Development and progression of urothelial carcinoma, Cancer Sci. 97, 9, 2006.

[37] Tetu B., Diagnosis of urothelial carcinoma from urine, Modern Pathology 22, 2009.

[38] Ihnat M., K. Kyker, J. Thorpe, S. Shenoy, R. Hurst, The Phenotypically Suppressed Cancer Cell As a Therapeutic Target American Journal of Pharmacology and Toxicology 1, 4, 2006.

[39] Filbeck T., U. Pichlmeier, R. Knuechel,W. Wieland, W. Roessler, Do patients profit from 5-aminolevulinic acid-induced fluorescence diagnosis in transurethral resection of bladder carcinoma?, Urology 60, 6, 2002.

[40] Barocas D., P. Clark, Bladder cancer, Curr. Opin. Oncol. 20, 3, 2008.

[41] Stenzl A. and S. Kruck, Should photodynamic diagnosis be standard practice for bladder cancer?, Expert Rev. Anticancer Ther. 9(6) 697-699, 2009.

[42] Morgan TM, Clark PE., "Bladder cancer", Curr Opin Oncol. 22(3):242-9, 2010.

[43] Kausch I., M. Sommerauer, F. Montorsi, A. Stenzl, D. Jacqmin, P. Jichlinski, D. Jocham, A. Ziegler, R. Vonthein, Photodynamic diagnosis in non-muscle-invasive bladder cancer: a systematic review and cumulative analysis of prospective studies, Eur Urol. 57(4), 595-606, 2010.

[44] Bensalah K., J. Fleureau, D. Rolland, N. Rioux-Leclercq, L. Senhadji, O. Lavastre, F. Guillé, J. J. Patard, R. de Crevoisier, Prog Urol. 20(7), 477-482, 2010.

[45] Danil'chenko D. I., A. S. Al'-Shukri, V. N. Tkachuk, Optical coherence tomography in diagnosis of urinary bladder cancer, Urologiya (in Russian) 2, 42-44, 2009.

[46] Bryan R. T., L. J. Billingham, D. Michael and A. Wallace, Narrow-band imaging flexible cystoscopy in the detection of recurrent urothelial cancer of the bladder, BJU International 101(6), 702–706, 2008.

[47] Cortes S., JA, Grahan J, Soloway MS., Photodynamic diagnosis in urology: state of the art, Arch Esp Urol.; 64(1):18-31, 2011.

[48] Mowatt G, N'Dow J, Vale L, Nabi G, Boachie C, Cook JA, Fraser C, Griffiths TR, Photodynamic diagnosis of bladder cancer compared with white light cystoscopy: Systematic review and meta-analysis, International Journal of Technology Assessment in Health Care, 27(1):3-10, 2011.

[49] Dougherty T. J., B.W. Henderson, S. Schwartz, J.W. Winkelman and R.L. Lipson, Historical Perspective, B.W. Henderson, T.J. Dougherty (eds.), Photodynamic Therapy, Marcel Dekker, New York, 1992.

[50] Ethirajan M, Chen Y, Joshi P, Pandey RK., The role of porphyrin chemistry in tumor imaging and photodynamic therapy, Chem Soc Rev.;40(1):340-62, 2011.

[51] Allison R. R., Claudio H. Sibata, Oncologic photodynamic therapy photosensitizers: A clinical review, Photodiagnosis and Photodynamic Therapy, Vol. 7(2), pp. 61-75, 2010.

[52] Krammer B, Plaetzer K., ALA and its clinical impact, from bench to bedside, Photochem Photobiol Sci. Mar;7(3):283-9, 2008.

[53] Zaak D, Karl A, Knuchel R, et al. Diagnosis of urothelial carcinoma of the bladder using fluorescence endoscopy, BJU Int; 96:217-22, 2005.

[54] Isfoss B. L., The sensitivity of fluorescent-light cystoscopy for the detection of carcinoma in situ (CIS) of the bladder: a meta-analysis with comments on gold standard, BJU Int. Dec;108(11):1703-7, 2011.

[55] Steinbach P., Kriegmair M., Baumgartner R, F Hofstädter, R Knüchel, Intravesical instillation of 5-aminolevulinic acid (5-ALA): The fluorescent metabolite is limited to urothelial cells. Urol;44:676-81, 1994.

[56] Filbeck T, Roessler W, Knuechel R, Straub M, Kiel HJ, Wieland WF., 5-Aminolevulinic acid-induced fluorescence endoscopy applied at secondary transurethral resection after conventional resection of primary superficial bladder tumors. Urology; 53(1):77-81, 1999.

[57] Hartmann A, Moser K, Kriegmair M, Alfons Hofstetter, Ferdinand Hofstaedter, and Ruth Knuechel, Frequent genetic alterations in simple urothelial hyperplasias of the bladder in patients with papillary urothelial carcinoma. American Journal of Pathol; 154 (3):721-7, 1999.

[58] Jocham D, Stepp H, Waidelich R. Photodynamic diagnosis in urology: state-of-the-art. Eur Urol;53:1138–50, 2008.

[59] Riederer, S.J. "Current technical development of magnetic resonance imaging". IEEE Engineering in Medicine and Biology Magazine 19 (5): 34–41, 2000.

[60] Zagaynova EV, Streltsova OS, Gladkova ND, Snopova LB, Gelikonov GV, Feldchtein FI, Morozov AN, .In vivo optical coherence tomography feasibility for bladder disease,.J Urol.;167(3):1492-6, 2002.

[61] Drain L., The Laser Doppler Technique, John WileyPress, USA, 1980.

[62] Leahy M. J., F. F. M. de Mul, G. E. Nilsson, and R. Maniewski R, “Principles and practice of the laser-Doppler perfusion technique,” Technology and Health Care 7, 143–162 1999.

[63] Rajan V., B. Varghese, T. G. van Leeuwen and W. Steenbergen, Review of methodological developments in laser Doppler flowmetry, Lasers in Medical Science Vol. 24(2), 269-283, 2009.

[64] Mourant J. R., I.J. Bigio, J. Boyer, R.L. Conn , T. Johnson and T. Shimada, Spectroscopic diagnosis of bladder cancer with elastic light scattering, Lasers Surg. Med. 17, 350-357, 1995.

[65] Pery E., W. C. P. M. Blondel, S. Tindel, M. Ghribi, A. Leroux and F. Guillemin, Spectral Features Selection and Classification for Bimodal Optical Spectroscopy Applied to Bladder Cancer in vivo Diagnosis, IEEE Trans Biomed Eng., 2011.

[66] Wang, L., Jacques, S., and Zheng, L., "MCML- Monte Carlo modeling og light transport in multi-layered tissues", Comp. Meth. in Biomed. 47, 131-146, 1995.

[67] Palmer C. M., and Ramanujam, N., "Monte Carlo-based inverse model for calculating tissue optical properties. Part 1: Theory and validation on synthetic phantoms", Appl. Opt. 45(5) 1062-1071, 2006.

2

CHAPTER

Experimental Investigation of Diffuse-Reflected Light

"Omnia mutantur, nihil interit."

Ovidius

2.1 Introduction

This chapter describes the proposed method for *in vivo* detection of diffuse-reflected light signals for diagnostic uses for the urinary bladder. In many of existing measurement methods, both transmitted and back-scattered light, are analysed. However such measurements are not sufficient for *in vivo* analysis of the internal organs, as the transmitted light cannot be detected. The idea of the analysis of the back-scattered light from media with different sizes, concentration and absorption properties of the scatterers, arisen after our analysis of the tissue structure and the mechanism of neoplasm formation. The experience shows that the simplicity of the instrument is a major factor for actually obtaining a method easily usable in clinical situation. The basic idea of the proposed method with relatively easy instrumentation is to detect the differences in distribution of the diffusely reflected light on the surface of different media according to their scattering or/and absorption properties.

The intensity profile of diffuse reflected light, acquired from a surface of a media, containing scatterers with different optical properties, under the homogenous irradiation by a narrow laser beam, is expected to be characterized in the following way: the amount of the photons outcoming from the central part of the illuminated area of the medium, is greater than the one from the surrounding area (Fig. 2.1). Even though the scattered photons inside the tissue gradually move away from the beam center, on average, they still follow its direction, forming a halo around the beam. The size of the halo and the proportion of energy largely depend on the diameter of the laser beam and the optical properties of the tissue: the smaller the diameter of the beam, the greater density of the photons will be in the halo. Thus, the effectiveness of the irradiation will be higher.

As illustrated in Fig.2.1 a and b, zone *II*, *p(x)* along the adjoining to the center of distribution area (i.e. a decreasing amount of diffusively back-reflected photons) decreases due to the multiple scattering and absorption inside the tissue, whereas the photons are mainly directly back-reflected in the central part of the illuminated spot, because of a specular reflection of the incident light. By comparing the intensity profiles, shown in Fig. 1a and 1b,

for small and large diameters of diffusing particles in the medium, one can see that the central zones (*I*) are equivalent, unlike the lateral zones (*II*) which differ with the scatterer diameters.

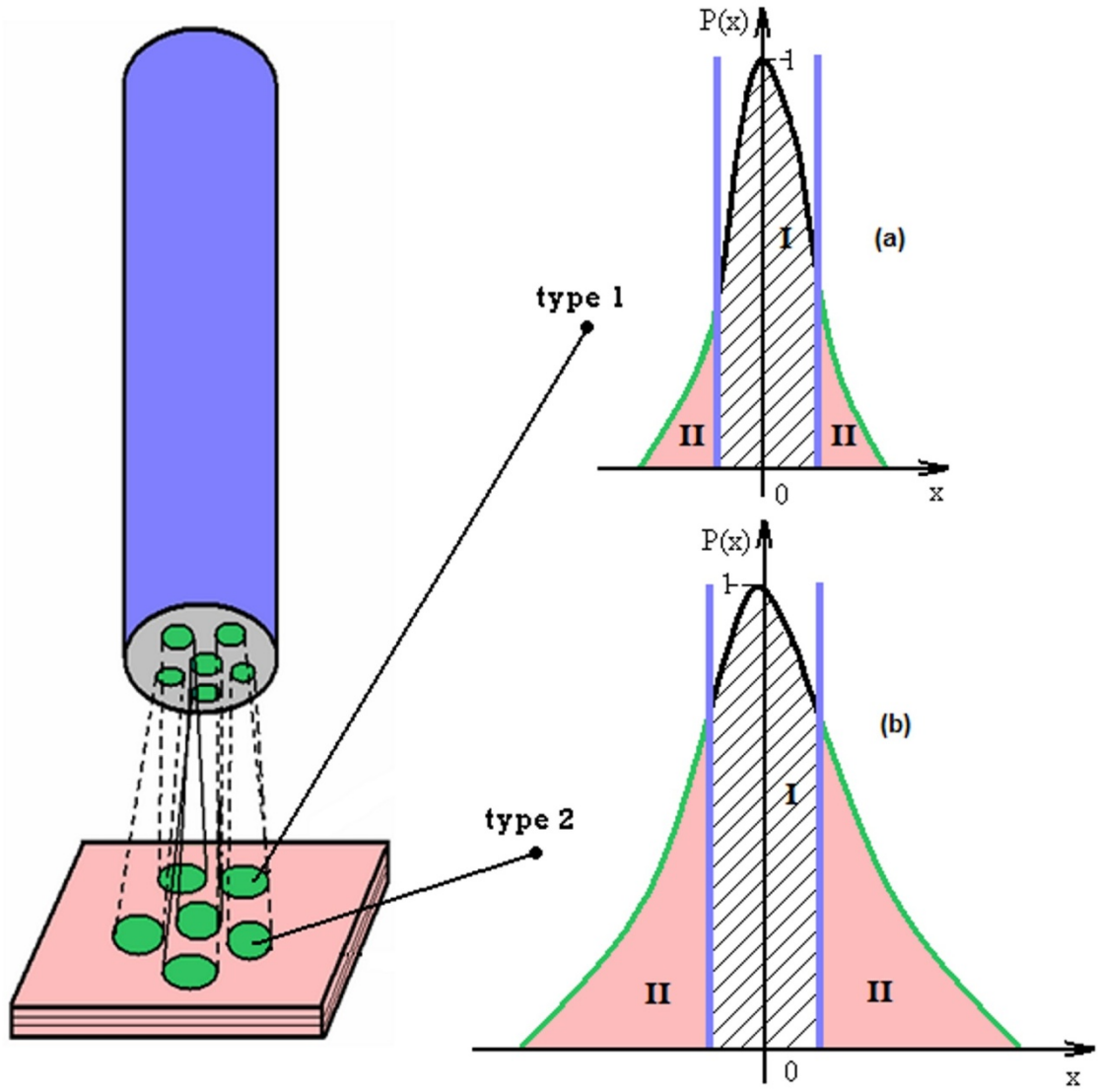

Figure 2.1 *Intensity profiles of the surface light distribution.*

The most common technique for extracting the optical properties of tissue is the Integrating Sphere method [1], [2]. The major drawback of this technique is that it cannot be applied *in vivo*. Such limitation does not allow us to apply this method in the present study.

An optical technique based on the illumination of the tissue surface by a narrow laser beam can be used as a non-invasive method for early diagnosis of superficial human bladder cancer. The dependence of the penetration depth into a tissue on the laser beam diameter

plays an important role in the accuracy and interpretation of the measurements, made at the surface of the tissue. As it is shown in Fig. 2.2, the wider the beam, the deeper light penetration. For our purposes it is more useful to perform the study with the narrow beam, as the initial neoplasms arise mostly on the surface layer of the bladder wall (which is of about 200 μm thick), and the high fluence rate is not necessary for such investigations. Thus, the light, penetrated for several hundred micrometers into a tissue, provide more accurate measurements on the superficial bladder layer, which allow to reduce the noise of the back-scattered signal.

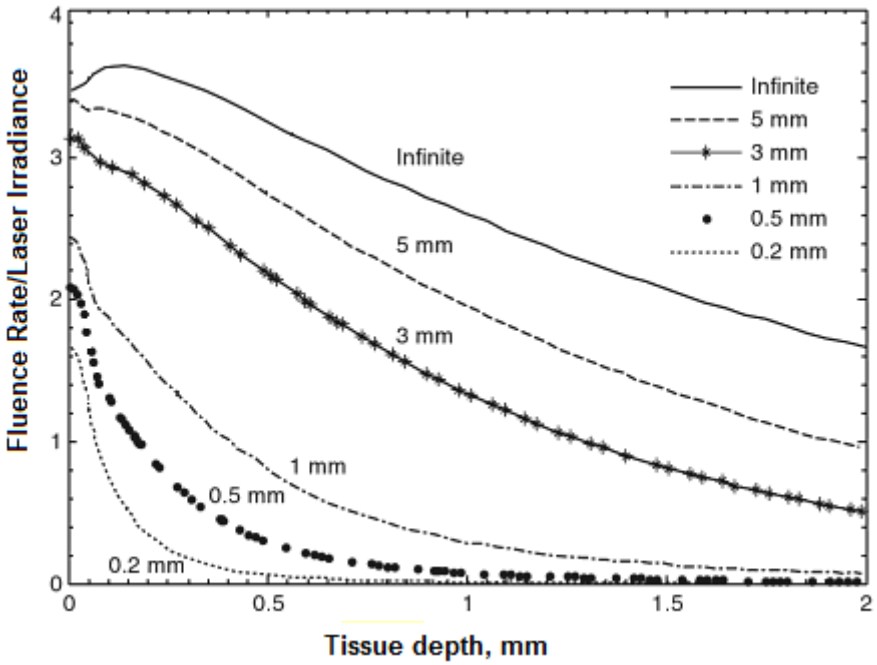

Figure 2.2 *Dependence of the irradiating beam diameter on the penetration depth (adapted from [3]). The data obtained from the Monte Carlo simulations made for the skin tissue at 585 nm for the irradiance (1 W/cm^2).*

2.2 Sensitivity Tests of the Diffuse-Reflectance Imaging Method

In this Section we present an experimental investigation of the sensitivity of the DR imaging to detection of the spatial intensity responses. The measurements were performed on different types of multi-layered phantoms containing diffusing particles and simulating different bladder states. The image-processing methods for different purposes of DR light analysis are also proposed in this Chapter.

2.2.1 Experimental Construction

Tissue illumination with the use of optical fiber probes is quite common for the studies in biomedical optics. Different systems (like imaging or spectroscopic) can detect different types of light signals from the tissues. The detecting methods can also be combined together for enhancing the analysis potential. For example, some systems for surface light distribution detection have been already applied with addition of white-light spectroscopic measurements for determining optical penetration depths of non-collimated laser light to bladder and brain tissues by Beck *et al.* [4]. In this Section of the thesis we present a set-up for imaging back-scattered laser light distribution on the surface of a media for detection of micro-changes in scattering and absorption properties of different media. The set-up was constructed following real clinical conditions.

Among the most important specific features of laser light are coherence (the light waves coming from a laser are all in phase), and high light concentration in the laser beam. Such light can be focused to an optical fiber, widely used in biomedical optical analysis. Because of relatively low penetration depth [1], a diode laser of a 532 nm wavelength at a 15 mW power was used as a light source in our experimental set-up (see Fig. 2.3).To provide the laser radiation of the media, an optical fiber of 600 μm diameter was connected to a diode laser, and was attached to a rigid endoscope base, Stryker, 30°, 10mm. For beam focusing on the media surface, the optical fiber was coupled to a micro collimator - a lens in objective. The final diameter of the laser spot, illuminating the surfaces of the media, was 300±15 μm. The

diameter was measured with a micrometer, fixed at a distance of 37 mm from the lens end. A colour video camera (Watec WAT-221S), with signal-to-noise ratio of about 50dB, was connected to an endoscope by means of an optical adapter. The camera served for acquiring and transferring of the images to a personal computer. The experiments were carried out in the dark without any additional light sources except the laser irradiation source. For the chosen light conditions, an automatic mode of the shutter speed (from 1/50 Sec. to 1/100000 Sec.) of the camera was the most suitable for acquiring well contrasted images.

Because of the size of the objective of the lens, the optical fiber was located at a distance of 1.5 cm along the endoscopic base, which limited the possibilities to observe necessary areas. However, the 30˚ orientation of the front-view endoscope enabled the imaging of the DR light on the irradiated phantom surface.

The endoscope and the fiber were placed at a normal to the phantom surface. The distance from the optical fiber to the micro-collimator was 13 mm, from the micro collimator to the phantom - 37 mm, from the micro collimator to the endoscope tip- 15/20 mm, and from the endoscope tip to the phantom - 8/13 mm (see Fig. 2.3).

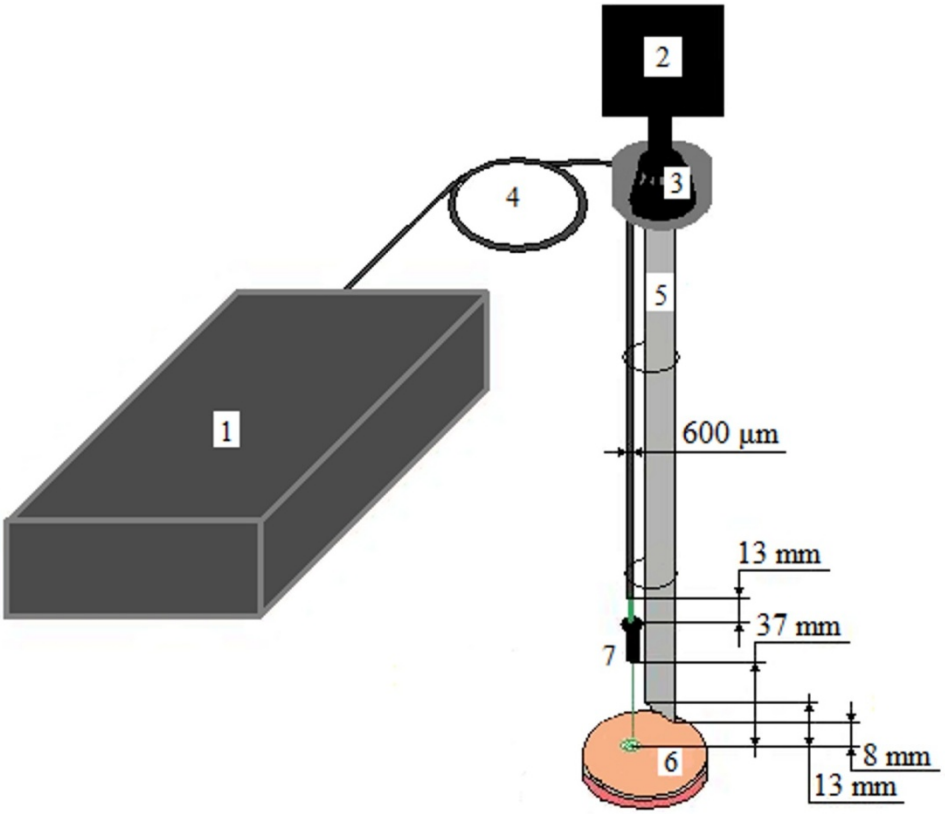

Figure 2.3 *Experimental set-up: 1 - diode laser (532 nm, 15 mW), 2 - highly sensitive colour camera, 3 - adapter for camera and endoscope connection, 4 - optical fiber, 5 - endoscope with a front-side view (30°), 6 - phantom, 7 - lens in the objective for light focusing.*

2.2.2 Three-Layered Phantoms Construction

In order to perform testing studies of the light propagation into a medium, one can use biological models, called also tissue phantoms. Different phantoms simulating the optical behaviour of urinary bladder wall can be useful to understand the mechanism of internal light scattering. They can also be helpful for identifying the main principles of differences of DR light signals from healthy and pathological tissues. For biomedical studies, such phantoms should correlate with scattering and absorption optical properties of the tissue of interest over the necessary spectral range [5], [6]. The possibility of selective variation of the phantom composition (thus of their optical-geometric parameters) allows controlling the impact of various phantom properties to the distribution of the back-scattered light [7], [8].

According to the purpose of the experimental studies, tissue phantoms can be realized, using various substances, including Intralipid, agar or gelatin powder, distilled water, ink, haemoglobin or polystyrene microspheres [9], [10], [11], [12], [13]; [14], The fluid phantoms, for example allow small solid targets to be placed within them, and to perform the movements, mimicking, for example, the blood flow. Intralipid is commonly used in order to reproduce the scattering behaviour of different tissues. Some of the optical properties of Intralipid are already studied [15], [16], which simplifies construction and analysis of the phantoms. For precise control of the anisotropy factor and size and concentration of the scatteres, polystyrene spheres can be used in phantoms. Gel-based dense phantoms allow to separate tissue layers or regions with different tissue properties [17], [18]. The most popular absorbers for tissue phantoms are inks, food colouring agents or industrial dyes.

For our studies multi-layered synthetic phantoms of three types were constructed by superposing three layers. The layers, simulating different parts of the urinary bladder wall, had different thicknesses and optical properties. The first layers varied in sizes of diffusing particles, while the two other layers were identical for all three types of the phantoms (Fig. 2.4).

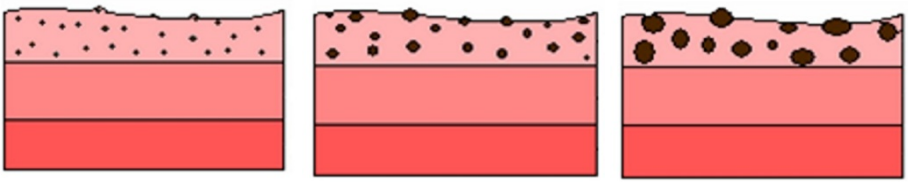

Figure 2.4 *Composition of the phantoms simulating three layers of the bladder wall: mucosal (with scattering particles of different diameter), submucosal and muscle.*

The first (top) layer simulated diffusing optical properties of cell nuclei of transitional epithelium of the urinary bladder mucosa. A substance, consisting of gelatine powder of 5% concentration and micro and nano polystyrene spheres suspended in distilled water, was taken as a basic component of the medium. To estimate the contribution of scatterers with different sizes to the scattering process inside the medium, microspheres of various diameters in a concentration of 10^7 spheres per ml were used as main scatterers of the first phantom layers. The particles of the smallest diameter of 50 nm were included to the phantoms of a 1st type. The microspheres of 0.53 μm diameter characterized the phantoms of a 2nd type, and the

microspheres of 5.09 μm diameter were added to the phantoms of a 3rd type. The thickness of the first layers was 200 μm.

The second and the third layers were made from Intralipid in 1.6% and 2.0% concentrations, respectively, and of gelatine powder of 5% concentration, diluted in distilled water. The thickness of the second layers was 700 μm, and that of the third one was 2100 μm. All layers were put into a Petri dish with a black coloured bottom for ensuring theabsorption of the photons having passed through the phantom.

2.2.3 Image Processing

This section describes the methods of image processing for comparison of the images acquired from the surfaces of different phantoms. The methods applied in our study can be divided into two parts: visualization methods and methods for quantitative analysis. Both types of the image processing can be useful in diagnostic studies, depending on the aims and possibilities of analysis.

2.2.3.1 Image Subtraction

The size of RGB images acquired by the video camera was 320×240 pixels. However, useful for the analyses image areas of the diffuse-reflected light corresponded to 60×50 pixels (Fig. 2.5). Such small areas could not be large enough for obtaining differentiative information on DR signals from different phantom types. For that reason a bilinear interpolation, which is widely used in a medical imaging [19], [20], [21], between the neighbouring points of the images, was applied. The idea of the bilinear interpolation is to expand an image by linear fitting of two neighbouring points with the coordinates (x_1, y_1) and (x_2, y_2) along two orthogonal directions. The fitting of a straight line by two points is given by:

$$y = y_1 + (x - x_1)\frac{y_2 - y_1}{x_2 - x_1} \quad (1)$$

with $x \in (x_1, x_2)$.

The final interpolated area was 520×432 pixels. Prior to the data analysis, each RGB image was first converted into a grayscale image:

$$Gray = 0.3R + 0.59G + 0.11B \quad (2)$$

The graylevel values were then normalized between 0 and 255.

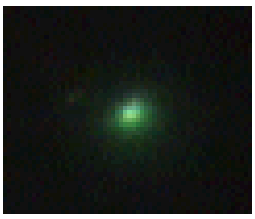

Figure 2.5 *Area of 60×50 pixels corresponding to the Diffuse-Reflected light signal (a rough image acquired by the camera).*

In order to estimate the impact of the particle's size on the light distribution, a visualisation analysis of the normalised images was performed by means of subtracting all images one from another (Fig. 2.6). For the contrast enhancement, prior to their subtracting, each image was multiplied by a constant value of 3, determined after comparing the images with the results of multiplication by other constants. In the matrices obtained after image subtraction, the central areas were formed by almost zero intensity signals (black round areas in the image centres of Figs. 2.6 *a* and *b*), which is due to similar Fresnel reflection in all the phantoms, and a high concentration of the DR light around the place of entrance of the incident beam. Such a "noise" does not allow to differentiate the signals from each other in the central parts.

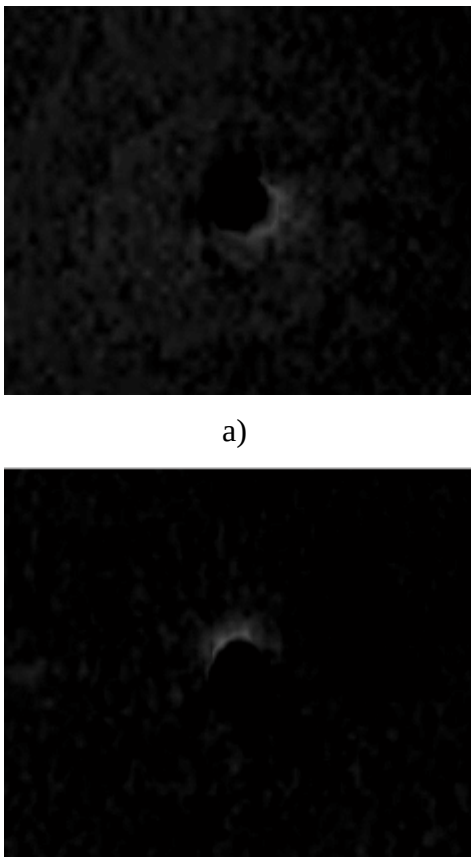

a)

b)

Figure 2.6 *Images of the Diffuse-Reflected light for different particles: (a) one image for the particles of 50 nm diameter minus another one of the same kind, (b) one image for the particles of 5.09 μm diameter minus an image taken for the particles of 50 nm diameter.*

However, because of small image centre displacement due to mismatches in the central areas under the image superposition, there was a nonzero signal around the central region in the subtracted images, which can be clearly seen in the Fig. 2.6 b. Almost a zero signal was observed at some distance from the central areas of the DR of the matrices obtained with the subtraction of the data acquired for the media with scattering particles of the same diameter, i.e. 50 nm – 50 nm, 0.53 μm – 0.53 μm, or 5.09 μm – 5.09 μm, (Fig. 2.6 a). On the contrary, after subtraction of the DR images, taken for the phantoms with different diameters, there were nonzero signals on some distance from the centre (Fig. 2.6 b). Due to the size of the scatterers, the DR signal from the media with the small particles of 50 nm diameter, can be considered as a background signal, as the impact of such small particles on the light scattering is minimal. Such image processing allows for distinguishing the signals from the phantoms with different properties of diffusing particles, however, the processed images still suffer from large noise intensity.

2.2.3.2 Three-Dimensional Diagrams

This subsection describes another visualisation method of processing the images from the surfaces of the phantoms. For analysing the DR surface distributions, the three-dimensional intensity diagrams were plotted in MATLAB environment. Prior to their processing, the truecolor RGB images were converted to the grayscale intensity images. For more distinguishable visualization and for noise attenuation, the images were treated with a basic morphological operator of mathematical morphology, namely dilation. The dilation operation was performed by superposing each pixel of a grayscale image with a symmetrical disk-shaped structural element, comparing the elements of the structural element with corresponding underlying pixels of the image. This allowed replacing dark central pixel value by a brighter gray-level value, according to the pixels values of the neighbourhood defined by the structural element. As every grayscale image can be presented as a function *f(x)*, giving the relationship between the coordinates and the grayvalues of the pixels [22], the modifications of the images by a function *g(x)*, defining a structural element can be described by:

$$(f \oplus g)(x) = \sup_{z \in G, (x-z) \in F} \{f(x-z) + g(z)\} \quad (3)$$

where *f*: *F*→*E*, *g*: *G*→*E*, and *F* and *G* are subsets of the *(N-1)*-dimensional Euclidean space [22].

Thereby, the parametric surfaces were created for three types of the phantoms (Fig. 2.7 a-c). The hue, saturation and intensity space (HSI) was chosen for the representation of the surface with “false” colours. On the diagrams, the pixel coordinates were plotted horizontally and vertically, on the *x* and *y* axes, respectively. The intensity values were plotted on the *z* axis, and are presented by false colours. The intensity of the DR light increased with the diameter of the scatterers, which is related to the contribution of each diameter of the particles to the scattering process. In the center of the diagrams, signals are similar for all the phantoms with the particles of different dimensions in terms of intensity distribution. However, for the areas surrounding the diagram center, differences of the DR signals are visibly distinguishable.

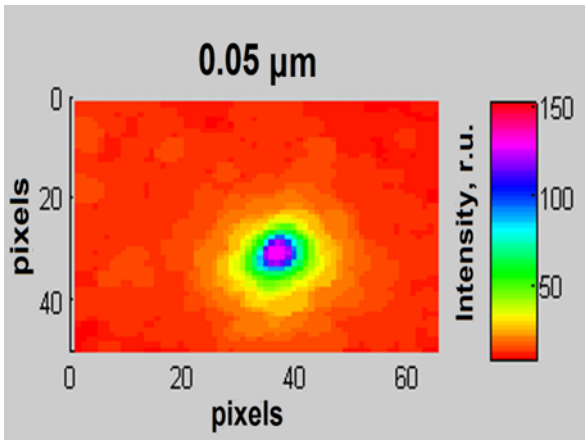

a)

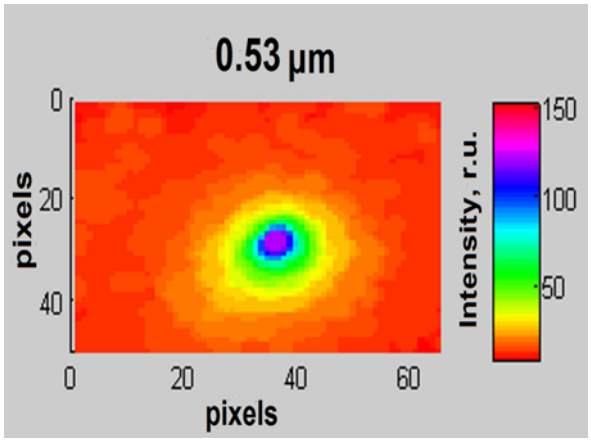

b)

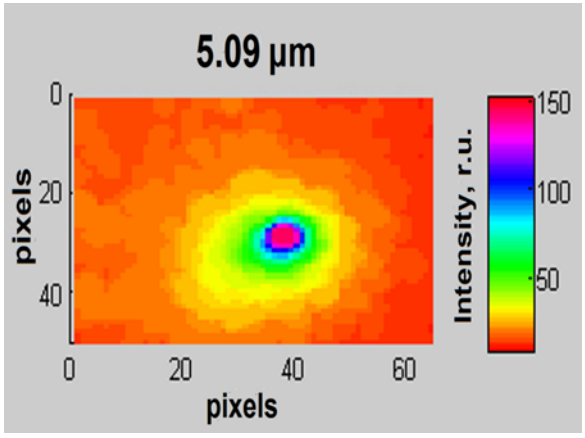

c)

Figure 2.7 *3-D intensity diagrams of the Diffuse-Reflected light measured for the particles of different diameter: (a) 50 nm, (b) 0.53 µm, (c) 5.09 µm.*

2.2.3.3 Area Measuring

However, obtaining only visual information is not satisfying enough for an objective result assessment. To quantify the light spot differences, the correlation between the sphere diameters and the area of DR light in the image were calculated.

To perform such calculus, the interpolated (see Section 2.2.3.1) truecolour RGB images (with pixel values from 0 to 255 in each colour band) were first converted to the grayscale ones (with pixel intensity values belonging to[0, 1]), and then binarized. Each image was divided into foreground and background pixels, creating two data sets:

$G_1 = \{f(m,n): f(m,n) > t\}$ (foreground pixels with value 1)

$G_2 = \{f(m,n): f(m,n) \leq t\}$ (background pixels with value 0) (4)

where *f(m,n)* is the value of pixel located in the m^{th} column, n^{th} row [23], and *t* is a threshold value, which was experimentally chosen (see below).

If symmetrically chosen values x_1 and x_2 in the zones *II* on the *x* axis of the Fig. 2.1, then the two extreme points of the back-scattering areas can be defined, so that the value $d = |x_2 - x_1|$ corresponds to the diameter of the areas. The threshold value of 0.11 for the grayscale images lies near the border of the DR light on the surfaces of the phantoms. Based on this observation, this value was chosen to measure the DR areas. Therefore all pixels with luminance, greater than 0.11, were replaced with 1 (the white colour in Fig. 2.8), and the values of all other pixels were replaced with 0 (the black colour in Fig. 2.8).

Such operation has allowed us to get the numerical results by measuring the areas corresponding to the halo diameters. For the higher calculation accuracy, we have filled up all the white holes which were remaining in the black image areas after the conversion to the binary format. Then, to obtain the area values, the amount of pixels of the “white” areas was calculated for each binary image.

We have processed 45 DR light images representing irradiated phantom surfaces. Since 15 images were treated for each phantom type, the probability of each “event” (“event” corresponds to the data from each image of one of the phantom types) was 1/15. For statistical analysis, we have calculated the variances of the expected values, and, by square-rooting, the standard deviations for the areas with light intensity higher than 0.11 (Table 2). The variance of the expected value of the DR light areas is equal to the mean of the square minus the square of the mean: $E(X) = \sum_{i=1}^{15} (x_i * p(x_i))$ with x_i is the area value, *X* the mean value of the

area, $E(X)$ the expected value, and $p(x_i)$ the probability of an area value. The variance of the expected value is [24]:

$var(X) = E[X^2] - (E[X])^2$

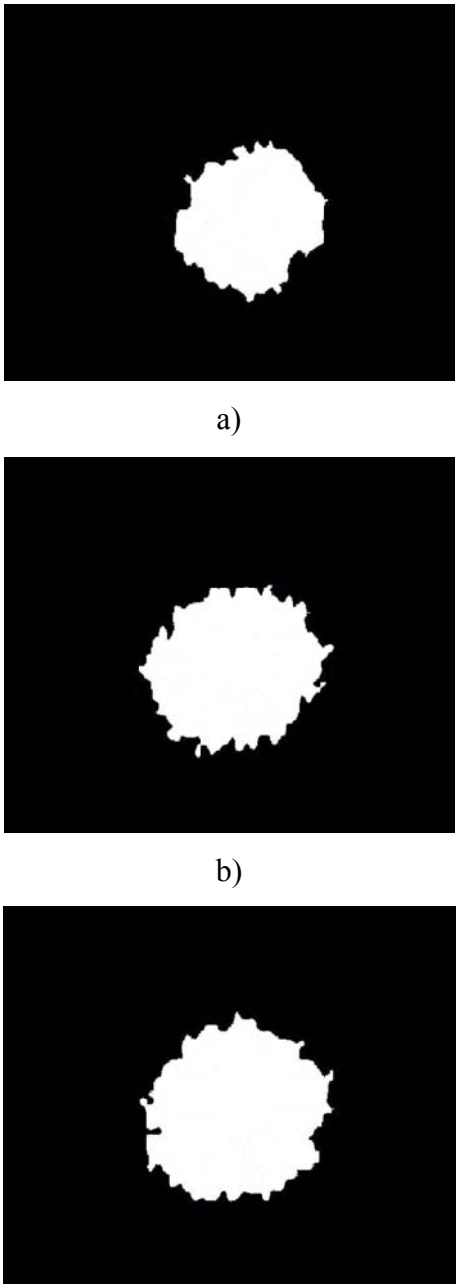

a) b) c)

Figure 2.8 *Examples of binary images used for the calculation of the Diffuse-Reflected areas with threshold of 0.11 for the phantoms with scattering particles of different diameter: (a) 50 nm, (b) 0.53 µm, (c) 5.09 µm.*

The results provided in Fig. 2.9 show that at an average, the surface areas of the optical responses to the changes in the laser signals on the surface of different types of the phantoms. However, a non-parametric statistical Mann–Whitney–Wilcoxon test was performed to assess, whether the data obtained from two phantom types (with 0.53 and 5.09 μm scatterers diameters) belongs to two distinctive groups:

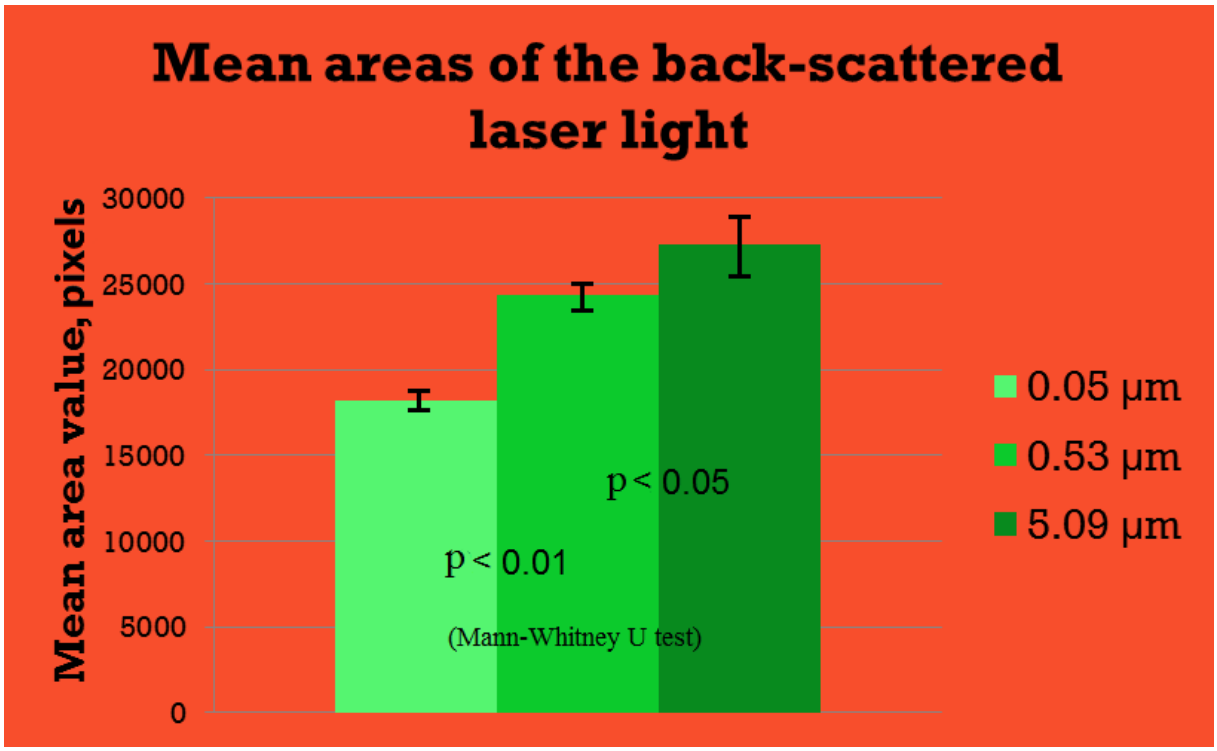

Figure 2.9 *Mean areas of back-scattered laser signals.*

The H_0-hypothesis for our study: the data 1 (area of the back-scattered light from the phantoms with the microspheres of 0.53 μm diameter) is equal to the data 2 (area of the back-scattered light from the samples with the microspheres of 5.09 μm diameter); The H_1-hypothesis (alternative): data 2 > data 1. The U-criteria of Mann–Whitney is

$$U = n_1 * n_2 + \frac{n_x*(n_x+1)}{2} - T_x \qquad (5)$$

where n_1 and n_2 are the number of units in the first and second group respectively, T_x is the greatest value of the two rank sums, corresponding to the n_x-group.

In our study: $n_1 = n_2 = 15$, thus

$$U = n^2 + \frac{n*(n+1)}{2} - T_x = 68 \qquad (6)$$

From the Critical Value Table for the Mann-Whitney U-test we found a critical value corresponding to the 15×15 units, which is for a standard significance level of α=0.05 [25]

(confidence 95%) equal to 64. Such result shows that the data 2 > data 1, thus the H_1 alternative hypothesis is true. Consequently, it is possible to conclude that there are significant differences in the back-scattering areas arising on the surfaces of the phantoms with two different diameters of the scattering particles.

Diameter of polymer spheres/ Measures parameters	50 nm	0.53 μm	5.09 μm
Mean area (in pixels)	18170.8	24356.9	27266.3
Variance of expected value	2259021	7176856.1	35561233
Standard deviation	1503	2679	5963
Accuracy	92%	89%	78%

Table 1 Parameters calculated for the areas of surface Diffuse-Reflected laser light.

The area measurements let us to obtain the information on the laser spot diameter with a high accuracy (Table 1). However, a higher standard deviation for the microparticles of 2nd and 3rd phantom type can be noticed.

2.2.4 Discussion

This section describes a technique for the detection of the differences in the surface back-scattered light signals from the media with different diameters of the scatterers. The obtained results reveal a variable contribution of polymer particles of different sizes to the light diffusion in biological models of the urinary bladder wall. The proposed image processing methods has provided us with the extraction of the DR parameters, which makes possible the

differentiation between the back-reflected light from the particles of 50 nm, 0.53 μm and 5.09 μm diameters.

The greatest impact to the scattering process is made by the particles of the largest diameter of 5.09 μm. It is noticeable that these diameters are close to the sizes of the cell nucleus, in which main initial cancerous transformations arise. The impact of the other scatterers to the DR signal can be used for the estimation of the background signal that does not change during the cancerous transformations, and may be subtracted, or considered as a zero signal. However the accuracy (78%) of the measured areas of back-scattered light for the phantoms with the scattering particles of 0.53 μm and 5.09 μm diameters, in the concentration of 10^7 spheres per ml, is relatively low. The increase in the concentration of the scatteres (which means more distinguishable differences in the scattering parameters) and augmentation of the quantity of the measurements will lead to higher accuracy and sensitivity. The results, obtained in this Section show that the DR imaging method can potentially be useful for *in vivo* diagnosis of urinary bladder pathology. To improve the diagnostic capacity of our optical system and to avoid measurement errors, several additional fiber-optical laser channels can be added to the existing set-up.

Moreover, for further analysis it is necessary to take into account some other aspects of the neoplasm formation, such as absorption changes and population density changes, which strongly influence the absorption and scattering properties. Such kind of studies can provide useful information on the tissue state and may improve clinical diagnosis.

2.3 Five States of Urinary Bladder Epithelium

2.3.1 Phantom Construction

For experimental estimation of dependence of the surface laser light distribution on the micro-changes of the tissues, five types of three-layer phantoms simulating the bladder wall were prepared (see Fig. 2.10). According to the bladder structure and initial pre-cancerous changes, five phantoms types were chosen to simulate several possible changes in tissue.

The third layers, mimicking the muscular layer of the bladder, were identical for all the phantom types and consisted of 7% of gelatine dissolved in distilled water, 2% of Intralipid

and an absorber (black ink at a concentration of 0.001%). The second layers, simulating tissue submucosa, were also identical for all the five phantom types, and consisted of 7% of gelatine and 1.6% of Intralipid. The phantoms were classified into 5 types was according to the composition of their first layers, simulating the transitional epithelium of the urinary bladder. The basis of all the first layers was made of 7 % of gelatin, of an absorber (black ink) of 0.0005% concentration, and polystyrene microspheres (Bang Laboratories) of 0.05 μm and 0.53 μm diameter in a concentration of 10^{10} particles per ml each.

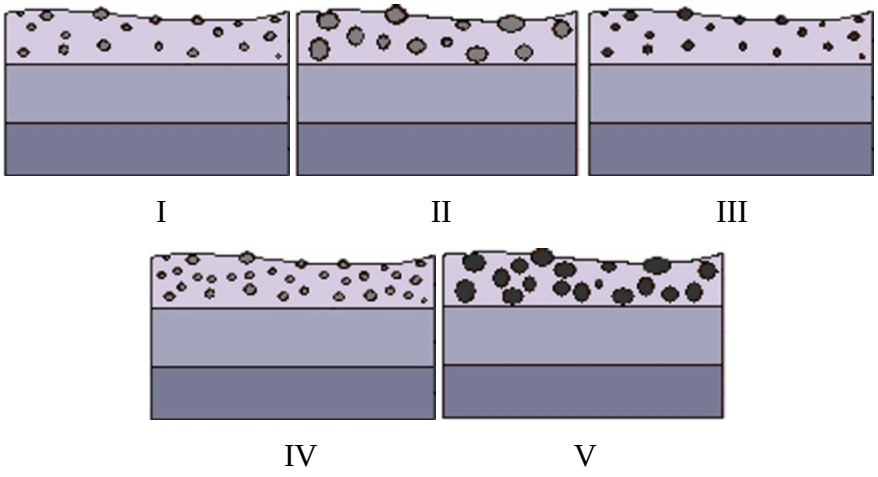

Figure 2.10 *Structure of the phantoms of five types mimicking the bladder wall: I – normal tissue, i.e. with cell nuclei of normal size, II - enlarged nuclei, III - absorption growth, IV - population density augmentation, V - all changes together.*

The first layer of the first phantom type contained polystyrene particles of 5.09 μm diameter at a concentration of $8x10^6$ spheres per ml. In the second types of the phantoms the mean diameter of the scatterers was bigger: to the basis of the first layers the particles of 5.09 and 20.92 μm in a concentration of $4x10^6$ particles (of each size) per ml were added. The third phantom type differed from the first and second types by the presence of additional absorber at a concentration of 0.00075%. Thus, the total concentration of the absorber in the first layers of the third type of the phantom was 0.00125%. The fourth type of phantoms differed from the others by a more dense packing of the scattering particles: the concentration of the microspheres of 5.09 μm diameter was $1.6x10^7$ spheres per ml. The last (fifth) types of the phantoms consisted of the scatterers with increased average sizes and density, higher absorber

concentration: the microspheres of 5.09 and 20.92 μm diameter were added in a concentration $8x10^6$ each, and the total absorber concentration was 0.0025%. The thickness of the third layers was 2.1 mm, that of the second was 0.7 mm, and that of the first was 200 μm. The composition of the phantoms, selected to simulate various properties of the light scattering on the bladder wall, was based on the five main epithelial changes described in the Chapter 1 and recalled in the Fig. 2.10.

The surface of the phantoms was simultaneously illuminated by six laser beams, generated by a copper vapour laser (510.6 nm, Mechatron), an optical probe with 6 fibers of 200 μm, and an optical lens (f = 17mm) for the light collimation. The lens was located at an equal distance of 4.6 mm to the fiber end, and to the surface of the phantoms. The illuminating probe consisted of 6 fibers in order to arise the scanning surface area and to reduce the measurement errors. The scattering signals induced by the six laser beams were acquired from the surfaces of the phantoms by a black-and-white video camera (Videoskan, 30 ms exposure, 200 amplification). The final diameter of each beam was 0.5 mm.

2.3.2 Acquired Images

The illumination of a tissue or media by a probe, consisting of multiple fibers, allows analysing average areas of the back-scattered laser light induced by six fibers simultaneously (Fig. 2.11), or, if necessary, analysing DR signals induced by each of six fibers. For the quantitative analysis, the third method, described in the Section 2.3 was chosen to provide the differentiative information on 15 images acquired for each phantom type. Thus, in order to analyse the differences between the surface signals depending on the composition of the first layers of the phantoms, the pixel areas of the diffuse-reflected light were calculated for all 5 phantom types. The algorithm of the area's calculation, including the main operations, were similar to the ones described in the Section 2.3.3.3, thus they will be briefly described in this section.

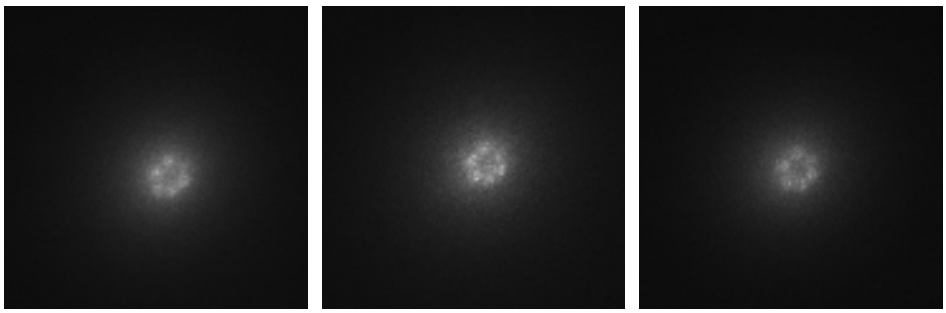

I type II type III type

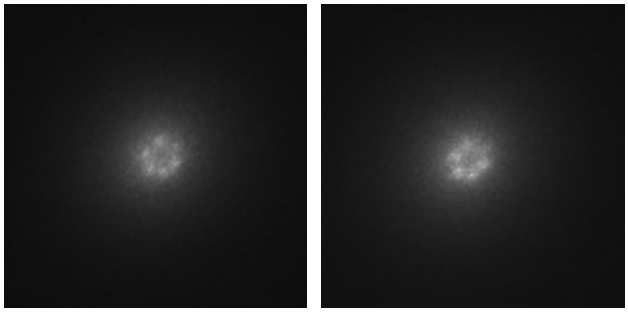

IV type V type

Figure 2.11 *Examples of acquired images of the back-scattered light, induced by a multi-fiber probe. Five phantom types: I – normal tissue, i.e. with cell nuclei of normal size, II - enlarged nuclei, III - absorption growth, IV - population density augmentation, V - all changes together.*

The initial grey images were normalized between 0 and 1, and then converted to the binary images by giving the “0” values to all the intensity values below the threshold value 0.3 (by comparing with other values it was revealed that such threshold allows to differentiate our images more sufficiently), and the values “1” to all the pixels which intensity value was lower the threshold. All the holes in the white areas were filled in by the values “1”. The pixel areas with the values, equal to 1 were calculated for all the 75 images.

2.3.3 Results and Discussion

Fig 2.12 gives the back-scattered area values, calculated for each type of the phantom, are presented. The lowest area values were obtained for the phantoms with higher absorption; the highest - for the nuclear growth (type II) and all the changes together (type V). All the signals significantly differ from each other in terms of area values. This observation is especially noticeable in the case of comparing the results for the changes of absorption (type III) and all the changes together (type V). However, the differences of the signals from the phantoms with the higher the population density of the scatterers (type IV) compared with the "normal" state (type I), can be ambiguously interpreted. The later observation can be explained by the low quantity of the main scatteres in the phantoms. However, such concentrations are high enough for the detection of the other scattering and absorption changes. In the real tissues, the concentrations of the nuclei can vary with the type of the tumour, with its location and with its malignancy.

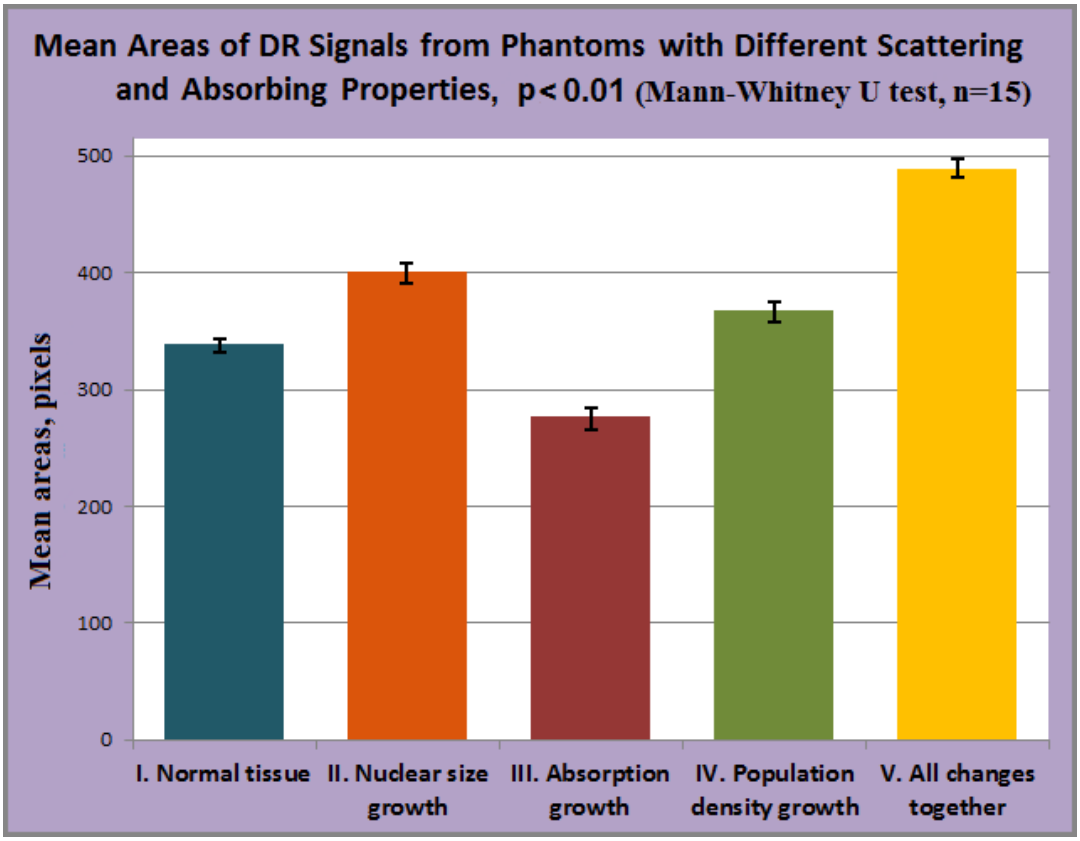

Figure 2.12 *Average areas of the back-scattered laser light on the surface of the phantoms, simultaneously illuminated by 6 fibers.*

2.4 Surface Fluorescence Signal Detection

As it was discussed before, the presented method is aimed to detect the differences in the DR light signals. However, the used construction allows for the fluorescence measurements, which can be necessary, for example, during the PDD. The two methods can give mutually complementary information on the tissue state. In order to estimate the sensitivity of our visualisation method to the changes in the photosensitizer concentration, and to describe the algorithm of such analysis, we present in this chapter the study on the fluorescence measurements.

2.4.1 Preparation of Experimental Studies

2.4.1.1 Clinical Measurements of Photosensitizer Concentrations

The method described below is a modification of the DR light analysis technique, and can be applied either as a separate diagnostic tool, or as a fluorescence diagnosis associates to the photodynamic therapy for biopsy navigating, detection of the tumour borders and specificity tests. Before the phantom constructing and examining the sensitivity of the method to determination of accumulation of the photosensitizer it is necessary to define approximate standard concentrations (and their orders) of the photosensitizer accumulation in normal and pathological tissues. On that purpose, we analysed the results of the spectroscopic studies, held previously in the Russian Blokhin Oncological Research Center in collaboration with the laser spectroscopy laboratory of the Prokhorov General Physics Institute of Russian Academy of Sciences.

The initial motivation of this research study was our previous finding that during fluorescence monitoring of a radical transurethral resection of the bladder, the fluorescence signal of tumours were visually brighter than inflammatory and dysplastic tissues. Thus, we decided to make a quantitative measurement of the fluorescence intensity in order to compare normal and neoplastic tissue signals of the UB wall. Such a study is helpful for understanding the intrinsic fluorescence properties of the tissue and to estimate quantitatively the accumulation of the ALA-induced photosensitizer protoporphyrin-IX (PpIX) at different tissue states.

To control the distance between the optical catheter and the tissue, and to follow the same measurement conditions, the studies were conducted *ex vivo*. During examination of the bladder wall in the fluorescent light modality, the biopsy material was taken from different, fluorescent and non-fluorescent, parts of the bladder mucosa. Due to the fact that the biopsy material cannot be fully cleaned from the blood before the measurements, the spectra can lead to significant measurement errors. Thus, in order to reduce the absorption dependence on haemoglobin concentration it is necessary to choose the wavelength, which does not depend on the haemoglobin absorption. In Fig. 2.13 the absorption spectra of oxy- and deoxygenated haemoglobin are shown.

The data were taken from the table given by Scott Prahl [26], and converted into the absorption units, notably [cm^{-1}]. Usually, for the *ex vivo* studies, it is necessary to take into account the properties of the oxygenated haemoglobin, as the tissue has accumulated the oxygen from the air. However, at some parts of the tumour tissue, there can be deoxygenated haemoglobin. Thus, the spectra of absorption of both haemoglobin states have to be taken into consideration. Considering the absorption spectra of Fig. 2.13, the wavelength of 633 nm (red light) was chosen for the spectral measurements.

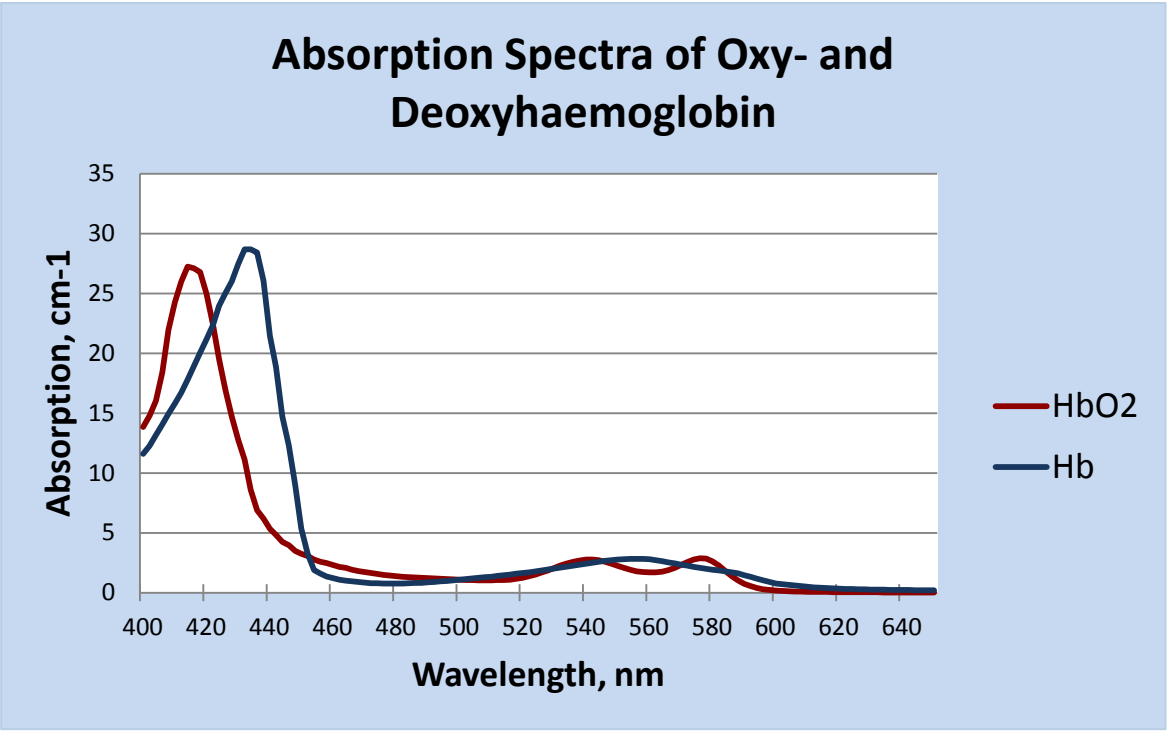

Figure 2.13 *Absorption spectra of haemoglobin in water for (1% of blood concentration). The initial data was taken from [26].*

The experiment was held with the portable multichannel laser spectral analyser of last generation “LESA 01” [27] of co-production BioSpec, Russia and General Physics Institute of Russian Academy of Sciences. The system allows to receive spectra of diffuse reflected laser and fluorescence light with an 0.1 second intervals that are enough for real time monitoring. Also, the device allows for making registration of fluorescence spectra in a rapid mode in a wavelengths range from 400 nm to 850 nm synchronously on more than 3000 channels. The system contains a flexible Y-shaped multichannel fiber-optical catheter (see Fig. 2.14) with 1.8 mm diameter. Due to the small diameter and flexibility the catheter can enter into the biopsy channel of an endoscope with the aim to explore such organs like UB. The device can provide a close observation of the investigated surface, including using a contact mode. A narrow-band optical filter, reducing the intensity of the back-scattered laser light by a factor of 10^4, is located in front of the entrance to the spectrometer. The filter allows to analyse the spectral features of fluorescence and back-scattered laser light at the same scale.

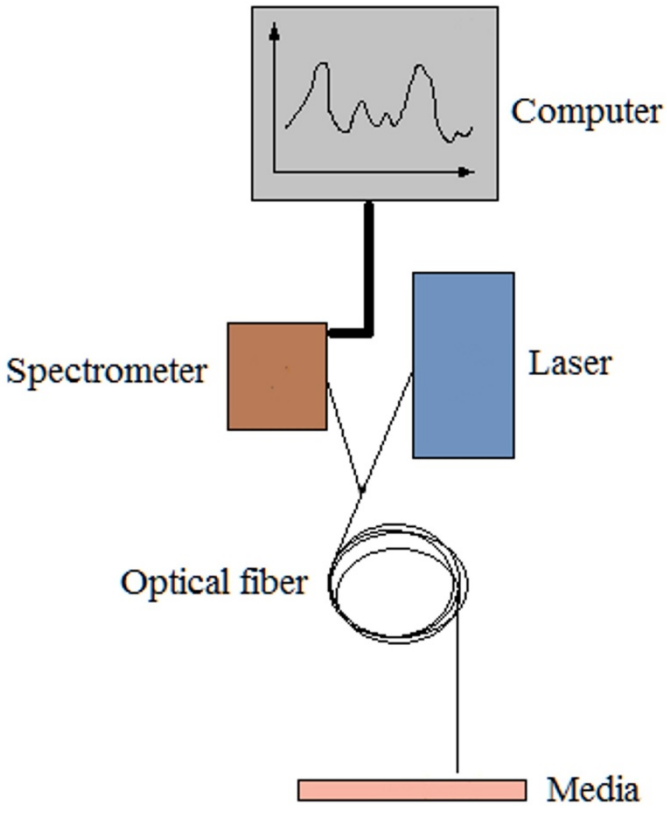

Figure 2.14 *Schematic construction of a portable system for in vivo measuring of both, fluorescence and laser reflection spectra.*

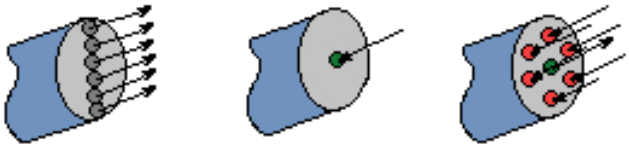

Figure 2.15 *Fiber ends. From left to right: 1) connective end to spectrometer; 2) connective end to laser; 3) illuminating end.*

The measure principle of the system was the following: the light from a laser source was focused on the entrance of the Y-shaped fiber-optical catheter (see Fig. 2.14). For the study described in this Section we have used a helium-neon laser producing light with a wavelength of 632.8 nm, and with the power of 25 mW. The analytical end of the diagnostic catheter was designed in such a way that it could be inserted into the biopsy channel of a conventional endoscope for internal organs.

Fluorescence and laser light passed through 6 receiving fibers surrounding the laser light delivery fiber (see Fig. 2.15). The 6 fibers, arranged in a set at the output of the catheter, were connected to the spectrometer in such a way that the light flux was increased without any resolution loss. For an effective use in biophysical and clinical applications, the device enables to make real-time analyses of the spectral information.

The spectral measurements were performed at an angle of 15°, and at a distance of 1-2 mm between the fiber end and the tissue. Such experimental conditions were necessary to permit penetration of the blinks and to receive signals from near-surface area. The spectral measurements were held in a dark box dedicated for measurements on biopsy material. The measurements were performed just after resection to avoid the photobleaching effect. Marked after spectral measurements, the biopsy tissues were sent for histological studies.

2.4.1.2. Results

After processing the signal, transformed by the spectrometer, we obtained the spectrograms of different parts of bladder walls. The spectrograms were complex curves, consisting of fluorescence spectra in the range of 650-800 nm, and back-scattered laser light in the range of 625-640 nm (Fig. 2.16). The curves had similar shapes with a maximum of intensity at about

700 nm and weak peak at around 665 nm, which is typical for the fluorescence of the PpIX. The wavelengths in nanometers and the fluorescence intensities in relative units (r.u.) were respectively plotted on the horizontal and vertical axes. The shapes of the curves gave us information about the fluorescence properties of the tissue substances.

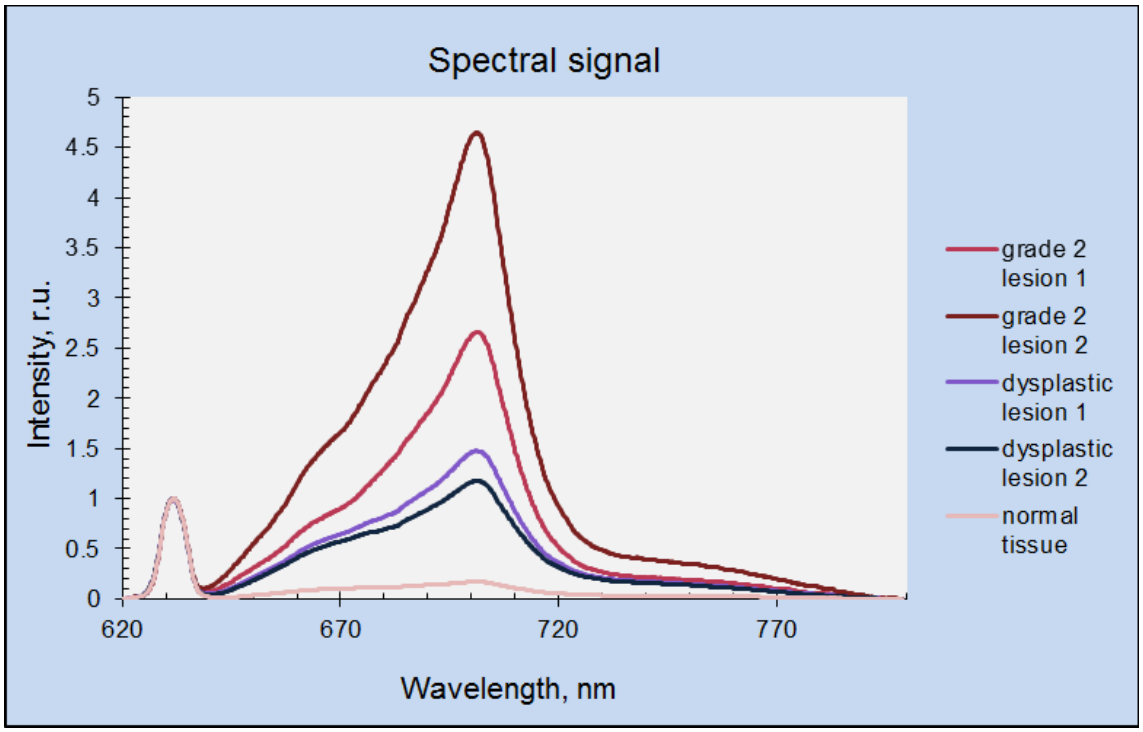

Figure 2.16 *Example of fluorescence spectra of the Protoporphyrin-IX accumulation in the bladder tissue of a patient.*

For the fluorescence intensity estimation we have measured the areas under the fluorescence curves on the spectrograms (at the range of 650-780 nm) from different parts of the bladder walls. Fig. 2.17 presents the area values under the fluorescent signals and their average for normal, inflamed, dysplastic and tumorous tissues.

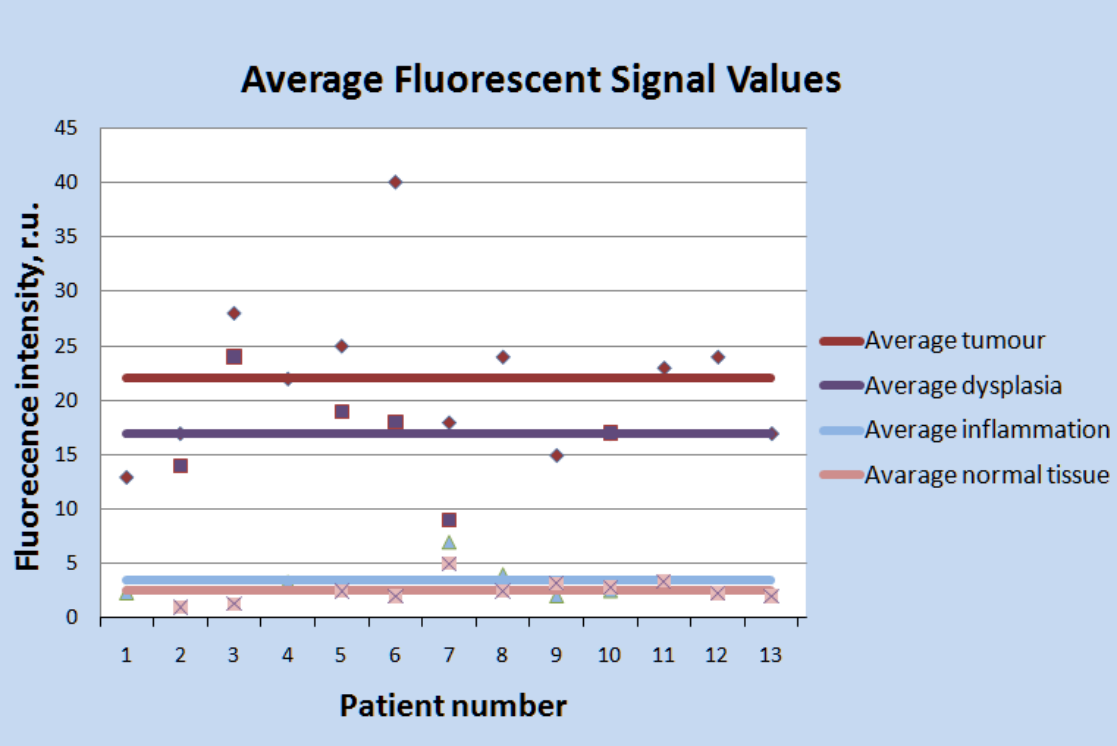

Figure 2.17 *Average values of fluorescence intensities.*

The intensities of normal and inflammatory tissues were much lower than cancerous and precancerous tissues. In order to estimate quantitatively the differences in the fluorescence intensities the average intensities of the fluorescence signal values of tumors, dysplastic, and inflammatory tissues, were normalized by dividing them by the average fluorescence intensity, obtained from normal tissues. The average normalized intensities from the inflammatory, dysplastic and timorous (from CIS to grade 2) tissues were about 1.4, 6.6 and 8.8 times higher than those from the normal tissue, respectively.

Fig. 2.17 shows that the non-tumoral tissues (inflammatory and normal) have a lower dispersion of the fluorescence intensity as compared to the cancerous and pre-cancerous tissues. Particularly small signal differences were seen for the dysplastic tissues and CIS cases. Such results can be explained by cell structure changes which are almost unnoticeable for spectroscopic methods, and can be fully observed only after the histological studies.

Even though the fluorescence signals for some tissue states could be hardly differentiated, their average signals still differed from each other, which allowed for the assessment of the average concentrations of the photosensitizer in different pathological bladder tissues.

The results of the fluorescence signal normalization enabled us calculate approximate concentrations of the PpIX for the first layers of the phantoms, simulating different states of

the bladder wall. By comparing the intensity of ALA-induces fluorescent signals from normal tissues and different concentrations of the PpIX in the Intralipid solutions, it was previously determined that the accumulation of the PpIX in the normal tissue is about 1 mg/l. Thus, a value of 1 mg/l was taken as a basic concentration of the PpIX for the phantoms, reproducing normal bladder tissue. Thereby, the PpIX concentrations for phantoms, simulating inflammatory, dysplastic and timorous tissues were determined to be 1.4 mg/l, 6.6 mg/l and 8.8 mg/l, respectively.

2.4.2 Phantom and Experimental Construction

The phantoms for the fluorescence signal estimation were also three-layered, and consisted of Intralipid (2% and 1.6% concentrations for the third and second layers, respectively), 5% gelatin and polystyrene scattering particles in the first layers at the concentration of 10^7, 10^9, and 10^{10} particles per ml for the spheres having respectively 5.09, 0.53 and 0.05 μm diameters. The “Alasens" drug is not a photosensitizer itself, but during the chemical reactions is converted into protoporphyrin IX, which has a distinct fluorescence in the red wavelength range. Synthesized PpIX production Alchem was used in order to study the spectral properties of PpIX. To compensate its poor solubility PpIX was first dissolved in dimethyl sulfoxide (DMSO) and then diluted with saline solution to the required concentrations. The first layer of the phantoms differed from each other by their fluorescence properties due to the variations of concentrations of the Protoporphyrine-IX photosensitizer between 1 mg/l and 12 mg/l.

The experimental setup for the measurements of fluorescent back-scattered light areas was similar to the construction, described in the Section 2.1. The fluorescent and back-scattered laser signals were acquired by a highly sensitive black-and-white camera (VideoScan, 16 bit). The time of camera exposition was 400 ms and 1 ms, and amplification was 300 and 0, respectively to the type of the measured signal (back-scattered or fluorescence light). The distance from the objective (16 mm, 1:1.4) to the phantom was 11.8 cm, from the fiber (with diameter d = 200 μm) end to the microlens 20 mm, from the lens to the phantom surface 68 mm. Tissue illumination was provided by a 630 nm diode light source through an

optical fiber. The light was collimated by an optical lens. The distance from the optical fiber to the lens was 20 mm, from the lens to the sample 68 mm. Fluorescence images of the phantom surfaces were acquired with the use of two red-glass filters RG-18 of 5 and 1.5 mm thick for cutting off the range of wavelengths of the laser light. The absorption curve of the filter is presented in the Fig. 2.18.

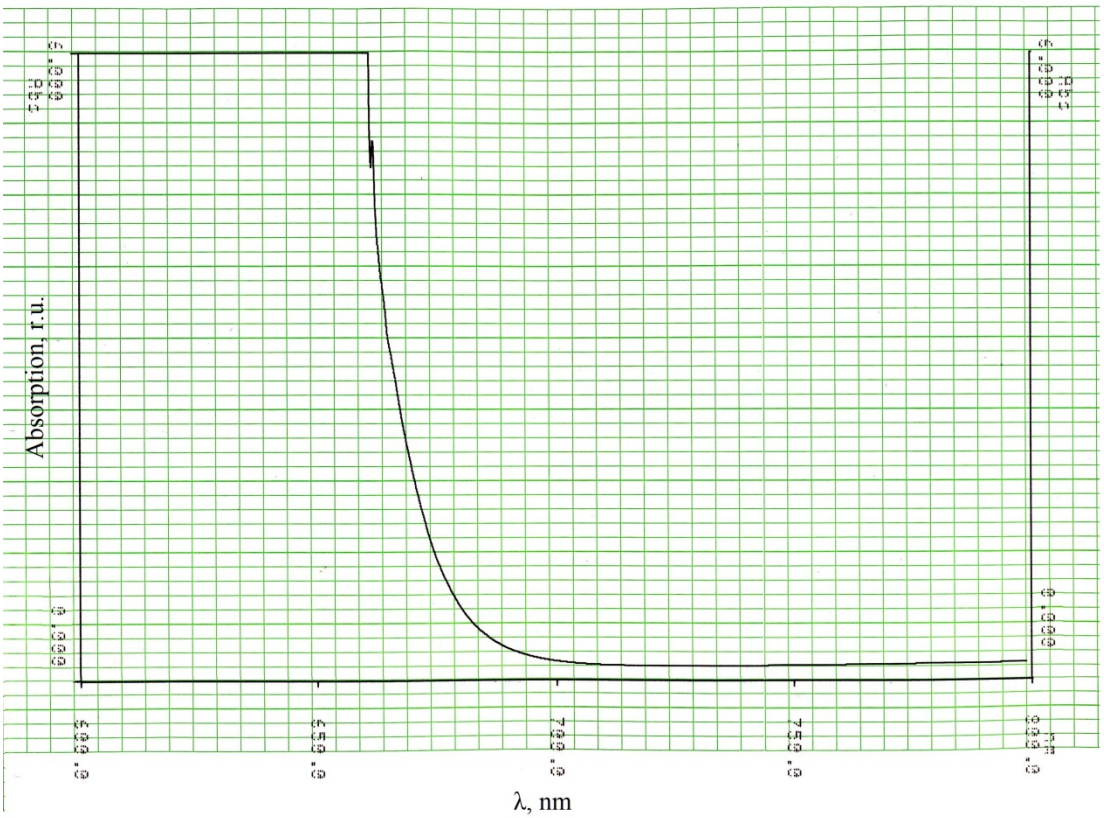

Figure 2.18 *Absorption curve of the RG-18 filter (measured with HITACHI U-3400 Spectrophotometer).*

Image examples of back-scattered fluorescence and laser light, obtained by the described method, are presented in the Fig. 2.19 and Fig. 2.20, respectively. The initial size of the images was 776 per 582 pixels. The back-scattered fluorescent signal increase, caused by the growth of the photosensitizer concentration, can be visually detected the human eye (see Fig. 2.19). Thus, we consider the sensitivity of the fluorescence measurements to be much higher than that of the measurements of the laser back-scattered signal. The higher sensitivity of the presented method to the fluorescence measurements to compare with the DR measurements can be explained by more pronounced target of detection – a photosensitizer compare to the micro changes at a cellular level.

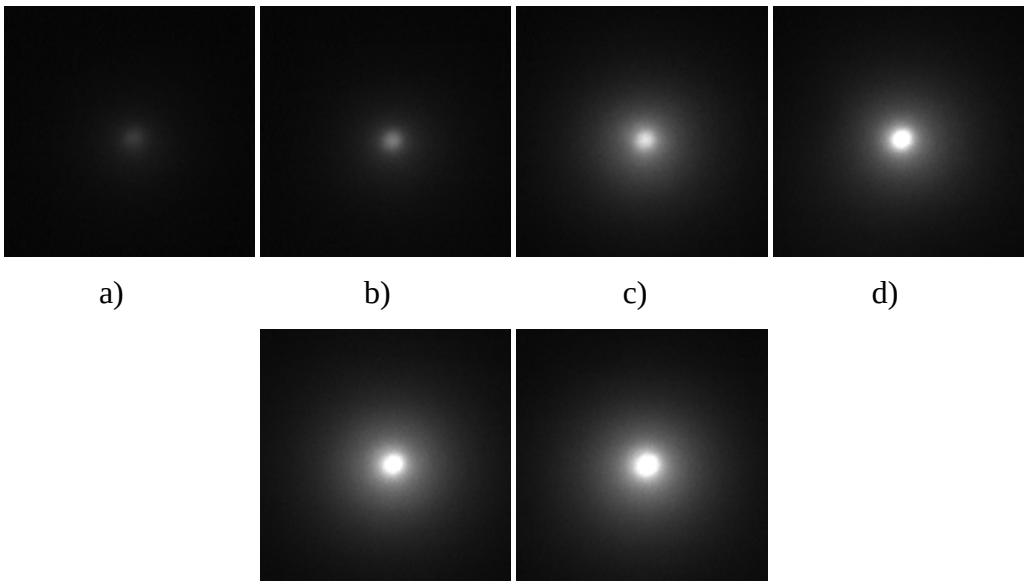

Figure 2.19 *Acquired images of the fluorescence light distributions on the surface of the phantoms with different concentration of Protoporphyrin-IX: a) 1 mg/l, b) 1.4 mg/l, c) 6.6 mg/l, d) 8.8 mg/l, e) 10 mg/l, f) 12 mg/l.*

Figure 2.20 shows diffuse-reflected signal from the surface of the fluorescent phantoms, acquired without a filter.

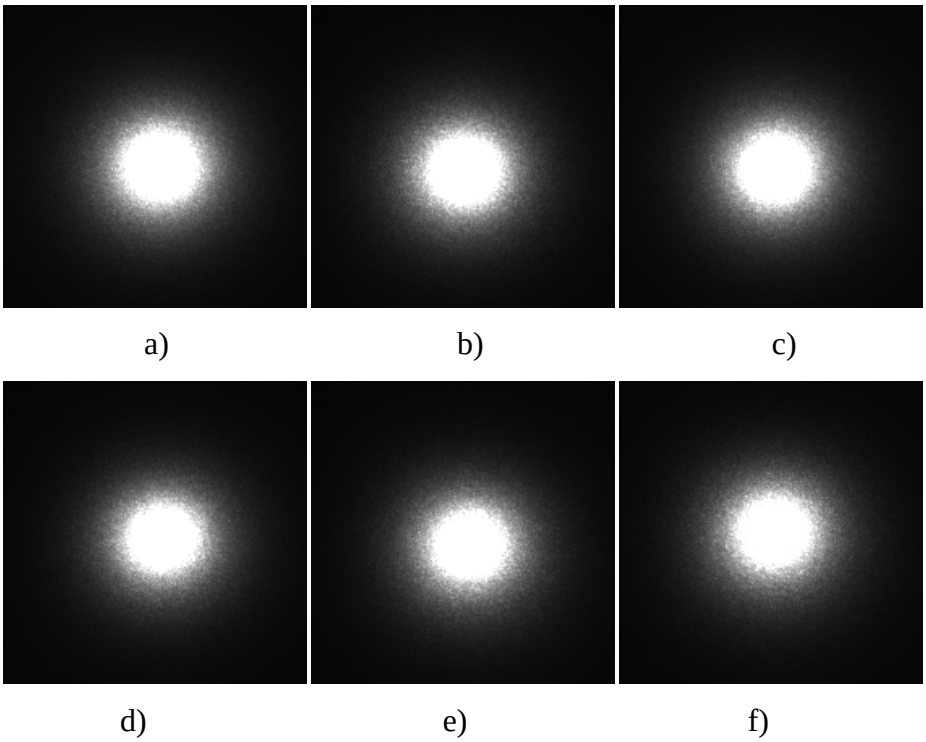

Figure 2.20 *Acquired images of the back-scattered laser light distributions on the surface of the phantoms with different concentration of Protoporphyrin-IX: a)1 mg/l, b) 1.4 mg/l, c) 6.6 mg/l, d) 8.8 mg/l, e) 10 mg/l, f) 12 mg/l.*

In order to compare the sensitivity of the measurements made by the presented technique with the spectroscopic technique (commonly used for estimations of photosensitizer accumulation), the spectroscopic measurements were also made on the same phantoms. The experimental construction was similar to the one described in the Section 2.5.1.

2.4.3 Results and Discussion

2.4.3.1 Fluorescence Signals

The areas of the diffusely reflected fluorescence light, obtained on the surfaces of the phantoms with different PpIX concentrations, ranged from 0 to 6600 relative units (see Fig. 2.21and 2.22). The linear approximation of mean area value evolution is presented on Fig. 2.22. The measurements show a stabile growth of the area values with the growth of the PpIX concentration inside the first layers of the phantoms.

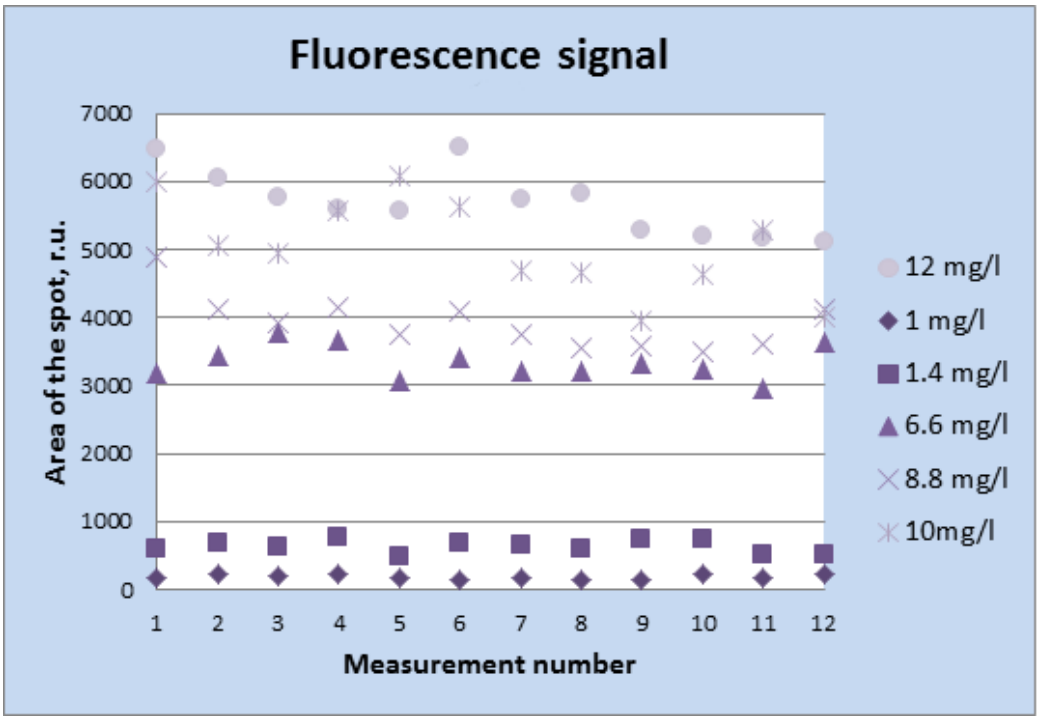

Figure 2.21 *Areas of the fluorescent signal on the surfaces of the phantoms, measured at the threshold of 0.12.*

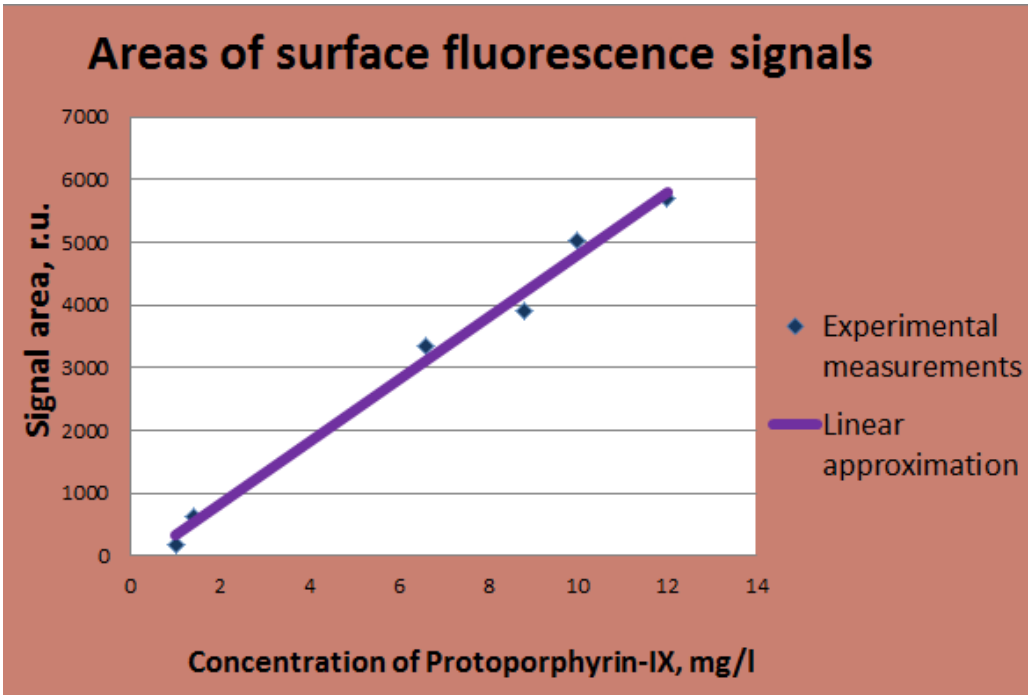

Figure 2.22 *Detection of concentration of the fluorescent agent by measuring the areas of Diffuse-Reflected light.*

The spectroscopic measurements of the fluorescence signal (Fig. 2.23) showed lower differentiation in the signals. The intensity values and the ratio of the intensity signals were compared with the data from the imaging method (see Table 2)

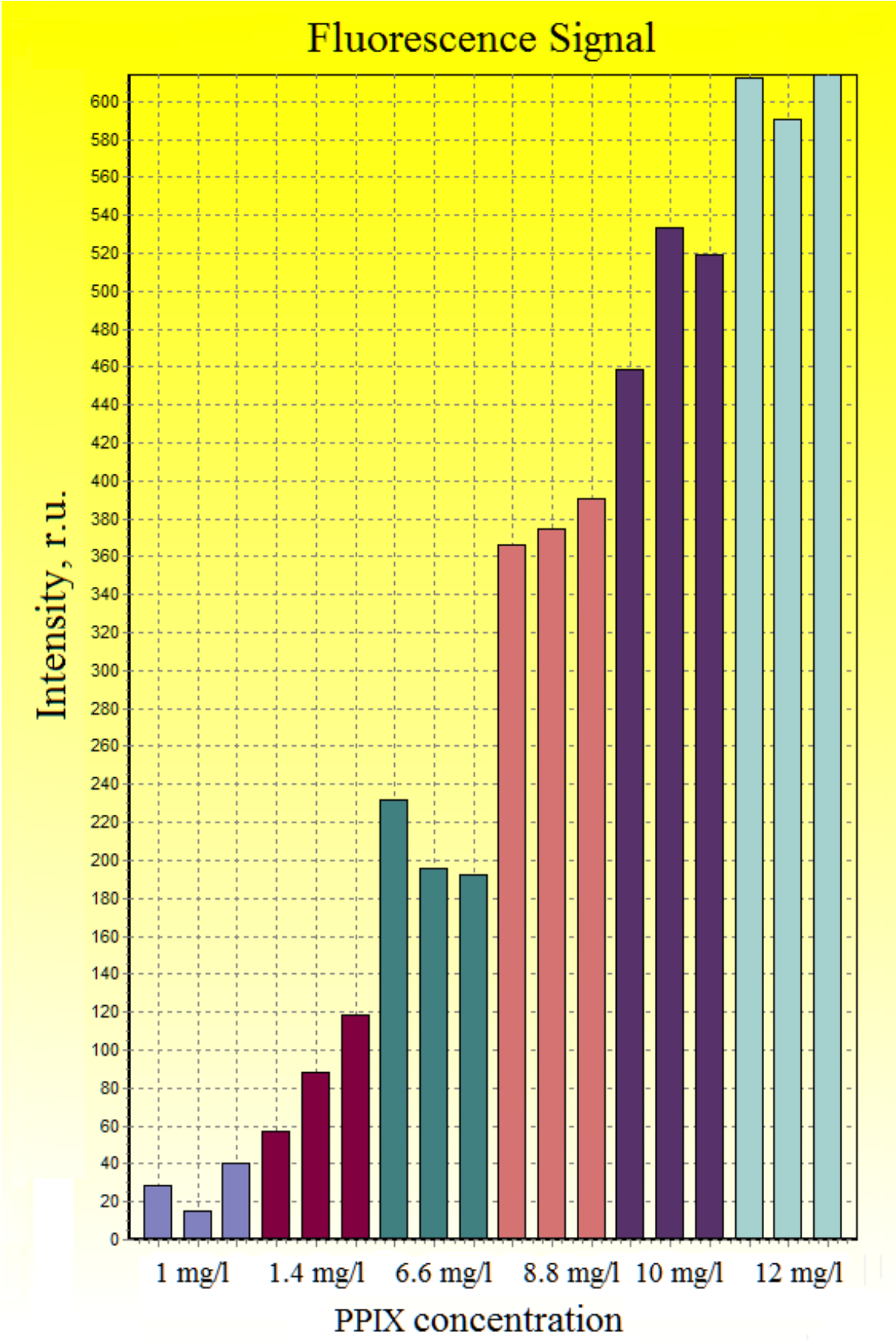

Figure 2.23 *Intensities of fluorescence spectra form the phantoms with different concentration of Protoporphyrin-IX.*

Measurement type	Data type	1 mg/l	1.4 mg/l	6.6 mg/l	8.8 mg/l	10 mg/l	12 mg/l
Spectral measurements	Mean intensity value	28	88	207	377	503	605
	Ratio to minimal signal	1	3.1	7.4	13.5	18	21.6
Surface DR imaging	Mean area value	184	632	3339	3922	5041	5693
	Ratio to minimal signal	1	3.4	18.2	21.3	27.4	31

Table 2 *Sensitivity of the imaging method of area measuring of fluorescence light to different photosensitizer concentrations.*

The processing results of the fluorescence images, and their comparison with the spectroscopic measurements show that the area measuring method has a higher sensitivity than the spectroscopic technique. Such sensitivity augmentation can be explained by the accumulation and detection of more photons due to measurements on larger areas. One of the main advantages of a high sensitivity is high accuracy and possibility to detect less visible differences between the photosensitizer concentrations.

2.4.3.2 Back-Scattered Laser Signals

Contrary to the fluorescence signals, the range of the area values of the back-scattered laser signal (measured without the RG filters) was not large: from 4250 to 5700 relative units (see Fig. 2.24). Thus the signal was stable for all the photosensitizer concentrations, though less accurate than the fluorescence signals.

It was also important to examine the influence of the fluorophores presence in the media on the scattering properties, and the possibility to detect the small internal changes of the scatterers. The results of the area measuring of the back-scattered signals, obtained without the use of the dedicated RG-filter, show that the matrices of the backscattered light are almost indistinguishable from each other (see Fig. 2.25). Thus, the presence of the fluorophores, and

hence the expenditure of the light energy for fluorescence excitation, does not affect the surface light distributions of the DR as much as to prevent detection of the small changes in size, concentration and absorption properties of a media. Thereafter, the presented method of analysis of the diffuse-reflected light can be associated to the study of the fluorescence properties of the tissues with accumulated photosensitizer in order to improve the sensitivity and specificity of the method.

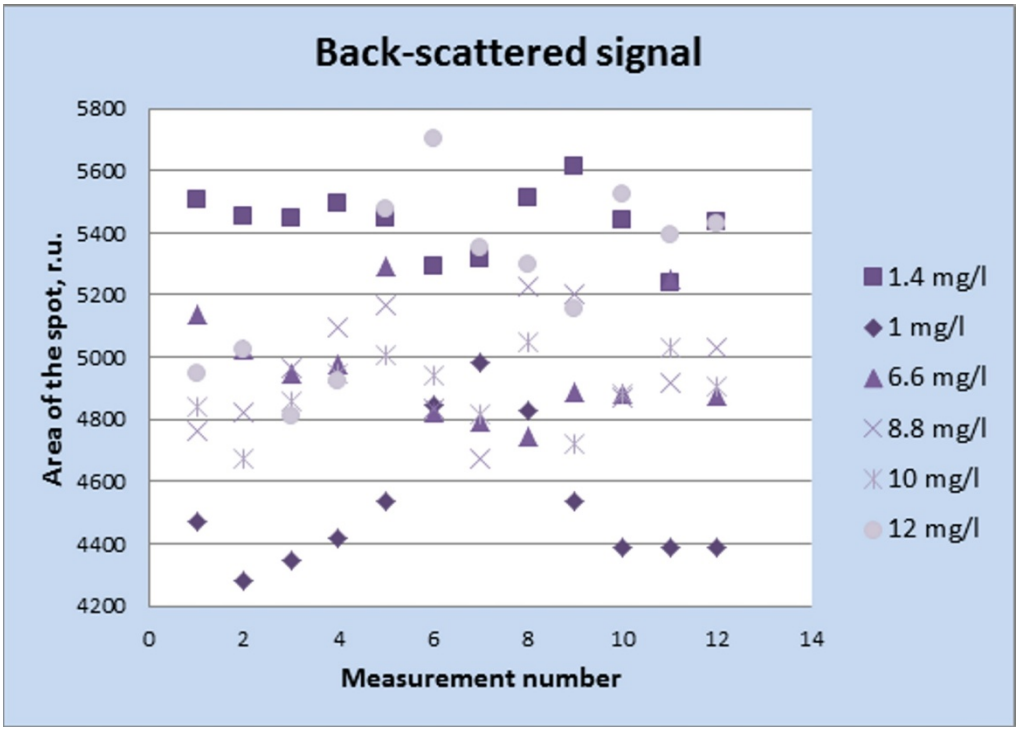

Figure 2.24 *Areas of the back-scattered laser signal on the surfaces of the phantoms, measured at the threshold of 0.3.*

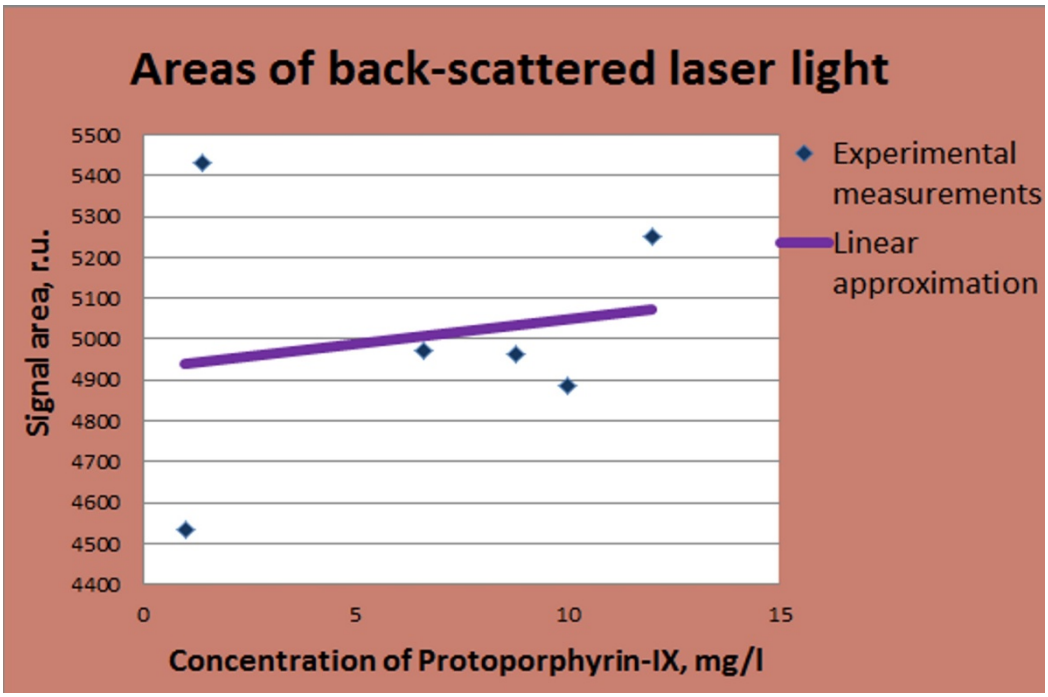

Figure 2.25 *Linear approximation of Diffuse-Reflected laser signals from the surface of the phantoms with different concentrations of the Protoporphyrin-IX.*

2.5 Conclusion

The sensitivity tests on the phantoms of the proposed method have shown that it can efficiently distinguish the differences in sizes, concentrations, and absorption properties of the consistence of the media at a micron level, and thus can be applied for differentiation of the UB tissues at early cancerous stages. The chosen concentration of 10^7 is lower than that arising in the real conditions, and the sizes of the scattering particles can be compared with the small scatterers of a cell, such as nucleus, mitochondria and Golgi apparatus.

The experimental results show different changes of the diffuse-reflected light signals depending on the scatterers' properties. The most significant differences are seen for the changes of absorption and when all the changes occur together (nuclear size growth, nuclear concentration growth, absorption growth). The lowest difference is seen between the nuclear size and population density growth. The sensitivity of the fluorescence measurements is higher than of the measurements of the back-scattered signal. This observation can be explained by more detectable target of analysis – photosensitizer compare to the cell nucleus.

Moreover, in comparison with the point analysis, and due to the larger number of photons during the area measuring of the diffuse-reflected light, the measurement errors are reduced, which makes the sensitivity of the presented method to the photosensitizer concentration higher.

References:

[1] Van Staveren H. J., J. F. Beeu, J. W. H. Ramaekers, M. Keijzerg and W. M. Star, Integrating sphere effect in whole bladder wall photodynamic therapy: I. 532 nm versus 630 nm optical irradiation, Phys. Med. Biol. 39, 947-959, 1994.

[2] Hanssen L., Integrating-sphere system and method for absolute measurement of transmittance, reflectance, and absorptance of specular samples, Appl. Opt. Vol. 40, No. 19, pp. 3196-3204, 2001.

[3] Welch A. J., M. J. C. van Gemert and W. M. Star, Definitions and overview of tissue optics, at Optical-Thermal Response of Laser-Irradiated Tissue, 2d edition, by A. J. Welch and M. J. C. van Gemert (eds.), Springer, 2011.

[4] Beck T., W. Beyer, T. Pongratz, W. Stummer, R. Waidelich, H. Stepp, S. Wagner, R. Baumgartner: Proceedings of SPIE-OSA Biomedical Optics, SPIE 5138, 2003.

[5] Swartling J., Biomedical and atmospheric applications of optical spectroscopy in scattering media, Dissertation thesis, Lund Institute of Technology, Lund, Sweden, 2000.

[6] Firbank M., D. T. Delpy, A design for a stable and reproducible phantom for use in near infra-red imaging and spectroscopy, Phys. Med. Biol., 38, 847-853, 1993.

[7] Lualdi M, Colombo A, Farina B, Tomatis S and Marchesini R., A phantom with tissue-like optical properties in the visible and near infrared for use in photomedicine Lasers Surg. Med. 28 237–43, 2001.

[8] Firbank M and Deply D T, An improved design for a stable and reproducible phantom material for use in near-infrared spectroscopy and imaging Phys. Med. Biol. 40 955–61, 1995.

[9] Shimada M, Yamada Y, Itoh M and Yatagai T, Melanin and blood concentration in human skin studied by multiple regression analysis: experiments Phys. Med. Biol. 46 2385–95, 2001.

[10] Hebden J. C., Time-resolved attenuation of transmitted laser pulses by a homogeneous scattering medium, Optics Letters, Vol. 17, Issue 6, pp. 444-446, 1992.

[11] Studinski R C and Vitkin I A., Methodology for examining polarized light interactions with tissues and tissuelike media in the backscattering direction J. Biomed. Opt. 5 330–7, 2000.

[12] Passos D., J. C. Hebden, P. N. Pinto, R. Guerra, Tissue phantom for optical diagnostics based on a suspension of microspheres with a fractal size distribution, Journal of Biomedical Optics 10(6), 064036, 2005.

[13] FawzyY.S. and Zeng H. Determination of scattering volume fraction and particle size distribution in the superficial layer of a turbid medium by using diffuse reflectance spectroscopy Appl. Opt. 45 3902–12, 2006.

[14] Wagnieres G., Cheng S., Zellweger M., Utke N., Braichotte D., Ballinni J. and ven den Berg H., An optical phantom with tissue-like properties in the visible for use PTD and fluorescence spectroscopy Phys. Med. Biol. 42 1415–26, 1997.

[15] Van Staveren H. J., Christian J. M. Moes, Jan van Marie, Scott A. Prahl, and Martin J. C. van Gemert, Light scattering in Intralipid-10% in the wavelength range of 400–1100 nm, Applied Optics, Vol. 30, Issue 31, pp. 4507-4514, 1991.

[16] Flock ST, Jacques SL, Wilson BC, Star WM, van Gemert MJ., Optical properties of Intralipid: a phantom medium for light propagation studies, Lasers Surg Med.;12(5):510-9, 1992.

[17] Cubeddu R, Pifferi A, Taroni P, Torricelli A and Valentini G A solid tissue phantom for photon migration studies Phys. Med. Biol. 42 1971–9, 1997.

[18] De Grand A. M., Stephen J. Lomnes, Deborah S. Lee, Matthew Pietrzykowski, Shunsuke Ohnishi, Timothy G. Morgan, Andrew Gogbashian, Rita G. Laurence, and John V. Frangioni, Tissue-Like Phantoms for Near-Infrared Fluorescence Imaging System Assessment and the Training of Surgeons, J Biomed Opt.; 11(1): 014007, 2006.

[19] Lehmann T., C. Gonner, K. Spitzer, Survey: interpolation methods in medical image processing, IEEE Transactions on Medical Imaging 18, 11, 1999.

[20] Poth M. , T. Szakall, Spatial and Frequency Domain Comparison of Interpolation Techniques in Digital Image Processing, 10th International Symposium of Hungarian Researchers on Computational Intelligence and Informatics, 591-600, 2009.

[21] Maeland E., On the comparison of interpolation methods IEEE Trans.Med. Imag., MI-7, 1988.

[22] Jones R., I. Svable, Algorithms for the Decomposition of Gray-Scale Morphological Operations, IEEE Transactions on Pattern Analysis and Machine Intelligence 16, 6, 581-588, 1994.

[23] Shapiro L., G. Stockman: Computer Vision Upper Saddle River, NJ: Prentice-Hall, 2001.

[24] Gmurman V., I. Berenblut: Fundamentals of Probability Theory and Mathematical Statistics, American Elsevier Pub. Co., New York, 1968.

[25] Fisher R., Statistical Methods for Research Workers, first ed, Edinburgh: Oliver & Boyd, 1925.

[26] Prahl S., Optical Absorption of Hemoglobin, Oregon Medical Laser Center (http://omlc.ogi.edu/spectra/hemoglobin/), 1999.

[27] Loschenov V. B., V. I. Konov, A. M. Prokhorov, Photodynamic therapy and Fluorescence diagnostics, Laser Physics vol. 10 No 6, pp. 1188-1207, 2000.

3

CHAPTER

Calculation of Optical Scattering Parameters of Bladder Tissues and Tissue-Like Phantoms

"…there is no royal road to geometry."

Euclid

3.1 Light Scattering in Biological Tissues

In order to understand the phenomenon of light interactions with highly scattering media like biological tissues it is helpful to study the characteristics of the structures, responsible for the scattering effects on a microscopic, i.e. extra-cellular, cellular or sub-cellular, level. The contribution of each type of biological constituent to the overall scattering properties of the tissue will depend on the individual scattering properties of each diffusing particle and its relative concentrations in the tissue.

Light scattering in biological tissues is caused by the presence of different inhomogeneities inside the tissue matrix and inside cells. The scattering process occurs at the interfaces between the tissue constituents from cellular organelles to extracellular matrix compounds of various sizes, concentrations and refractive indices [1]. The scattering and reflection of light arise due to a relative refractive index mismatch at the boundaries between two media or structures, like the extracellular fluid and the cell membrane. Cells vary greatly in size, however for most of the bladder epithelial tissues it is about 10-20 μm. The cells consist of three main components: the cell membrane, the cytoplasm and the nucleus. The membrane, which constitutes the cell outer boundary, is made up of a phospholipid bilayer, approximately 8 nm in thickness, with numerous proteins embedded in it. The cytoplasm is the intracellular matrix held within the bounds of the cell membrane. It consists of the cytosol, a water-based fluid within which the other constituents are suspended, of some non-functioning units (lysosomes, collagen and elastin fibers), and of organelles, each of which has a special function in the cell mechanism, like the Golgi apparatus and the mitochondria.

The size of the tissue scatterers plays an important role in the scattering process. The largest cell's organelle is the nucleus which constitutes the control centre of the cell. The size of the nucleus varies with the cell type, and has an average diameter of 5 μm in normal state [2]. Cell nuclei contain most of the cell's genetic material, organized as DNA molecules in complex with a large variety of proteins to form chromosomes. The genes within these

chromosomes are the cell's nuclear genome. General function of the nucleus is to control the activities of the cell by regulating genes expression, and by keeping their integrity. The main structures making up the nucleus are a nuclear envelope, a triple cell membrane and membrane (enclosing the organelle and unifying its contents from the cellular cytoplasm), and the nucleoskeleton. Nuclear transport is crucial to cell function, as movement through the pores is required for both gene expression and chromosomal maintenance. The interior of the nucleus has non-uniform contents, formed by proteins, RNA molecules, and parts of the mitochondria. Cell nuclei usually have strong impact to the light scattering due to teirr high concentrations, sizes and refractive indices. A hypothesis asserting that the main contribution to the light scattering from cells is caused by the nucleus and cell membranes was presented by Backman *et al.* [3] and Beuthan *et al.* [4]. In the first work, the conclusion is based on the result of the light scattering spectroscopy of polarized light and analysis of the spectrum of a single backscattering component of the light scattered from cells. In the second work, based on the results of phase-contrast spectroscopy, the obtained data has shown that the single phase shift of the mitochondria was small in comparison with the total phase shift. Thus the nucleus and the membranous structures of the tissue gave the most considerable phase shift of the cell. Thereafter, based on the structure, size, refractive index and concentration of cell nuclei, they were considered as main scatterers of bladder mucosa. Even though, the other mucosal structural elements have to be particularly discussed.

3.2 Small Scatterers and Mitochondrial Contribution to Light Scattering in Bladder Epithelium

Dimension of mitochondria and lysosomes [5] are much smaller than the nucleus diameter, and is of the same order of magnitude compared to the wavelengths in the visible range. However, their contribution to the scattering process can be still described by the scattering theory for “large” particles, first introduced by Gustav Mie in 1908 [6]. Scattering by smaller particles can be described by the Rayleigh scattering approach, which shows a stronger dependence on the wavelength compared to the Mie scattering theory implying for larger

scatterers. Mie scattering occurs preferably in a forward direction, while at Rayleigh scattering the light is uniformly distributed in forward and backward directions. In most of the biological tissues, photons are scattered anisotropically in the forward direction [7], [8]. The sizes of the tissue scatteres, their contribution to the light scattering and description of the scattering theories are discussed in this section of the present chapter.

The smallest scatterers in the tissue are small cell organelles such as endoplasmatic reticulum, component parts of the Golgi apparatus, and extracellular components like individual elastin and collagen fibers. The scattering process, not accompanied with the change of the initial frequency of the electromagnetic wave, is called elastic scattering. One of the examples of the elastic scattering is Rayleigh scattering, which corresponds to the scattering of particles much smaller in size than the wavelength of the incident radiation [9]. One of the main features of Rayleigh scattering for small particles is low angular dependence in the scattering distribution, thus isotropic character of the scattering. At Rayleigh scattering the intensity of the light scattering is inversely proportional to the fourth power of the wavelength. Such effect means that at short wavelength the scattering intensity will be higher than at longer wavelength with the same initial illumination intensity.

3.2.1 Golgi Apparatus and Lysosomes

Golgi apparatus is a reticulate membrane structure, located near the cell nucleus of an eukaryotic cell, and consisting of several components of various sizes, forming a single structure of about 200-400 nm in diameter [10]. It is composed of stacks of membrane-bound structures - cisterns, where the main element, a dictyosome, is a separate area of membranes, accumulated together, close to each other. Each individual cisterna has a diameter of about 1 mm and variable thickness with common approaching in the center of the membranes, and expansion at the off-central areas. The number of the stacks is typically about 60 [11]. Besides the densely packed flat cisterns, groups of small vacuoles are observed in the perifocal areas of the Golgi apparatus. Usually, the dictyosome zone of Golgi apparatus is divided into three main sections, representing the developement stages from initial forming to

mature. At the formed (mature) sections of the dictyosomes, an area of tubular elements and small vacuoles is attached to the last membrane cistern which is known as the trans Golgi network [12]. A group of larger vacuoles – a union of small vacuoles, forming the secretory vacuoles, is located more distally at the dictyosome. During the cell division the networks of the Golgi apparatus decompose to dictyosomes. The total number of dictyosomes grows with cells. The Golgi apparatus serves for the excretion of the substances such as proteins, lipoproteins and steroids outside of the cells. There is usually one Golgi Apparatus per cell, which, together with its relatively small size, gives a low influence on the forward light scattering in comparison with bigger and more densely packed tissue scatterers.

Lysosomes are products of endoplasmic reticulum and Golgi apparatus activities in cells. They are similar to secretory vacuoles by their main role - participation in the processes of intracellular decomposition of exogenous and endogenous biological macromolecules. The presence of lysosomes of various types in the cells of different organs is related to the necessity of transfer of hydrolytic enzymes for intracellular decomposition. Under electron microscopy, lysosomes appear in groups of vesicles of about 0.2-0.4 μm in size, separated by a single thin membrane. The content of lysosomes is very uniform: from isolate vacuoles to densely packed membranes. In the fraction of lysosomal vesicles with a homogeneous, unstructured content, there are vesicles filled with dense material containing, in turn, vacuoles, clusters of dense homogeneous membranes and particles. Also, not only parts of the membrane can be seen inside the lysosomes, but also fragments of mitochondria and of endoplasmic reticulum, which forms a complex structure. Due to their small sizes and low density, none of Golgi apparatus and lysosomes were not taken into account in our study.

3.2.2 Mitochondria

The mitochondria typically present in eucaryotic cells. Their main function is related to the cell energy, provided by the oxidation of organic compounds and their decomposition through the synthesis of Adenosine-5'-triphosphate (ATP). The initial stages of oxidation (anaerobic oxidation) of carbohydrates do not require the participation of oxygen. The mitochondria supply the cells with the energy, thus the number of mitochondria reflects the cell's need for energy.

The dimensions and sizes of the mitochondria are not the same in all tissues. In average, they are about 0.5-1.5 μm [13] in size, and their quantity in a cell varies from several mitochondria to few thousands. Due to their relatively large size and sometimes high concentration in a cell (depending on the oxygen demand in the organ), and the possibility to be well-dyed by the osmic fixation, mitochondria are visible under conventional microscopy. Unlike the sizes and density of mitochondria, the structure of the latter is regular: like the nuclei, the mitochondria are surrounded by a double-layered phospholipid thin membrane (of several nanometers thick), restraining the inner content. The matrix of a mitochondrium consists of homogeneous substance of DNA molecules, ribosomes, and sometimes magnesium and calcium salts.

The insufficient number of data on the characteristics of mitochondria in the bladder wall, given in literature, does not allow to make a precise estimation of their contribution to intensities of the light scattering and absorption in the bladder tissue. In this thesis we present an example of possible calculation of the mitochondrial contribution to the scattering coefficients.

The algorithm of the estimations of the scattering parameters for the mitochondria in the bladder tissue is described below in this Chapter. We consider that the scattering occurs on the mitochondria surrounded by a cytoplasm with respective refractive indices of 1.42 for the mitochondria organelle itself, and 1.37 for the surrounding medium (cell cytoplasm) [13]. The histological studies of the bladder wall tissue show that the mean mitochondrial size is about 0.5 μm [14]. In the cells, which do not require a large amount of oxygen (like urothelial cells), the volume fraction of the mitochondria is 2-8% [15], which correspond to about 200 mitochondria per cell.

The results of Mie calculations performed at 510.6 nm wavelength by the method described in Section 3.5.1, show that the scattering coefficient for the mitochondria in the bladder epithelial tissue (μ_s = 2.54 cm^{-1}) is much smaller than the one for cell nucleus (which is usually about (μ_s = 50-250 cm^{-1}), and thus is neglected in our study. The contribution of the mitochondria (together with other biological scatterers of a small size ($\leq$ 0.5 μm)) to the scattering process was considered in this thesis for anisotropy factor as a reducing component (mitochondrial anisotropy factor of light scattering was estimated to be about g = 0.884). However, the mitochondrial influence on the scattering process can be more significant for some tissues than it was estimated in this study. This is rather important for solving inverse problems of DR light analysis, which are not presented in this thesis. For example, for the organs, like liver and brain, in which the oxygen needs are high, mitochondria can serve as the main scatterers, or can give a significant impact to the DR light signal. Besides, mitochondria has one of the strongest influence on the cell death [16], and they can decrease in their quantity and sizes with the tumour development [17], which can influence the DR light responses on the surface of the tumorous tissues. Thus, in case of inverse problems, the study on mitochondrial content has to be held prior to interpretation of experimental and mathematical results.

3.3 Electromagnetic Wave Theory

The mathematical part of this thesis consists of two modelling methods, complementary to each other. This Chapter describes a modelling method of light scattering and absorption by tissues, based on the fundamental electromagnetic wave theory. Such method allows to obtain more accurate analytical solutions and to obtain scattering and absorption parameters, while another one (a Monte Carlo-based), with the use of this optical parameters, allow to take into account light transport in multi-layered tissue structure. The Monte Carlo simulation algorithm and analysis are presented in the next Chapter.

The light propagation is described by two theories, considering the dual nature of light: particles and waves. In general, in tissue optics, both electromagnetic wave and flux of photons descriptions of light appear complementarily. However, at the large wavelength (due

to lower impulse and energy) the corpuscular properties are inferior to the properties of the wave. As the Mie scattering theory is based on the Maxwell's equations for the electromagnetic waves, the present chapter presents the description of the wave theory.

The scattering process of electromagnetic waves is based on redistribution of the light with changing electric and magnetic fields, by re-emission of the energy of initial wave by a scattering particle into a solid angle. The brightness of initial and scattered light depends on the amplitudes of the waves**.** In this thesis we present only few main steps of mathematical description of the wave propagation into a medium. More detailed description can be found in [6].

The universal Maxwell's equations are basic equations for electromagnetic field inside a continuous medium, expressing four vector functions: *E* - electric field intensity, *B* - magnetic induction, *H* - magnetic field intensity, and *D* - electric induction, and are written as

$$\begin{aligned} \nabla \cdot D &= \rho\ , \\ \nabla \times E + \frac{\partial B}{\partial t} &= 0, \\ \nabla \cdot B &= 0, \\ \nabla \times H &= J + \frac{\partial D}{\partial t}, \end{aligned} \tag{7}$$

where *J* is the current density, and ρ the volume charge density. In order to take into consideration the properties of the medium and their influence on electromagnetic waves, Maxwell's equations are completed by the expressions for *D* and *H:*

$$D = \varepsilon_0 E + P, \tag{8}$$

$$H = \frac{B}{\mu_0} - M, \tag{9}$$

where *P* is the electric polarization field, and *M* the magnetization field. The two universal constants (permittivity and permeability) of the free space are represented by ε_0 and μ_0, respectively. The constitutive relations are:

$$J = \sigma E, \tag{10}$$

$$B = \mu H, \tag{11}$$

$$P = \varepsilon_0 \chi E, \tag{12}$$

where σ is the conductivity, μ the permeability, and χ the electric susceptibility. It was found [6], [18] that a time-harmonic electromagnetic field *(E, H)* in a linear, isotropic, homogeneous medium must satisfy the following wave equations

$$\nabla^2 E + k^2 E = 0,$$
$$\nabla^2 H + k^2 H = 0, \quad (13)$$

where $k^2 = \omega^2 \varepsilon\mu$, ω is angular frequency, and $\nabla \cdot E = 0, \ \nabla \cdot H = 0$.

E and *H* are interdependent: $\nabla \times E = i\omega\mu H, \quad \nabla \times H = -i\omega\varepsilon E$.

For the plane wave the Maxwell equations are

$$k \cdot E_0 = 0,$$
$$k \cdot H_0 = 0,$$
$$k \times E_0 = \omega\mu H_0, \quad (14)$$
$$k \times H_0 = -\omega\varepsilon E_0.$$

The wave vector of a homogeneous wave at the conditions of transversality may be written as $k = k' + ik'' = \frac{\omega N}{c}$, where *k'* and *k''* are nonnegative, *c* is the speed of light in vacuum, and *N* is the complex refractive index *N = n + ik*, where *n* and *k* are nonnegative. Hereinafter in this study, for simplicity, the real part *(n)* of the refractive index *(N)* will be called as "refractive index".

In the present study, mathematical approximation of light distribution in the epithelial layers is made for the spherical scatterers. Thus, for the case of light scattering by a sphere, supposing that a plane x-polarized wave is incident on a homogeneous isotropic sphere of radius *a*, the electric and magnetic fields can be expanded in vector spherical harmonics in an infinite series:

$$E_i = E_0 \sum_{n=1}^{\infty} i^n \frac{2n+1}{n(n+1)} \left(Q_{o1n}^{(1)} - iF_{e1n}^{(1)} \right)$$
$$H_i = \frac{-k}{\omega\mu} E_0 \sum_{n=1}^{\infty} i^n \frac{2n+1}{n(n+1)} \left(Q_{e1n}^{(1)} + iF_{o1n}^{(1)} \right) \quad (15)$$

where Q_{omn}, Q_{emn}, F_{omn}, and F_{emn} are vector spherical harmonics, generated by functions satisfying the scalar wave equation in spherical polar coordinates. The expansions in vector harmonics of the internal field of the sphere *(E_1, H_1)* and the scattered field *(E_s, H_s)* are:

$$E_1 = \sum_{n=1}^{\infty} E_n \left(c_n Q_{o1n}^{(1)} - id_n F_{eln}^{(1)} \right),$$
$$H_1 = \frac{-k_1}{\omega\mu_1} \sum_{n=1}^{\infty} E_n \left(d_n Q_{e1n}^{(1)} + ic_n F_{oln}^{(1)} \right), \quad (16)$$

where $E_n = \frac{i^n E_0(2n+1)}{n(n+1)}$, and μ_s is the preambility of the sphere. The expansions of the scattered field can be written as:

$$E_s = \sum_{n=1}^{\infty} E_n(ia_n F_{e1n}^{(3)} - b_n Q_{o1n}^{(3)}),$$
$$H_s = \frac{k}{\omega\mu}\sum_{n=1}^{\infty} E_n(ib_n F_{o1n}^{(3)} + a_n Q_{e1n}^{(3)}) \quad (17)$$

where a_n, b_n, c_n, *and* d_n, are Mie coefficients, characterizing the scattering and absorption properties of scatterers and media. They will be determined in further sections of this chapter for each particular case of our modelling.

From the boundary conditions for the sphere and the surrounding medium, we can write four independent equations for the electro-magnetic fields (the field inside the sphere (E_1, H_1), and the scattered field (E_s, H_s)) in vector spherical harmonics:

$$E_{i\theta} + E_{s\theta} = E_{1\theta},$$
$$E_{i\varphi} + E_{s\varphi} = E_{1\varphi},$$
$$H_{i\theta} + H_{s\theta} = H_{1\theta}, \quad (18)$$
$$H_{i\varphi} + H_{s\varphi} = H_{1\varphi},$$

The four linear equations in the expansion coefficients can be obtained from the expansions of the scattered and internal fields, boundary conditions for the sphere and surrounding medium, the vector spherical harmonics for the expansions of the fields, and orthogonal sets of angle-dependent functions

$$j_n(mx)c_n + h_n^{(1)}(x)b_n = j_n(x),$$
$$\mu[mxj_n(mx)]'c_n + \mu_1\left[xh_n^{(1)}(x)\right]'b_n = \mu_1[xj_n(x)]',$$
$$\mu m j_n(mx)d_n + \mu_1 h_n^{(1)}(x)a_n = \mu_1 j_n(x), \quad (19)$$
$$[mxj_n(mx)]'d_n + m\left[xh_n^{(1)}(x)\right]'a_n = m[xj_n(x)]'$$

Where the size parameter x and the relative refractive index m are

$$x = ka = \frac{2\pi N a}{\lambda}, \quad (20)$$
$$m = \frac{N_1}{N} \quad (21)$$

N_1 and N are the complex refractive indices of particle and medium, respectively. The solutions of the linear equations (19) give the coefficients of the field inside the particle and scattering coefficients (see Section 3.6).

If we assume that the series expansion of the scattered field (E_s, H_s) (17) is uniformly convergent, then the relation between incident and scattered field amplitudes is:

$$\begin{pmatrix} E_{\parallel s} \\ E_{\perp s} \end{pmatrix} = \frac{e^{ik(r-z)}}{-ikr} \begin{pmatrix} S_2 & 0 \\ 0 & S_1 \end{pmatrix} \begin{pmatrix} E_{\parallel i} \\ E_{\perp i} \end{pmatrix}, \quad (22)$$

where S_1 and S_2 depend on the scattering angle θ:

$$S_1 = \sum_n \frac{2n+1}{n(n+1)} (a_n \pi_n + b_n \tau_n), \quad (23)$$

$$S_2 = \sum_n \frac{2n+1}{n(n+1)} (a_n \tau_n + b_n \pi_n) \quad (24)$$

$E_{/\!/}$ and $E_\perp$ are parallel and perpendicular (to the scattering plane) components of the incident electric field, which lies on the xy plane; respectively; k is a wavenumber, r is a radius of the sphere, z is a distance from origin to plane, and τ_n nad π_n are functions determining the angle dependence of scattered fields.

The equations, described in this section, are useful for integral description of influence of the optical characteristics of the scatterers and the media in which these scatterers are situated. Prior to analyse the Mie coefficients a_n, b_n, c_n, and d_n, which serve for determination of the optical properties of the scatterers and the media, we will first introduce the optical scattering and absorption parameters, commonly used in biomedical optics and necessary for our modelling.

3.4 Optical Scattering and Absorption Parameters of Biological Tissues

Studying the tissue optical parameters is necessary for both, forward and inverse problems of predicting the diffuse light distributions. The optical properties of biological tissues can be described by the refractive indices of the various compounds of the medium, absorption and scattering coefficients, and a scattering phase function. Scattering of light occurs in media that contains variations in the refractive index at a level of a discrete particle or a continuous constituent. Biological tissues are heterogeneous media with refractive indices higher than of the air, which leads to a partial reflection of the incident light at the border of these two media. Reflection is the process by which an incident electromagnetic irradiation is partially or totally returned by the interface of two media with different refractive indices, such as cytoplasm and nucleus, for instance. The surface reflectivity can be defined as the ratio between reflected and incident wave amplitudes of the electric field. The ratio of the intensities of the waves determines the reflection coefficient, thus it is equal to square of the reflectivity. Both, the reflectivity and the reflection coefficient depend on the angle of incidence and refractive indices of the medium.

Non-reflected light from the surface passes into the medium, where it changes its velocity and direction due to the difference in the refractive indices of the tissue structural elements. The mathematical equation describing the refraction process is known as the Snell's law:

$$\frac{\sin\theta}{\sin\theta''} = \frac{\upsilon}{\upsilon'}, \tag{25}$$

where θ - is the angle of the incident light, θ''- is the angle of refraction, υ and υ'- are velocities of the light before and after entering the refracting medium, respectively. The corresponding refractive indices are defined as:

$$n = \frac{c}{\upsilon},$$
$$n' = \frac{c}{\upsilon'} \tag{26}$$

For mathematical estimations, the relative refractive indices *m*, (the ratio between the light velocities in one medium and in another one) are usually used. The typical refractive index of the tissue components lies in the range 1.35-1.47 [19].

A light wave, have penetrated into a biological tissue, attenuates due to the multiple scattering and absorption. The elastically connected charged particles under the influence of the electromagnetic waves are driven by the electric field. The resonance occurs when the wave frequency is equal to the intrinsic frequency of oscillations of the particles, which is accompanied by absorption. In a purely absorbing (non-scattering) medium the intensity attenuation due to absorption is described by the Beer-Lambert law:

$$\frac{I_{med}}{I_0} = \exp(-\mu_a d) \quad (27)$$

where I_0 – is the intensity of the incident light, I_{med} – is the light intensity after travelling a distance d inside the medium, and μ_a [cm^{-1}] is the absorption coefficient of the medium.

The ability of particles to scatter light is connected to the scattering cross-section, integrated over 4π angle – the scattering cross-sectional area. The scattering coefficient μ_s [cm^{-1}] is the sum of the products of the scattering cross-sections σ by number of scattering particles in the volume:

$$\mu_s = \sum_i \rho_i \sigma_{si} \quad (28)$$

Absorption coefficient of a biological tissue provides information on the concentration of various chromophores [20], while the scattering properties provide information on the form, size, and concentration of the scattering components of the medium [21].

The inverse of the absorption or scattering coefficients determines the average distance that a photon travels prior to the absorption or scattering event. Due to their opacity, in most of the biological tissues, both, scattering and absorption processes, occur during the light propagation. The first optical parameter combining these two effects is the total effective attenuation coefficient which can be expressed as:

$$\mu_t = \mu_a + \mu_s, \quad (29)$$

Another optical parameter, describing the tissue properties and connecting both, absorption and scattering coefficients, - is the albedo a (dimensionless):

$$a = \frac{\mu_s}{\mu_t} = \frac{\mu_s}{\mu_a + \mu_s}, \quad (30)$$

The total mean free path of the incident wave in a turbid media is defined as

$$l_{ph} = \frac{1}{\mu_t} = \frac{1}{\mu_a + \mu_s}, \quad (31)$$

Thus, the optical depth d of the light propagation into the tissue is determined by the following expression (for the case of a uniform attenuation):

$$d_{opt} = \mu_t l_{ph} \quad (32)$$

where l_{ph} - is the optical path length of the turbid medium.

In the scattering process, a photon, propagating in direction s_1 is scattered by a particle into direction s_2. The phase function p describes the portion of the light, scattered from the initial direction in the new direction, thus, the integral of the phase function, distributed in all directions, is equal to 1:

$$\int_{4\pi} p(s_1, s_2) d\omega' = 1 \quad (33)$$

where $d\omega$'- is the differential solid angle in the direction s_2.

Usually the new possible directions s' do not occur with equal probability, and depend on the type of particle causing the scattering, and the possible structure of the scattering medium. The phase function is commonly characterized by the scattering anisotropy factor g:

$$g = \int_{4\pi} p(s_1, s_2)(s_1 s_2) d\omega' \quad (34)$$

If the scattering is symmetric with respect to the direction of the incident wave, then the phase function depends only on the angle θ between the directions of s_1 and s_2, i.e. $g = \langle \cos(\theta) \rangle$ describes the average cosine of a scattering angle.

The scattering phase functions of biological scatterers are often rather complicated. For the media, where the asymmetry parameter g is known, it is not always necessary to use a complete description of the phase function $p(\cos\theta)$, as there are several approximations among which the most widely used in tissue optics is the Heyney-Greenstein approximation.

The values of the anisotropy factor g lie in the range from -1 for backward scattering to 1 for forward scattering, with 0 for isotropic scattering. As the phase function is influenced by the microscopic characteristics of scattering structures, such as size and shape, most of biological tissues have a high total g-factor value of 0.8-0.9 [22].

Some of the optical parameters serve as inputs for Mie calculations for our models, the others (the outputs of Mie calculations) - as inputs for Monte Carlo modelling. Next sections of this chapter describe the algorithm of electromagnetic-wave theory-based calculations for our the first layers of our models.

3.5 Mie Calculations of Optical Parameters of Bladder Tissues and Phantoms

3.5.1 Mie Scattering by Spherical Particles

This section presents the algorithm of Mie calculations for modelling of the light distribution in media with diffusing particles of different sizes in the top layers. Such calculations are necessary for further Monte Carlo modelling of the surface DR light distribution aiming the comparison of modelled and experimental results of the sensitivity tests. The experimental part of these tests is presented in the Section 2.2.

3.5.1.1 Modelling of Light Propagation into a Three-Layered Medium with Diffusing Particles

By means of the scattering and absorption, the laser electromagnetic waves interact with inner structural elements inside a biological turbid medium. Physically such process is the changes of the electromagnetic fields generated inside the tissue. Generally speaking, the "prediction" of behaviour of the electromagnetic waves in the tissue is hampered to the solution of the Maxwell's equations for the macroscopic electromagnetic field at the interior points in matter.

Due to the non-zero refractive index of the medium, the wavelength, penetrating inside, changes its value: $\lambda_{med} = \frac{\lambda_{vac}}{n_{med}}$. Furthermore, in order to compute the scattering amplitudes, on which the scattering cross-section and anisotropy factor are based, it is necessary to introduce the scattering parameters: Mie coefficients a_n and b_n. The Mie coefficients depend on the relative refractive index $m = \frac{n_{sph}}{n_{med}}$, and on the size parameter $x = ka$, where $k = \frac{2\pi}{\lambda_{med}}$ - is a wave number, and a - is a radius of the sphere:

$$a_n = \frac{m^2 j_n(mx)[x j_n(x)]' - j_n(x)[mx j_n(mx)]'}{m^2 j_n(mx)\left[x h_n^{(1)}(x)\right]' - h_n^{(1)}(x)[mx j_n(mx)]'}$$

$$b_n = \frac{j_n(mx)[x j_n(x)]' - j_n(x)[mx j_n(mx)]'}{j_n(mx)\left[x h_n^{(1)}(x)\right]' - h_n^{(1)}(x)[mx j_n(mx)]'} \quad (35)$$

where $j_n(z)$ and $h_n^{(1)}(z)$ are spherical Bessel functions. Thereby the scattering cross-sectional area, related to the scattering efficiency by the geometrical area $w = \pi a^2$ as

$$Q_{sca} = \frac{\sigma_{sca}}{w}, \quad (36)$$

can be defined by:

$$\sigma_{sca} = \frac{2\pi}{k^2}\sum_{n=1}^{n_{max}}[(2n+1)[|a_n|^2 + |b_n|^2]], \quad (37)$$

where the maximum number of iterations for biological scatterers was proposed by Bohren and Huffman in 1983 [6] to be $n_{max} = x + 4x^{1/3} + 2$. The asymmetry parameter of the scattering is described by the ratio of

$$Q_{sca}\langle cos\rangle = \frac{4}{x^2}\left[\sum_n\left[\frac{n(n+2)}{n+1} Re\{a_n a_{n+1}^* + b_n b_{n+1}^*\}\right] + \sum_n \frac{2n+1}{n(n+1)} Re\{a_n b_n^*\}\right] \quad (38)$$

and Q_{sca}.

An algorithm of such calculations was developed for a Mathcad program. This algorithm is similar to the algorithm made by Matzler [23] for the MATLAB program.

3.5.1.2 Calculation Results: Input Parameters for Monte-Carlo Modelling

The MC modelling requires a set of input parameters for each phantoms layer, including refractive index *n*, scattering coefficient μ_s, absorption coefficient μ_a, anisotropy factor *g*, and

layer thickness *l*. Several of those parameters (like g and μ_s) can be obtained by the Mie calculations, the others have to be known prior to the MC modelling. This section presents the calculations of the optical parameters of our multi-layered media.

To estimate the contribution of the directly-reflected light to the overall light distribution at the surface of our bladder models we have calculated the refractive indices *n* for all the layers of our phantoms, using the law of Gladstone and Dale [24]:

$$n = n_1 c_1 + n_2 c_2, \tag{39}$$

where n_1, n_2 and c_1, c_2 are the refractive indices and volume fractions of the basic substance (gelatin matrix and water) and the scattering particles, respectively, and $c_1 + c_2 = 1$. Such reflection together with a part of the DR light, is concentrated in the central part of the light signal, at the entrance of the incident beam, forming the area *I* in Fig.2.1.

The refractive index of the polystyrene particles used in our experimental phantoms is n_p=1.59 [25]. The substance of the top layers, surrounding the scattering particles, consisted of gelatin matrix (5%) with n_{gel}=1.533, and of water, with

$$n_{wat} = 1.31848 + \frac{6.662}{\lambda[nm] - 129.2} \qquad [26] \tag{40}$$

Thus, the refractive index of the surrounding medium for the scattering particles of the first layers was

$$n_{1med} = 0.05 n_{gel} + 0.95 n_{wat} \tag{41}$$

The total refractive indices of the first layers of the phantoms with the particles of 0.05 μm and 0.53 μm diameters were equal to the index of the surrounding medium, as the impact of the spheres on the refractive indices can be neglected due to the low volume fractions, which were 6.5×10^{-10} and 7.8×10^{-7}, respectively. The refractive index of the first layers of the phantoms with the spheres of 5.09 μm diameter was:

$$n_{1\_5.09} = 6.9 * 10^{-4} n_{sph} + 0.9993 n_{1med} \tag{42}$$

The indices of refraction of the second and the third layers of our phantoms were calculated in consideration of the refractive index of Intralipid 20% ($n_{\text{int}20\%}$=1.361 at 532 nm wavelength [27]):

$$n_{2med} = 0.016 n_{int100\%} + 0.05 n_{gel} + 0.934 n_{wat} \tag{43}$$

and

$$n_{3med} = 0.02 n_{int100\%} + 0.05 n_{gel} + 0.93 n_{wat} \tag{44}$$

From the formula of the Fresnel reflection of the light entering the medium, which is defined as [28]:

$$R = (\frac{1-n}{1+n})^2 \quad (45)$$

the Fresnel reflections for our mediums with different scattering particles were found: $R_{0.05} = 0.0216\ (2.2\%), R_{0.53} = 0.0216\ (2.2\%), \text{and } R_{5.09} = 0.0217\ (2.2\%)$

Due to the low values, the absorption coefficient for a water suspension of the non-absorbing polystyrene spheres [29] and the scattering coefficient of gelatin can be neglected [26] in our studies. As no additional absorbers were used in the phantoms, we considered gelatin to be the main absorber in each layer of the media with μ_a = 0.001 cm^{-1} [30]. The anisotropy factors of the two bottom layers were calculated by the formula given for the Intralipid in [23]:

$$g_{int} = 1.1 - 5.8 * 10^{-4}\lambda \quad (46)$$

The scattering coefficients for different Intralipid volume fractions were taken from [26].

Using the Mie and Rayleigh theories [6] the scattering coefficients and the anisotropy factors were calculated in a Mathcad program for the top layers with the spheres of 5.09 μm, 0.53 μm and 0.05 μm diameters (see Table 3).

Name/ Parameter	refractive index, n	anisotropy factor, g	scattering coefficient, μ_s, [cm-1]	absorption coefficient, μ_a, [cm-1]
First layer with the spheres of 0.05 μm	1.3449	0.027	0.000015	0.001
First layer with the spheres of 0.53 μm	1.3449	0.867	0.024	0.001
First layer with the spheres of 5.09 μm	1.34505	0.87	3.9	0.001
Second layer	1.347	0.79	10	0.001
Third layer	1.34752	0.79	15	0.001

Table 3 *Input parameter values for Monte Carlo modelling.*

The anisotropy factors of the particles of 0.53 μm and 5.09 μm in a concentration of 10^7 are very similar (see Table 3), and their high values move the photons strongly into the medium, and make them hit faster next scatterers. The scattering coefficients of the largest particles are about 160 times higher than those of the medium size, and much more higher than those of the smallest, which reduces the mean free path between the two scattering events in the media with the particles of 5.09 μm diameter. Such particular differences in the scattering properties of the media can potentially lead to the differences in DR signals from the phantoms with different sizes of scattering particles.

3.5.2 Scattering by Nucleated Cells Modelled as "Coated" Spheres

In order to simulate the DR signals five states of the UB epithelium (see Section 2.3) by a Monte Carlo method, we have to determine the input parameters for such modelling. This section describes the algorithm for Mie calculations of optical parameters for different states of the bladder wall. Unlike the previous Mie calculations for the models with the optical parameters of our phantoms, the calculations in this section were performed basing on the parameters of real bladder tissue.

3.5.2.1 Scattering Amplitudes

The nuclear sizes of the bladder transitional epithelium are of about 5 μm for the normal cells, and 10 μm for the enlarged, which is larger than the wavelengths of the visible range 400-750 nm. Such nuclear sizes together with their orbicular shape, give us a subject to consider the nuclei as large spherical scattering centres inside the cells having different refractive indices. Thus, Mie calculations for "coated spheres" were chosen as a basis for determination of the input parameter values required for Monte Carlo simulations of the light distribution in the first layers of our models.

We consider an electro-magnetic wave incident to the "coated sphere" with an inner radius equal to the mean radius of a nucleus, and the outer - of a cell. In order to compute the scattering amplitudes, on which the scattering cross-section and anisotropy factor are based, it is necessary to express the scattering parameters: Mie coefficients a_n and b_n (cf. equation 35). They depend on the relative refractive indices $m_1 = \frac{n_{sph}}{n_{coat}}$ and $m_2 = \frac{n_{coat}}{n_{med}}$, and on the size parameters $x_1 = ka_1$ and $x_2 = ka_2$, where the wave number $k = \frac{2\pi}{\lambda_{med}}$, and a_1 and a_2 are respectively sphere's and cell's radii:

$$a_n = \frac{j_n(x_2)[[z_3 j_n(z_3)]' + A_n[z_3 y_n(z_3)]'] - m_2^2[x_2 j_n(x_2)]'[j_n(z_3) + A_n y_n(z_3)]}{h_n^{(1)}(x_2)[[z_3 j_n(z_3)]' + A_n[z_3 y_n(z_3)]'] - m_2^2\left[x_2 h_n^{(1)}(x_2)\right]'[j_n(z_3) + A_n y_n(z_3)]}$$

$$b_n = \frac{j_n(x_2)[[z_3 j_n(z_3)]' + B_n[z_3 y_n(z_3)]'] - [x_2 j_n(x_2)]'[j_n(z_3) + B_n y_n(z_3)]}{h_n^{(1)}(x_2)[[z_3 j_n(z_3)]' + B_n[z_3 y_n(z_3)]'] - \left[x_2 h_n^{(1)}(x_2)\right]'[j_n(z_3) + B_n y_n(z_3)]} \quad (47)$$

with

$$A_n = \frac{m_2^2 j_n(z_2)[z_1 j_n(z_1)]' - m_1^2 j_n(z_1)[z_2 j_n(z_2)]'}{-m_2^2 y_n(z_2)[z_1 j_n(z_1)]' + m_1^2 j_n(z_1)[z_2 y_n(z_2)]'}$$

$$B_n = \frac{j_n(z_1)[z_2 j_n(z_2)]' - j_n(z_2)[z_1 j_n(z_1)]'}{-j_n(z_1)[z_2 y_n(z_2)]' + y_n\ -(z_2)[z_1 j_n(z_1)]'} \quad (48)$$

and $z_1 = m_1 x_1$, $z_2 = m_2 x_1$, $z_3 = m_2 x_2$;

where $j_n(u)$, $y_n(u)$ and $h_n^{(1)}(u)$ are spherical Bessel functions of the first, second and third kind, respectively.

The scattering efficiency Q_{sca} for our scatterers can be defined by:

$$Q_{sca} = \frac{2}{a^2}\sum_{n=1}^{n_{max}}[(2n+1)[|a_n|^2 + |b_n|^2]] \quad (49)$$

where the maximum number of iterations for the case of biological scatterers is $n_{max} = x_2 + 4{x_2}^{1/3} + 2$. The asymmetry parameter of the scattering can be obtained from the ratio between $Q_{sca}\langle cos\rangle$ and Q_{sca} with

$$Q_{sca}\langle cos\rangle = \frac{4}{x^2}[\sum_n[\frac{n(n+2)}{n+1} Re\{a_n a_{n+1}^* + b_n b_{n+1}^*\}] + \sum_n \frac{2n+1}{n(n+1)} Re\{a_n b_n^*\}] \quad (50)$$

and n ∈ [1, n_{max}].

3.5.2.2 Definition of Input Optical Parameter for Mie Calculations

In order to reproduce the optical properties of the UB wall, several three-layered models, mimicking mucosa, submucosa and muscle layer, were considered. To trace the influence of each intra- or extra-cellular modifications, five "states" of the UB urothelium, corresponding to main metamorphosis at dysplasia, were imitated (by varying the scatterer's parameters in the first layers of the models):

Type I. Normal, with normal size and concentration of the cell nuclei;

Type II. Enlarged nuclei;

Type III. Absorption growth;

Type IV. Nuclear population density increase;

Type V. All changes together.

As the pre-cancerous changes arise mostly in the epithelium, and the lower layers do not undergo discriminant modifications in their structure, same optical properties for the second and third layers were reproduced in all types of the models. Implementation of such modelling by Monte Carlo simulation method requires the prior knowledge of the optical parameters of each layer and type of the model. Some parameters of the bladder wall are presented in the studies of Cheong *et al.* (1987) [31], Star *et al.* (1987) [32], Splinter *et al.* (1989) [33].

First (top) layers: The top layer of the UB wall mostly consists of the epithelial cells (about 15 μm in diameter) with rounded nuclei inside, which we consider to be the main scattering centers of the first layer of our models. As the epithelial layer is a tight pack of cells, the surrounding medium for these scattering centers is intracellular medium with its refractive index n_{cell} lying between 1.35 and 1.38 [13]. In the present work we used a value of the cell refractive index n_{cell}=1.37 for Mie calculations as an input parameter, and for the Monte Carlo simulations as a refractive index of the first layers (Table 4). Beauvoit *et al.* (1994) [34] assumed a nucleus refractive index relative to the cell cytoplasm to be about 1.04, thus we considered the nucleus refractive index to be equal to n_{nuc}=1.42. As the cells of the transitional epithelium are densely packed, we considered the refractive index of the surrounding medium for the cell (the extracellular matrix) in the first layers to be minimally different from the cellular one, thus to be lower than the refractive index of the cytoplasm because of the presence of extracellular composition between the cells, so that n_{med}=1.365.

Based on the study of Staveren *et al*. (1994) [35], in which the value of the absorption coefficient μ_a for mucosal/submucosal layers lies in the range of 0.6-1 [cm^{-1}] for the green wavelength region, we considered the absorption of the first layers to be equal to the maximum value 1 [cm^{-1}], as the absorption in the top epithelial layers is usually higher than in the second submucosal layers. The calculations of the values of the scattering coefficients μ_s were based on the Mie theory, described above.

Second (intermediate) layers: The submucosal layer (which is 400-1000 μm thick) has a small amount of cells, and consists generally of the intercellular material with protein fibers, forming a connective tissue, which main constituent is water, forming of about 60% [36]. For that reason, we have taken a value of n_{exf}=1.36 [37] for the extracellular fluid as the refractive index for the intermediate submucosa-like layers. The absorption coefficient and anisotropy factor of the second layers were chosen as minimum values given in [35] for 500-550 nm wavelengths, 0.6 [cm^{-1}] and 0.87, respectively. The results obtained by Qu et al. (1994) [38] for the bronchial tissues show that the scattering coefficient of the submucosal layer is about 40 less than of the one of mucosal layer, which we took into account for the determination of the scattering parameter of the second layer.

Third (bottom) layers: The muscle layer of the UB mostly consists of smooth muscle fibres, connective tissue and nerves, and is about 2 mm thick. The refractive index value for this layers muscle layers n_3=1.37 was taken from [39], and the other optical parameters were based on data from the colon muscle tissues [40], similar by its structure to the bladder muscle tissue: 193 cm^{-1}, 1.53 cm^{-1},and 0.941 for the scattering, absorption and anisotropy coefficients, respectively.

The thicknesses of each layer in each simulation model were fixed to 200 μm for the first, 700 μm for the second, and 2.1 mm for the third layers.

In the present study, the imaginary part of the refractive indices was chosen in a way that the final calculated absorption coefficient matched with the value μ_a=1 presented in the section 2.1, and with the corresponding absorption changes according to the cases III-V of the neoplasm formation. The results of Staveren *et al.* [35] and Wei *et al.* [40] show that the absorption of diseased bladder and colon tissues exceeds the normal one by a factor of about 1.5 to 3. Consequently, in the III^d type of our models, we increased the absorption coefficient from 1 cm^{-1} (for normal tissue, type I) to 2.5 cm^{-1}. In the type IV we considered that the scatterers in the epithelium have multiplied so that the population density has changed from

1.5×10^8 to 3×10^8 cells per ml, and the absorption at the first layer has grown. The average density of scatterers ρ defined for the first layers of the models from the histological studies.

Taking into account that in case of population density augmentation the nuclei multiplies inside the cells, the computations for the type IV consisted of two parts: 1) the scattering coefficients of the normal tissue (type I), calculated for the "coated" spheres (nuclei in cells) were summed up with 2) those ones, computed for the nuclei as separate spherical scatterers without the "coat", which was already taken into account in the first part. The equations for such computation can be found by considering the refractive index of the "coat" to be equal to the surrounding medium. Although our calculations allowed to obtain the values of the anisotropy factor *g*, they did not reflect the contribution of all the compounds of the tissue (including small cellular and intracellular components). For our models average values for the anisotropy parameter of the epithelial tissue [35], [38], [40] were used.

The Mie calculations for "coated" spheres were computed in a MathCAD program by an algorithm, presented in Appendix of this thesis.

Model type/Parameter	**a, μm**	**μ_a, cm^{-1}**	**ρ, nuclei per μm^3**	**n_{nuc}**
I. Normal	5	1	0.00015	1.42+0.000413i
II. Nuclei size growth	10	1	0.00015	1.42+0.000051i
III. Absorption changes	5	2.5	0.00015	1.42+0.00101i
IV. Population density changes	5	2	0.0003	1.42+0.000413i
V. All changes together	10	5	0.0003	1.42+0.000121i

Table 4 *Input parameters applied for Mie calculations performed on each of the 5 types of bladder epithelial tissue-like models.*

3.5.2.3 Output Scattering and Absorption Parameters from Mie Calculations

The input parameters for the Monte Carlo modelling of the laser light interaction with our models, mimicking five states of the bladder epithelium are summurized in the Table 5.

Modelling Parameters	Layer 1 (transitional epithelium), 200 µm	Layer 2 (submucosa), 700 µm	Layer 3 (muscle), 2100 µm
Type I. Normal			
g	0.91	0.87	0.941
μ_s, cm^{-1}	190*	150	193
μ_a, cm^{-1}	1	0.6	1.53
n	1.37	1.36	1.37
Type II. Nuclei size growth			
g	0.91	0.87	0.941
μ_s, cm^{-1}	**262***	150	193
μ_a, cm^{-1}	1	0.6	1.53
n	1.37	1.36	1.37
Type III. Absorption changes			
g	0.91	0.87	0.941
μ_s, cm^{-1}	**187***	150	193
μ_a, cm^{-1}	**2.5**	0.6	1.53
n	1.37	1.36	1.37
Type IV. Population density changes			
g	0.91	0.87	0.941
μ_s, cm^{-1}	**272***	150	193
μ_a, cm^{-1}	**2**	0.6	1.53
n	1.37	1.36	1.37
Type V. All changes together			
g	0.91	0.87	0.941
μ_s, cm^{-1}	**513***	150	193
μ_a, cm^{-1}	**5**	0.6	1.53
n	1.37	1.36	1.37

Table 5 *Input parameters for Monte Carlo modelling of light distribution in the bladder wall. The calculations of the parameters marked with * are based on the Mie theory.*

3.6 Conclusion

By varying sizes and concentrations of the epithelial scatterers, and epithelial absorption properties, different states of the bladder were mimicked. With the use of the calculation algorithms for spherical and “coated” spherical scatterers, presented in this Chapter, the values of the optical parameters needed for the further Monte Carlo modelling were obtained.

References:

[1] Perelman L. T., V. Backman, M. Wallace, G. Zonios,1 R. Manoharan, A. Nusrat, S. Shields, M. Seiler, C. Lima, T. Hamano, I. Itzkan,1 J. Van Dam, J. M. Crawford, and M. S. Feld, Observation of Periodic Fine Structure in Reflectance from Biological Tissue: A New Technique for Measuring Nuclear Size Distribution, Vol. 80, No 3 Phys. Rev. Lett. 19, pp. 627-630, 1998.

[2] Marieb E. N., K. Hoehn. Human Anatomy and Physiology (3rd ed.). Benjamin Cummings, 2007.

[3] Backman V., Gurjar R., Badizadegan K., Itzkan I., Dasari R. R., Perelman L. T. and Feld M. S "Polarized light scattering spectroscopy for quantitative measurement of epithelial structures in situ," IEEE J. Sel. Topics Quant. Elec. 5(4), pp. 1019-1026, 1999.

[4] Beuthan J., Minet O., Helfmann J., Herrig M., Muller G., "The spatial variation of the refractive index in biological cells," Phys Med Biol 41(3), pp. 369-382, 1996.

[5] Wilson J. D., Bigelow C. E., Calkins D. J., and Foster T. H., Light Scattering from Intact Cells Reports Oxidative-Stress-Induced Mitochondrial Swelling, Biophysical Journal Volume 88, 2929–2938, 2005.

[6] Bohren C. F. and D.R.Huffman, Absorption and scattering of light by small particles, John Wiley & Sons, New York, 1983.

[7] Niemz M. H. , Laser-Tissue Interactions Fundamentals and Applications, 3d edition, Springer-Verlag Berlin Heidelberg, 2007.

[8] Kim A. D. and Joseph B. Keller, "Light propagation in biological tissue," J. Opt. Soc. Am. A 20, 92-98, 2003.

[9] Gu F., C.M. Crump and G. Thomas, Review: Trans-Golgi network sorting, CMLS, Cell. Mol. Life Sci. 58, 1067 – 1084, 2001.

[10] Rumyantsev P. P. (B. M. Carlson ed.), Soviet medcal reviews, supplement series, Crdiology Vol. 3, p. 30, Switzerland, 1991.

[11] Duran JM, Kinseth M, Bossard C, Rose DW, Polishchuk R, Wu CC, Yates J, Zimmerman T, Malhotra V, "The role of GRASP55 in Golgi fragmentation and entry of cells into mitosis". Mol. Biol. Cell 19(6): 2579–87, 2008.

[12] Dunn A. K., Modelling of Light Scattering from inhomogeneous biological cells, at Optics of biological particles, p. 20 (Hoekstra A., Maltsev V. and Videen G. eds.), Springer, The Netherlands 2007.

[13] Podgorsak E. B., Biological and Medical Physics, Biomedical Engineering: Radiation Physics for Medical Physicists, 2d ed., Springer, Berlin, 2010.

[14] Jost, “The morphology of normal humain bladder”, J. of Anatomy, 167, pp 103-115, 1989.

[15] Beauvoit B, Evans SM, Jenkins TW, Miller EE, Chance B, Correlation between the light scattering and the mitochondrial content, Analytical Biochemistry, 20; 226 (1): pp. 167-74, 1995.

[16] Green D. R. and Reed J. C., “Mitochondria and apoptosis”, Science 281, 1309-1312, 1998.

[17] Oudard S, Boitier E, Miccoli L, Rousset S, Dutrillaux B, Poupon MF., “Gliomas are driven by glycolysis: putative roles of hexokinase, oxidative phosphorylation and mitochondrial ultrastructure,” Anticancer Res. 17(3C), 1903-1911, 1997.

[18] Ishimaru A., Electromagnetic wave propagation, radiation, and scattering, (Prentice-Hall, Inc., New Jersey, 1991.

[19] Tuchin V. V., Optical clearing of tissues and blood, SPIE Washington, p. 3, 2006.

[20] Jacques S. L., Reflectance spectroscopy with optical fiber devices, and transcutaneous bilirubinometers, in biomedical optical instrumentation and laserassisted biotechnology, eds. A.M.Verga Scheggi, S.Martellucci, A.N.Chester and R.Pratesi, pp. 83-94, Kluwer Academic Publishers, Dordrecht, 1996.

[21] Mourant J. R., J.P.Freyer, A.H.Hielscher, A.A.Eick, D.Shen and T.M.Johnson, Mechanisms of light scattering from biological cells relevant to noninvasive optical-tissue diagnotics, Appl. Opt. 37, 3586-3593, 1998.

[22] Prahl S. A., "Light Transport in Tissue," PhD thesis, University of Texas at Austin, 1988.

[23] Matzler C., Research report No 2002-08, Institut für angewandte Physik, Universität Bern, pp. 1-24, 2002.

[24] Gladstone J., T. Dale, Researches of the refraction, dispersion and sensitiveness of liquids, Phil. Trans. Royal Soc. London 153, 1864.

[25] Bang Laboratories: TechNote 100 (Polymer Microspheres), 2010.

[26] Bashkatov A., E. Genina, V. Kochubey, V. Tuchin, Effects of scattering particles concentration on light propagation through turbid media Proceedings of SPIE 3917, 2000.

[27] Ding H., J. Lu, K. Jacobs, X-H Hu, Determination of refractive indices of porcine skin tissues and Intralipid at eight wavelengths between 325 and 1557 nm,: J. Opt. Soc. Am. A 22, 6, 2005.

[28] Hecht E., Optics, 4 ed., Addison Wesley, 2002.

[29] Quinten M., J. Stier, Absorption of scattered light in colloidal systems of aggregated particles, Colloid and Polym. Sci., 272, 1995.

[30] Kang H., J. Kim, Y. Yu, J. Oh, Molecular dynamics simulations of an angular velocimeter with a carbon nanotube oscillator, Journal of the Korean Physical Society 55, 1, 2009.

[31] Cheong W. F., M. Motamedi and A. J. Welch, Cheong Optical modeling of laser photocoagulation of bladder tissue Lasers Surg Medc 7, 72, 1987.

[32] Star W. M., J. P. A. Marijnissen, H. Jansen, M. Keijek and M. J. C. van Gemert, Light dosimetry for photodynamic therapy by whole bladder wall irradiation, Photobiol 46, 619-624, 1987.

[33] Splinter R., W. F. Cheong, M. J. C. van Gemert and A. J. Welch, In vitro optical properties of human and canine brain and urinary bladder tissues at 633 nm, Lasers and Surg Med 9, 37-41, 1989.

[34] Beauvoit B.., T. Kitai and B. Chance, Contribution of the mitochondrial compartment to the optical properties of the rat liver: a theoretical and practical approach, Biophysical J. 67, 2501-2510, 1994.

[35] Van Staveren H. J., J. F. Beeu, J. W. Ramaekers, M. Keijzerg and W. M. Star, Integrating sphere effect in whole bladder wall photodynamic therapy: I.532 nm versus 630 nm optical irradiation Phys. Med. Biol. 39, 947-959, 1994.

[36] Werner A. P. Luck, Water in biological systems, in Topics in Current Chemistry, Volume 64, 114-180, 1976.

[37] Perelman L. and V. Backman, Spectroscopy of light scattering by epithelial tissues: principles and applications, in: V. Tuchin (ed.), Optical Biomedical Diagnostics 2 (in Russian), Fizmalit, Moscow, 2007, pp. 36-76, 2007.

[38] Qu J., C. MacAulay, S. Lam and B. Palcic, Optical properties of normal and carcinomatous bronchial tissue, Appl. Opt. 33(31), 7397-7405, 1994.

[39] Muthu P., Study of Cross Bridge Kinetics in Hypertrophic Ventricular Muscle PhD thesis, University of North Texas (Fort Worth), 2009.

[40] Wei H.-J., D. Xing, J.-J. Lu, H.-M. Gu, G.-Y. Wu, Y. Jin, Determination of optical properties of normal and adenomatous human colon tissues in vitro using integrating sphere techniques, World J Gastroenterol, 11(16), 2413-2419, 2005.

4

CHAPTER

Monte Carlo Modelling of Light Propagation into Three-Layered Tissues and Tissue Phantoms

"Mathematics is the most reliable form of prophecy."

W. Schwebel

4.1 Introduction

In the previous Chapter we described a wave theory-based mathematical technique we used for calculating the values of the basic optical parameters of different phantoms and models mimicking bladder wall. The present Chapter describes a Monte Carlo-based (MC) technique, where the simulations of scattering and absorption happen with randomly travelling light photons. Based on the transport equation, Monte Carlo modelling methods can be used for describing light transport in tissues and to receive photons distributions on the surface of absorbing and scattering multi-layered media. This capability of the MC technique is one of the main reasons explaining our choice of the modelling method.

The problem of light transport through a biological tissue is a complex problem due to the large variety in distribution, shape and orientation of the scattering centres. For a model of light transport in biological tissues to be successful, it has to factor into the following peculiarities: multiple scattering and absorption in a complex tissue structure. Monte Carlo modelling techniques, based on the light transport in tissues, are commonly used in tissue optics in order to simulate the photon migration in a media for estimating the transmittance and back-scattering probability distributions [1], [2], [3] [4]. A detailed description of a Monte Carlo method describing the photon-tissue interactions with turbid multi-layered media was given by Wang and Jacques in 1995 [2]. The Monte Carlo modelling method of light transport in multi-layered tissues (MCML) reflects the possibilities of tracing photons behaviour inside the tissue. In the present study a method for obtaining the matrices of the back-scattered light distribution was used in order to simulate the light propagation into the tissues for differentiating between cancerous and normal tissues.

The Monte Carlo method is a method of statistical tests for tracing the light transport inside a medium, requiring several initial parameters, describing the optical properties of the medium. In the MC simulation, photon packages are traced through the tissue until the exit or termination due to absorption.

4.2 Light Transport Theory

In this Section the mathematical aspects of the light transport in biological tissues, necessary for our modelling, are discussed. Modelling of light propagation in turbid media can be expressed in integral-differential form by the radiative transport theory [5]. One of the main peculiarities of this theory is that it considers the energy transfer in a medium by superposition of energy flux, but not of the electromagnetic fields [6]. Photon propagation into a scattering and absorbing media is commonly used, has been previously described using the transport theory by numerous authors [7], [8], [9], [10]. Thus we present a brief description of the main parameters and features of the transport theory.

The flow of the photons, travelling in a turbid medium with the velocity *c* in a direction s_1, has a certain energy *hv*. The frequency, amplitude and phase of the flow randomly vary in time, changing the fluence rate. The power flux density in the direction s_1 within a solid angle $d\omega$ at a unit interval of frequencies near the frequency *v* is expressed by the radiance $J(r, s_1)$. The differential equation for radiance is the basic equation of the light transport theory, and is called radiative transport equation [11]:

$$\frac{dJ(r,s1)}{ds2} = -\mu_t J(r,s1) + \frac{\mu_s}{4\pi}\int_{4\pi} p(s1,s2)J(r,s2)\,d\omega \qquad (51)$$

where *r* reflects the position of the incident light, $p(s_1, s_2)$ is the scattering phase function determining the probability of scattering from a direction s_1 into s_2, and μ_s and μ_t are, respectively, scattering and attenuation coefficients of the medium.

The integral of the radiance over 4π describes the fluence rate $\Phi(r, s_1)$, distributed in all directions, which is more useful for biomedical optical applications, as well as the radiant flux $F(r, s_1)$, which describes the power incident on a sphere at a position r and transferred per unit area:

$$\Phi(\mathrm{r},\mathrm{s1}) = \int_{4\pi} L(r,s1)d\omega \qquad (52)$$

$$\mathrm{F}(\mathrm{r},\mathrm{s1}) = \int_{4\pi} L(r,s1)s1d\omega \qquad (53)$$

In order to simplify analytical solving of the transport equation, various numerical and approximation methods were developed. Monte Carlo stochastic method is one of such numerical approximations of the transport equation.

4.3 Monte Carlo Simulation Flowchart and Random Variables

This Section describes the main iterations of the algorithm of Monte Carlo modelling. The principle of Monte Carlo-based method for DR light modelling is to calculate the random processes of photon transport in media, where resulting matrices of light, transmitted or returned to the surface, obtained after a set of statistical data [12]. Depending on the aim, many physical parameters of the photon package, describing the properties of the medium, such as distribution of absorption and back-scattering, can be acquired. By repeating the tracking process for a large number of photon packages, it is possible to obtain statistics of needed characteristics. The number of photons or packages of photons to be launched depends on the need of accuracy.

General description of forward Monte Carlo simulation of the transport of light in a scattering and absorbing medium, is based on several main steps that are repeated until sufficient statistic accuracy is achieved: selection of a starting position for a photon or a packet, depending on the required spatial and angular distributions of the light; generation of a probable distance before the collision with the scatterer; statistical sampling and update of absorption; registration of photons. The flowchart of our Monte Carlo simulation, which was previously developed in the Biospectroscopy Laboratory of GPI RAS, is presented in the Fig. 4.1.

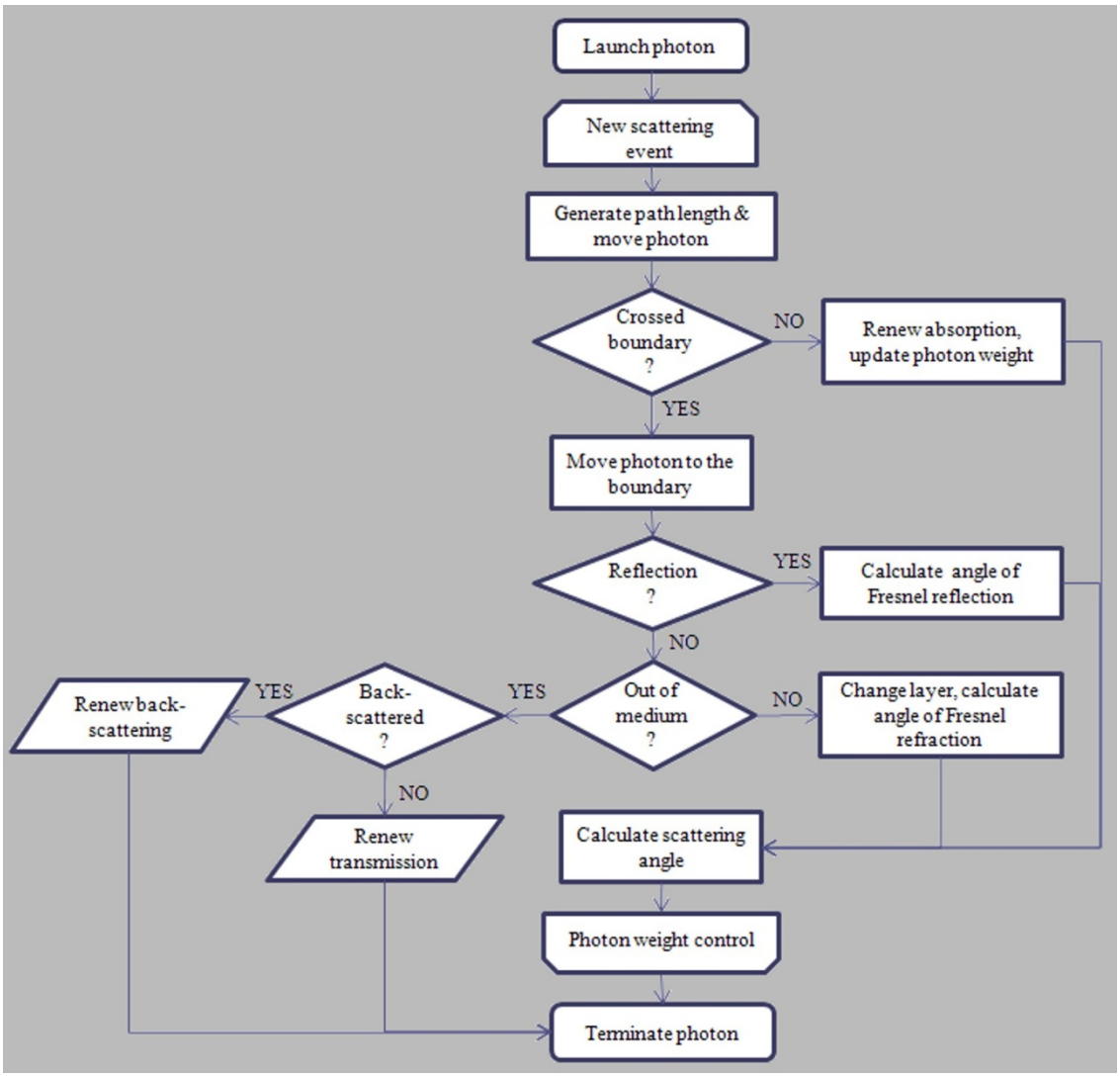

Figure 4.1 *Flowchart for Monte Carlo simulations of light distribution in a scattering and absorbing medium.*

In the MC simulations, the main factors influencing the behaviour of the photons are the mean free path of scattering and absorption events, and the scattering angle. Both are computed with the use of random variables. First random variable γ_1, distributed uniformly between 0 and 1, was used in our study for determining the photon path length l in the medium before the next absorption or/and scattering effect, called step size:

$$l = -\frac{1}{\mu_t} \ln(\gamma_1), \tag{54}$$

where $\mu_t = \mu_s + \mu_a$, with the distribution density $p(l) = \mu_t e^{-\mu_t l}$. The probability of photon absorption is described by $\beta = \frac{\mu_a}{\alpha}$, thus the updated weight W_i after an event of absorption is:

$$W_i = W_{i-1}(1-\beta) \quad (55)$$

where W_i- number the photons left in the packet.

As it was mentioned in the previous chapter, one of the most suitable approximations for the probability density function for mathematical modelling of the light distribution in biological tissues is a Heyney-Greenstein function - a simple one-parametric model, describing the scattering by single scattering approximation. The Heyney-Greenstein phase function $p(\theta)$ characterizes the scattering spatial distribution directions for a single scattering event, and is given by:

$$p(\theta) = \frac{1-g^2}{(1+g^2-2gcos(\theta))^{\frac{3}{2}}} \quad (56)$$

where θ is the scattering angle. The Heyney-Greenstein function was used for determination of the photon direction after a collision act as:

$$\cos(\theta) = \frac{1+g^2+[\frac{1-g^2}{1+2g\gamma_2-g}]^2}{2g} \quad (57)$$

for the case when g is variant from 0, and $cos(\theta) = 2\gamma_2-1$, for the case of $g = 0$, where γ_2- is a second random variable, also distributed uniformly between 0 and 1.

Behaviour of the photons at the interface boundaries of the layers is quite particular and should be taken into a special consideration. In general, scattering on the boundary surface of a layer is induced by the interface roughness, while the spatial scattering (inside the medium) is created by inhomogeneities inside the medium. After a collision act with the boundary between the layers of the UB tissue, the packet of the photons underwent the reflection in the case when the third random variable $\gamma 3$, uniformly distributed in the interval from 0 to 1, was less or equal to the probability of the Fresnel reflection. Otherwise, in our models, the photons continued to spread into the other layer in a direction according to the Snell's law for the angles of refraction, with the deviation caused by the interface irregularities. The deviation angle was calculated as an angle of scattering on the medium scattering element of the current layer. The photons, colliding with the layers' interfaces, deviate from the direction of the Fresnel angle due to the optical properties of a layer [13]. For example, in the case of our phantoms, it is to recall that the latter optical properties of each layer depend on the index of

refraction, population density and size of the polystyrene microspheres and liposomal components of the Intralipid. In order to accelerate the calculation, the photon diffusion in the medium, at a preliminary stage (after setting the parameters of the layers), the computations of the matrices of probabilities of transmitted and back-scattered light ,and of the angles of refraction for all the interfaces between the layers, were made in the directions from and to the light source in the range from 0° to 90° with discretization on the incidence angle equal to 1.

4.4 Simulation Results

4.4.1 Sensitivity Test of the Imaging Method of Surface Diffuse-Reflected Light Distribution

This Section presents the modelling of the light distributions on the surfaces of the phantoms (constructed for the sensitivity tests of the method), described in the Section 2.2. The input parameters for this modelling were described in the Section 3.5.1. For this case we simulated irradiation of a collimated light beam of 0.3 mm diameter with 10^7 of initialized photon packets with 10^7 photons in each. To correspond to the real experimental conditions a 378 ppi resolution was used. The final simulation matrix size was 60×60 pixels (0.4 cm in length). The simulation results were compared to the experimental results, obtained through the measurements performed on the phantoms. The matrices of the DR light on the tissue were processed in a MATLAB program in order to image the light distributions on the surfaces of the phantoms (Fig. 4.2). The raw intensity signals were normalised between 0 and 1 (according to the quantity of the back-scattered photons), corresponding, respectively, to the lowest and the highest determined quantities of the photons, hit the surface. For the 10^7 initially launched photons and 10^7 packets of photons, we considered the lowest photons quantity to be 10^8 photons (such a quantity corresponded to the value “0”), and the highest to be 3×10^{10} photons (such a quantity corresponded to the value “1”).

The obtained images of the simulated DR light distribution (Fig. 4.2) highlight the influence of the various sizes of polymer spheres on the light diffusion in biological models of the UB wall. The visualization of the surface DR light provided us with the differentiation

between the back-scattered light from the phantoms with diffusing particles of 50 nm, 0.53 μm and 5.09 μm diameters. The results show a similar character to the experimental ones: the highest intensities of the DR light were on the surfaces of the phantoms with the largest particles of 5.09 μm, while the lowest intensities were found on the surfaces of the phantoms with the smallest particles of 0.05 μm. Distinctive features in the areas of the DR light spots, back-scattered by the phantoms with microspheres of different sizes are seen.

The greater impact to the scattering process is made by the particles of the largest diameter of 5.09 μm, which is in a good agreement with cell nucleus sizes, which undergo the main initial cancerous transformations. The impact of the other scatterers to the DR signal can be used for estimating the background signal, that does not change during the cancerous transformations, and may be subtracted, or considered as a zero signal.

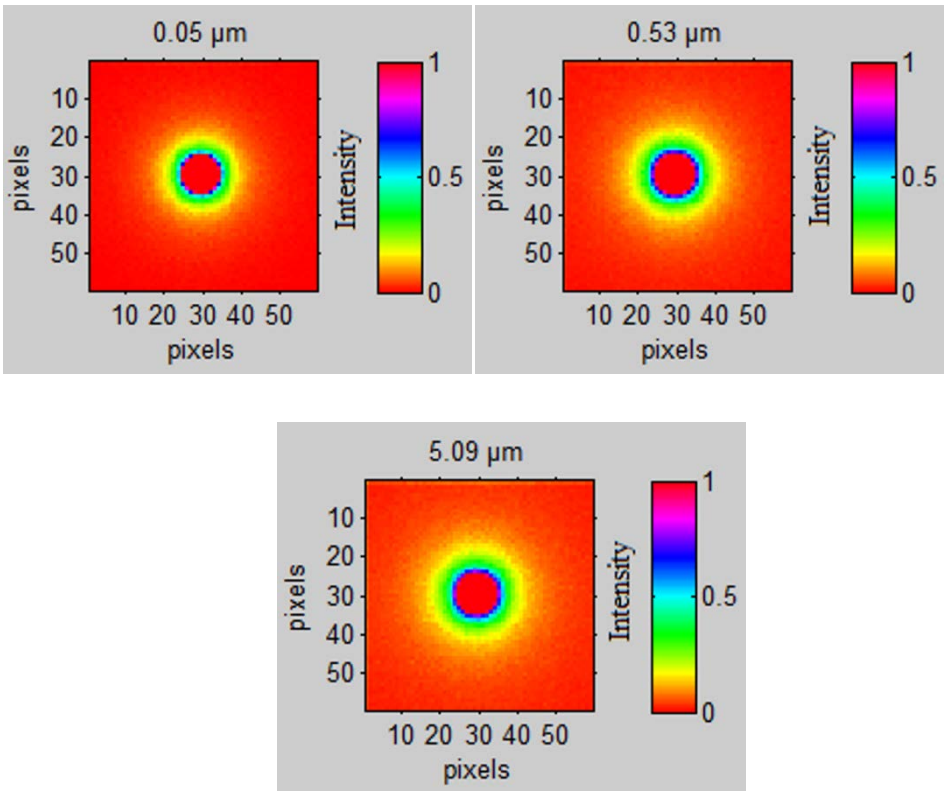

Figure 4.2 *Images from Monte Carlo simulations of Diffuse-Reflected light on the surfaces of the phantoms with the particles of diameters: (a) 50 nm, (b) 0.53 μm, (c) 5.09 μm. The images are plotted in a hue, saturation and intensity value colour space.*

4.4.2 Five States of Bladder Urothelium

This Section presents the modelling of the five states of the UB wall, based on the optical parameters described in the Section 3.5.2 of this thesis. The size of the imitated irradiation beam was 0.5 mm. The number of initialized photons was 10^7. The final matrix size was 30×30 pixels (0.2×0.2 cm). As a result of the simulations, the statistical matrices of the photons, returned back to the surface, were obtained.

The matrices of the DR light were processed in a MATLAB program in order to visualise the light distributions on the surfaces of our five models (Fig. 4.3). The raw signals were normalised according to the quantity of the back-scattered photons between 0 and 1, where 0 corresponded to 1 photon (the lowest determined quantity of the photons hit the surface), and 1 corresponded to $1.3x10^4$ photons (the highest determined quantity of the photons hit the surface). Such matrices are similar to the light distributions, which can be captured by the video camera from tissue surface.

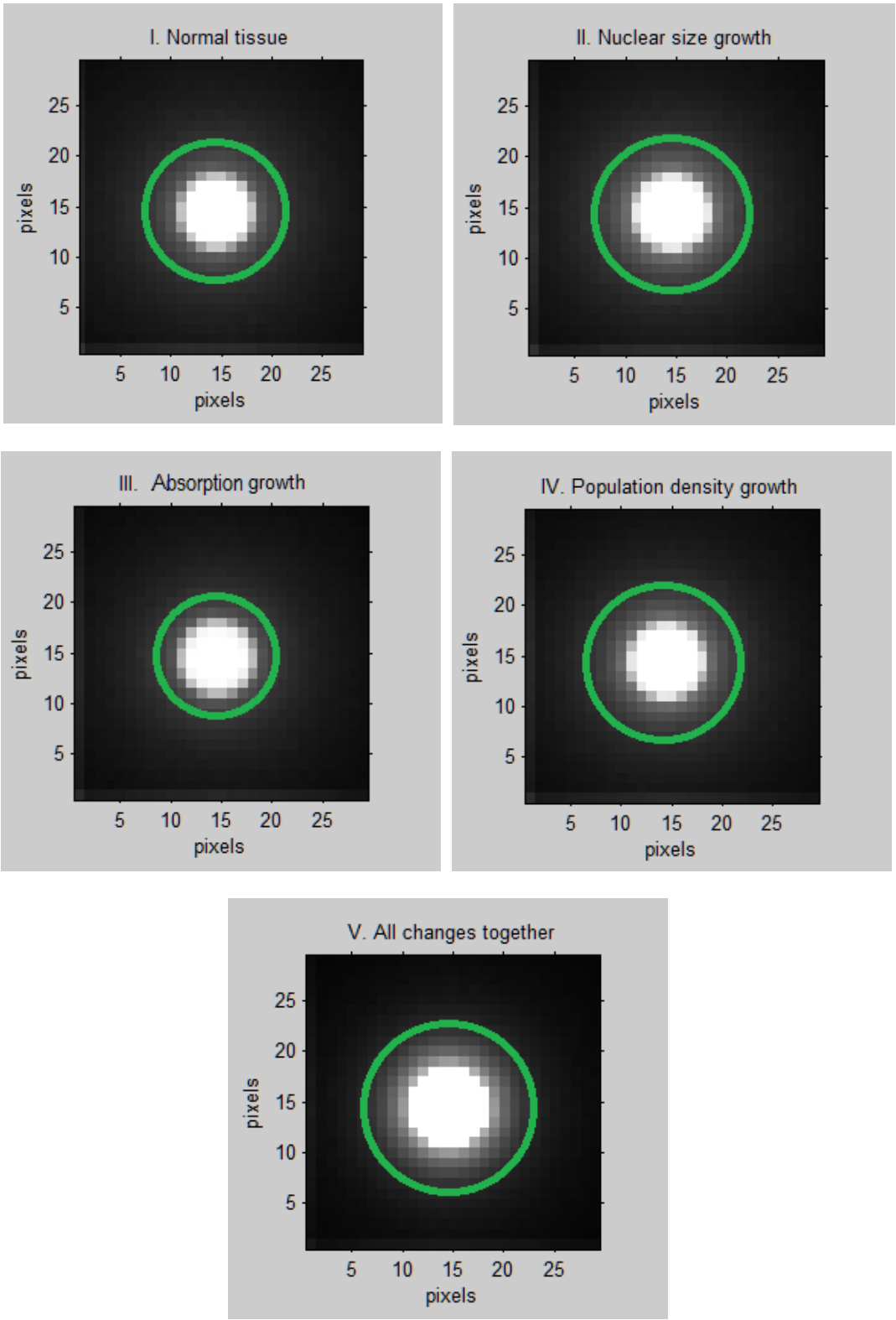

Figure 4.3 *Processed matrices of the Monte Carlo simulated surface back-scattered laser light: I - normal, with normal size of cell nuclei, II - enlarged nuclei, III – absorption growth, IV - population density augmentation, V - all changes together.*

Modelling results reflecting different changes of the DR light signals with scattering and absorption properties, show that the changes in absorption properties (models of type II) and all the changes together (models of type V) can be well-detected. Less obvious differences are seen in the cases of population density (models of type IV) and nuclear size growth changes (models of type II). The correlative analysis of the DR images with the optical parameters (see Section 3.5.2.3) shows that the surface spot increases with the scattering coefficient, and decreases with the absorption coefficient.

The areas of the DR images corresponding to the intensity values over the threshold of 0.3 (the green circle in the Fig. 4.3, found by varying the most distinguishing differences between the five models) were calculated for each model, and then normalized to the area of back-scattered signal from the normal tissue of type I. Figure 4.4 presents a comparison of the simulation and experimental data. The results show a positive correlation for all the five bladder tissue states. For some states the normalized values differ from each other due to the differences in the mathematical and experimental models (real bladder tissues and phantoms, respectively). Besides, due to the idealization of mathematical simulations, the normalized modelled area values are higher than the experimental for all the 5 states of the bladder tissue. This signifies more considerable differences between the bladder states for the case of mathematical modelling in comparison to the experimental detection.

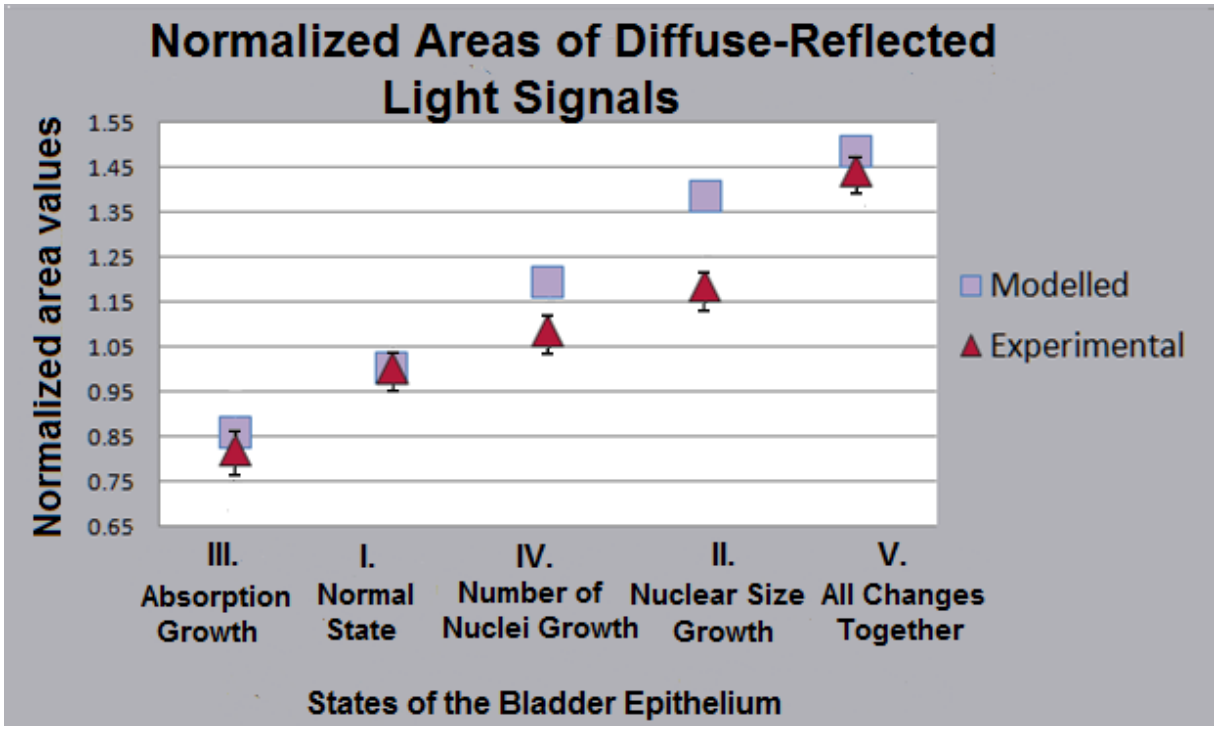

Figure 4.4 *Comparison of experimental and simulation Diffuse-Reflected light area ratios for 5 states of bladder tissue.*

The analysis of dependences of the back-scattering distributions on tissue optical properties allowed to reveal that the augmentation of the scattering coefficient leads to an increase in the size of the back-scattered laser spot on the surface of a model. Moreover, such increase can be compensated by the absorbing properties of the medium: the augmentation of the absorption coefficient reduces the surface spot size. The obtained results on all the five types of the models illustrate the back-scattering surface intensity distributions with the highest value for the type V of our phantoms (all changes together). However, in biological tissues, the higher increase in absorption or the diminution of scatterers (like mitochondria) in number or sizes with the neoplasm formation, can lead to decrease of the total back-scattered signals. Thereafter, any (up or down) deviations in the surface DR light signal indicate the presence of an abnormality in the tissue, and should be analysed according to each particular case. The possible issues of the presented modelling method can lead to the interpretation errors: due to the big variety of the scattering and absorption tissue optical parameters: scattering coefficient, anisotropy factor, absorption coefficient, refractive indices, and sizes and shapes of the scatterers, the results of the mathematical modelling can differ. However, the surface DR light signals, being normalized to a “normal” signal, depend only on the changes in the scatterers’ sizes and density, and absorber quantity. Thereafter, globally such variations do not influence on the eventual result, and are rather important for the calibration of the measurements.

4.5 Conclusion

The presented chapter was dedicated to the study of the forward problem for simulating surface scattering intensity matrices, i.e. the ability to trace the photons behaviour inside the tissue, and thus to analyse the variations of the optical scattering and absorption parameters. Such study gives an opportunity to analyse the differences occurring in the tissue on the cellular-intercellular level, without the use of any additional markers.

With the use of the optical parameters calculated by electromagnetic light theory, light behaviour inside the bladder tissue at five states was mimicked, varying sizes and concentrations of the scatterers and tissue absorbing properties. The matrices of the back-

scattered light from the three-layered phantoms and tissue models were calculated using Monte Carlo modelling. The analysis of the contribution of each epithelium property change to the scattering process showed that the most significant differences between the normal and early-pathological states of the UB were revealed due to the absorption growth, whereas the contribution of the population density to the backscattered light is insignificant. The flexibility of the method presented here allows varying the input parameters according to the tissue type, state and experimental or diagnostic conditions. The results of the experimental study are in a good agreement with the DR light signal modelling.

The presented analytical method is adapted to the urinary bladder diagnostics, taking into account its structure and internal disposition. However, this methodology can be rearranged for the diagnosis of other internal and external organs, basing on their structure and peculiarities of the tumour formation.

References:

[1] Doronin A., Meglinski I., Online object oriented Monte Carlo computational tool for the needs of biomedical optics, Biomed. Opt. Express, 2(9), pp. 2461-2469, 2011.

[2] Wang L., S. Jacques and L. Zheng, MCML - Monte Carlo modeling of photon transport in multi-layered tissues, Comp. Meth. in Biomed. 47, 131-146, 1995.

[3] Palmer C. M. and N. Ramanujam, Monte Carlo-based inverse model for calculating tissue optical properties. Part I: Theory and validation on synthetic phantoms, Appl. Opt. 45(5) 1062-1071, 2006.

[4] Matuszak Z., A. Sawow and M. Wasilewska-Rdwanska, Fluorescence spectra of some photosensitizers in solution and in tissue-like media. Experiment and Monte Carlo simulation Pol J Med Phys Eng, 10(4), 209-221, 2004.

[5] Case K. M. and P.F.Zweifel, Linear transport theory, (Addison-Wesley Publishing Co., Reading, MA, 1967.

[6] Welch A. J. and M.J.C.van Gemert, Optical-Thermal Response of Laser-Irradiated Tissue, Plenum Press, New York, 1995.

[7] Niemz M: Laser-Tissue Interactions. Fundamentals and Applications. 1st edition. Springer-Verlag Berlin Heidelberg; 1996.

[8] Tuchin VV: Handbook of Optical Biomedical Diagnostics: SPIE Society of Photo-Optical Instrumentation Engineering, 2002.

[9] Iizuka MN, Vitkin IA, Kolios MC, Sherar MD: The effects of dynamic optical properties during interstitial laser photocoagulation. Physics in Medicine & Biology, 45(5): 1 335-1357, 2000.

[10] Kim AD: Transport theory for light propagation in biological tissue. Journal of the Optical Society of America, 21:820-827, 2004.

[11] IshimaruA., Electromagnetic wave propagation, radiation, and scattering, (Prentice-Hall, Inc., New Jersey, 1991.

[12] Barlet S., Heilscher A., Monte Carlo simulations of the diffuse backscattered Mueller matrix for highly scattering media, Appl. Optics, V. 39, No 10, pp. 1580-1589, 2000.

[13] Amra C., From light scattering to the microstructure of thin-film multilayers, Applied Optics 32, 28, 1993.

5

CHAPTER

Clinical Studies and Mathematical Estimations of Multi-Wavelengths Light Excitation Mode

"The Hope always says, in future will be easier."

A. Tibul

5.1 Introduction

This Chapter of the thesis presents clinical studies of back-scattered laser signals on the surface of bladder tissues at different states. As it was revealed in the Section 2.4, the presence of the photosensitizer in the tissue does not influence the distribution of the back-scattered laser light, collected by a detector. Thereafter, the measurements of the back-scattered laser and fluorescent light can be held simultaneously. To realise such measurements, either a spectroscopic or a double-mode imaging systems can be used for detection both, laser and fluorescent signals. The imaging approaches of the DR light detection have a higher sensitivity due to the possibility to collect more of light photons at larger areas. The study of the present chapter does not require the measurements with higher sensitivity, and was held in a spectroscopic mode, allowing for obtaining fluorescence and laser signals simultaneously.

As it was previously discussed, the areas of surface DR signals change their size with the tissue optical properties. However, the differences in the DR signals from healthy and pathological tissues become less detectable when approaching the threshold level to the centre of the images, which makes the central signal of the DR light less informative. The absence of useful information in the central image areas allowed us to provide clinical analysis in a "contact" mode of a fiber probe with a tissue.

5.2 Diffuse-Reflected Light Detection on Tissue Surface

The clinical study of the back-scattered light distribution was performed in the urological department of Pirogov 1st Moscow Municipal Clinical Hospital. The analysis of the DR laser and fluorescence light was combined with the photodynamic therapy in one operation. The

measurements were made with the use of a Helium-Neon laser light source (632.8 nm, 30 mW) equipped with an SMA connector for optical fiber. The light, generated by the laser, was delivered to the tissue through the Y-shaped fiber-optic catheter illustrated in the Fig. 2.14 and 2.15. The distal end of the catheter had the diameter of 2 mm for insertion into the cystoscopic biopsy channel. The irradiation and light collection were performed throughout the optical fiber probe in contact with the tissue. The central fiber of the optical probe conducted the laser light radiation, while back-scattered fluorescent and laser light were collected by 6 receiving fibers surrounded the central fiber. At the output end of the catheter, which was connected to a spectrograph, the fibers were formed into a series in order to increase the luminous flux without resolution loss. At the entrance of the spectrograph a notch filter was installed for attenuating the intensity of the backscattered laser light about 10000 times and obtaining afluorescence detection level at the same scale.

For the fluorescence excitation, we have used a second-generation photosensitizer, a derivative of chlorine E6 - “Photolon” (Belorussia), with an absorption maximum peak in the red wavelength region. The “Photolon” dye drug was injected to the patient at a concentration of 1 mg per kg of body weight. The measurements of the back-scattered laser and fluorescent light distributions were carried out three hours after the drug injection in different parts of the bladder wall. Such time is optimal for studying the photosensitizer accumulation in the tissue, as its concentration reaches the maximum value in the tumour tissues in about 3 hours. In healthy tissues, “Photolon” accumulates minimally, that allows to avoid the need of additional tissue protection from the light exposure during the photodynamic treatment. After 24 hours the dye vanishes out from the tumour tissue. The resulting spectroscopic signals, collected by means of the setup described above, are curves with two main intensity peaks: one at the maximum peak of the backscattered laser signal at 632.8 nm, and the other at 706 nm, corresponding to the maximum peak of fluorescence signal. The analysis of the spectra was carried out by measuring the intensities of the fluorescent and back-scattered light signals at their peaks. The relative intensity values allowed to estimate the level of fluorescence, which made it possible to determine the relative drug accumulation in the tissues at three hours after the introduction of the photosensitizer.

5.3 Results and Discussion

Fig. 5.1 shows the values of the areas under the curves of fluorescent signals in the range 640-780 nm for 6 categories of bladder tissues: normal ones, large base (3 cm in diameter) of transitional cell carcinoma (main focus), two margin areas of the primary papillary tumours, and two shady areas of the bladder wall. The shady areas of the tissue, situated at some distance from the main focus of the tumour, were oedematous. The maximal accumulation of the photosensitizer was observed at the shady bladder tissue sections. The lowest intensity values corresponded to the base of the tumour, which can be explained by non-vascularisation of the neoplasm and its size, making the accumulation of the photosensitizer in tumour difficult. The intensity of the fluorescent signal from the first margin area of the tumour tissue was commensurate with the intensity from the normal tissue. The intensity of the fluorescence signal from the second margin area was overrated in comparison with the normal tissue, which indicated a greater accumulation of the photosensitizer in this area.

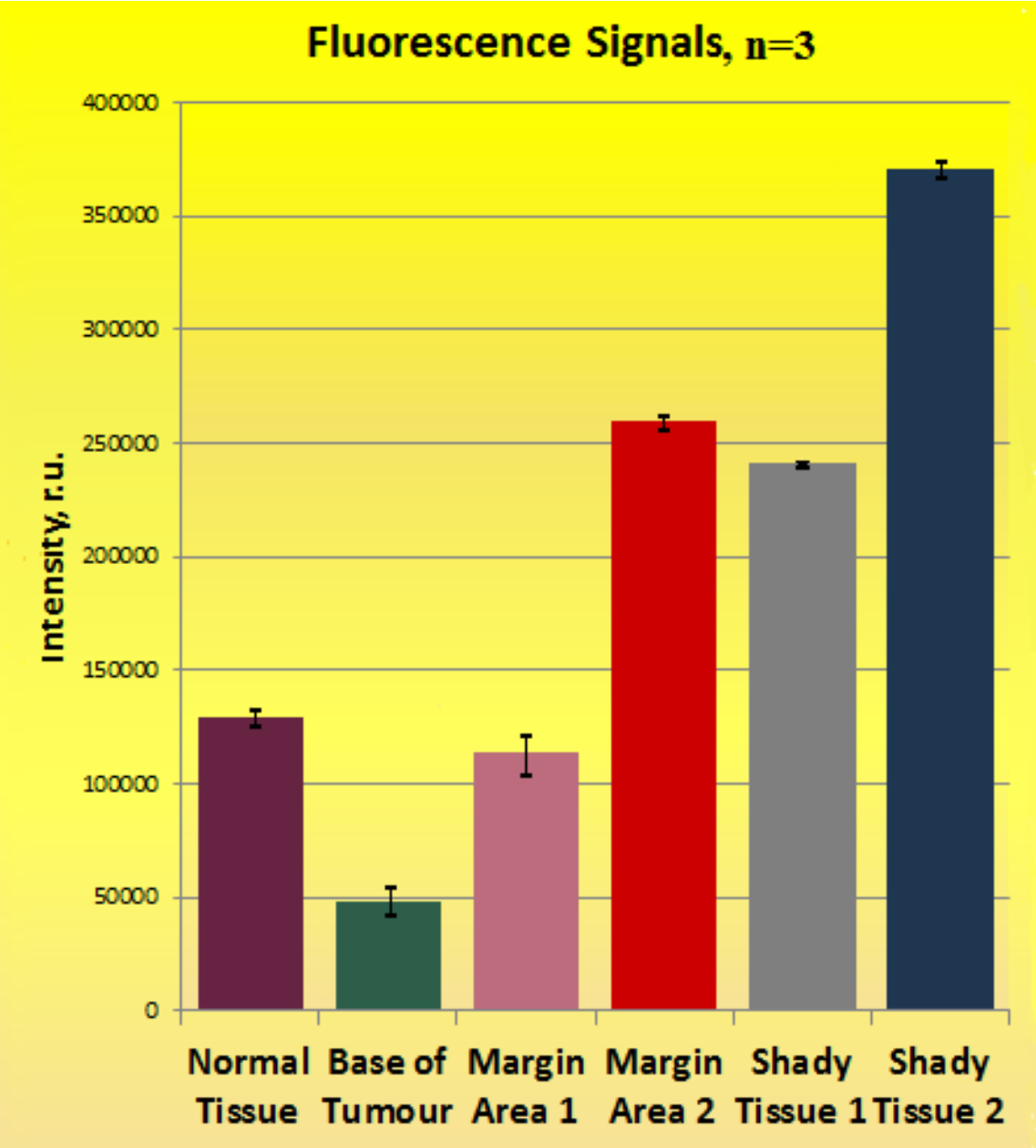

Figure 5.1 *Fluorescence intensities from 6 different parts of bladder tissue.*

Contrary to the fluorescent signal, the back-scattered laser signal was higher for the normal tissue than for pathological ones, except for the first shady area (Fig. 5.2). These values indicate the increase of the light absorption at the wavelength of 632.8 nm with the tumour formation. The minimal back-scattered laser signal and the maximal difference from the normal tissue were observed in the case of the tumour base. According to the analysis of the backscattered laser signal, the quantitative differences in signal intensities between

neoplastic and normal tissues, and thereafter the degree of the tissue changes, could be estimated. However, the specificity of these changes could not be defined.

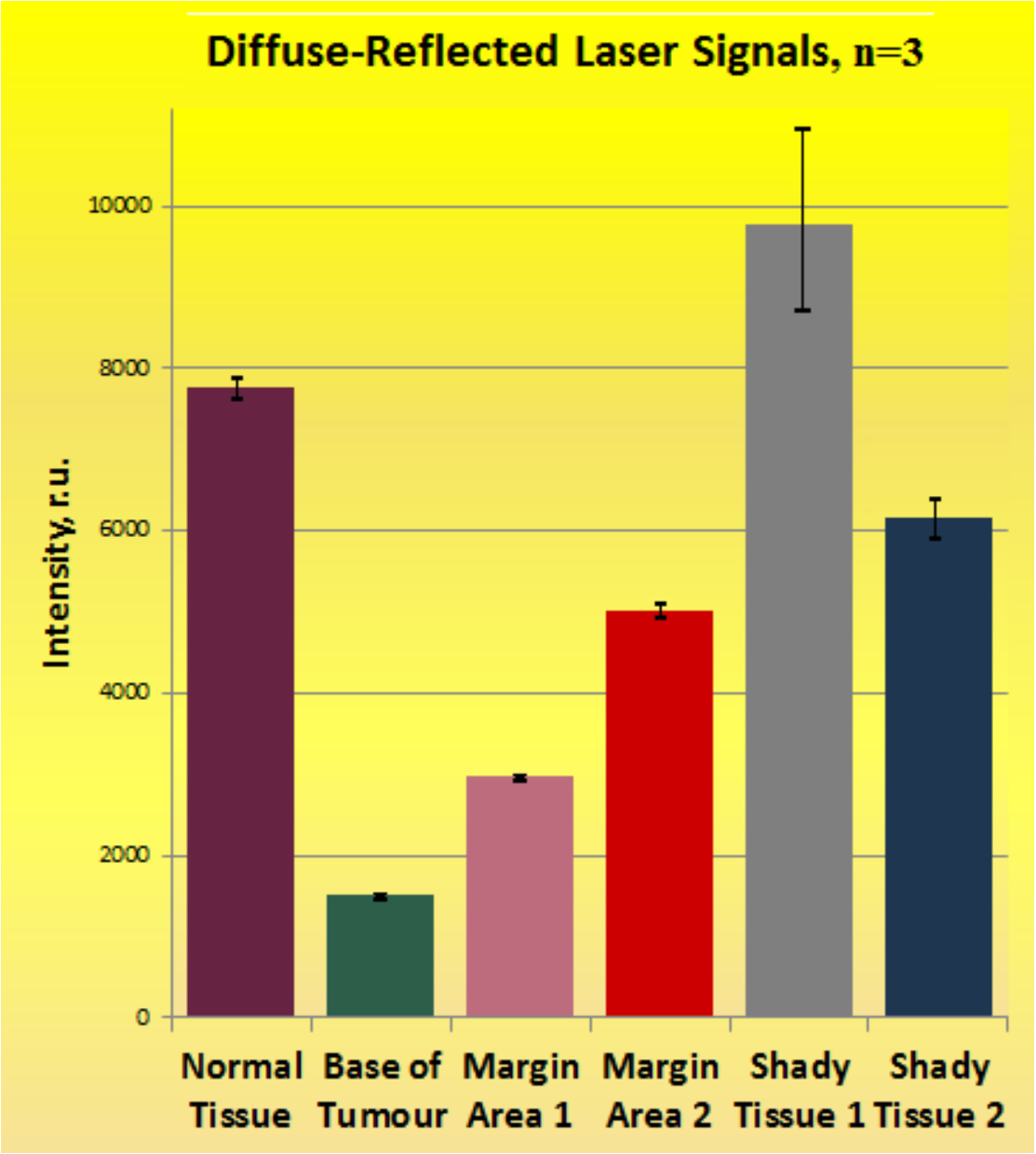

Figure 5.2 *Intensities of the back-scattered laser light from different parts of the bladder tissue.*

The mean intensity values of the backscattered laser and fluorescence signals for the six different areas of the bladder and their ratio to the "normal" signal are presented in the Table 6.

Analysed signal	Parameter	Normal tissue	Base of tumour	Margin area 1	Margin area 2	Shady tissue 1	Shady tissue 2
Back-scattered laser signal	Mean value, r.u.	7783	1527	2990	5023	9767	6170
	Ratio to normal tissue	1	0.2	0.38	0.65	1.22	0.79
Back-scattered fluorescent signal	Mean value, r.u.	129667	48000	114000	259667	241667	370333
	Ratio to normal tissue	1	0.37	0.88	2	1.84	2.86

Table 6 *Intensity measurements of fluorescent and laser back-scattered light from tissues of different states.*

Fig. 5.3 shows a comparison of the intensity values of back reflected laser and fluorescence signals related to the intensities of the signals measured for the normal tissue. Despite the fact that the differences in the DR laser signals are visible between all six tissue types, the measurement sensitivity of the back-scattered laser signal intensity is lower than of the fluorescence signal intensity, which was also noted previously, in the experimental studies (see Section 2.4). In the case of the margin area 1 of the tumour, the laser signal showed similar values with the signal from the large focus of the transitional cell carcinoma of the bladder tissue, unlike the fluorescent signal, which is similar to the signal from the normal tissue. In the case of the shady tissue 1, on the contrary, the fluorescence signal showed larger differences in the intensity values for the normal tissue than the laser signal, which was slightly larger than the normal. These results reveal the necessity to combine several complementary diagnostic techniques based on single-mode light excitation.

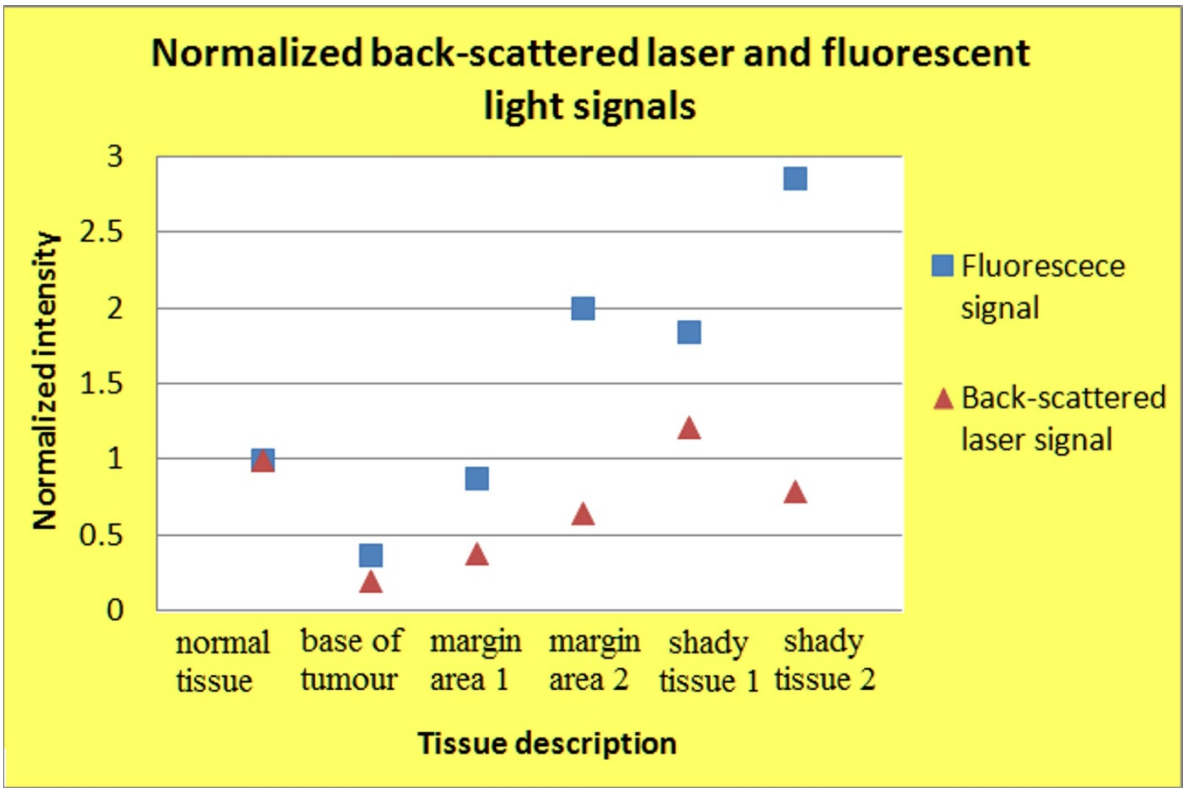

Figure 5.3 *Comparison of the fluorescent and laser back-scattered light from different parts of the bladder tissue.*

5.4 Multi-Wavelengths Mathematical Study

At pre-cancer and early-staged cancer formations, determination of tissue specificity and *in vivo* non-invasive diagnostics efficiency are usually limited by similarities and complexity of different pathologies. Besides, in the case of the inflammatory tissue, the absorption at the certain wavelengths can grow due to the oedemal concentration of the oxyhaemoglobin (see Section 1.2.2 and Fig. 2.13), which can be taken as a sign of dysplastic tissue and vice versa. In order to avoid such kind of misinterpretation of the measurements, the results of the DR laser light analysis have to be compared for various excitation wavelengths. Previously, multiwavelength studies were applied for different tissues and techniques: autofluorescence spectroscopy for bladder neoplasm detection [1], diffuse-reflectance spectroscopy analysis of brain tissue [2], light scattering spectroscopy on the corneal tissue [3], and spectroscopy and integrating sphere measurements on liver tissue samples [4].

In our study, the multiwavelength mathematical analysis was made for the bladder models characterizing by optical parameters for five tissue states, described in the Section 3.5.2. The analysis of the wavelength dependence of the tissue scattering coefficients was performed in a MathCAD program with the use of Mie calculations (see Section 3.5.2). As shown in Fig. 5.4, raising or lowering character of the scattering coefficient curve as a function of the wavelength for 5 different bladder states is caused by each particular tissue change at a cellular level. As the calculations were performed by the electromagnetic wave theory, the analysis of the absorption changes (tissue state type III) was restricted. Thus, only the imaginary part of the absorption coefficient was taken into consideration, which did not influence significantly on the scattering coefficient values. Thereafter, the scattering coefficient values for the normal tissue (tissue state type I beige curve) and for the tissue with higher absorption (light blue curve) show a similar character (see Fig. 5.4).

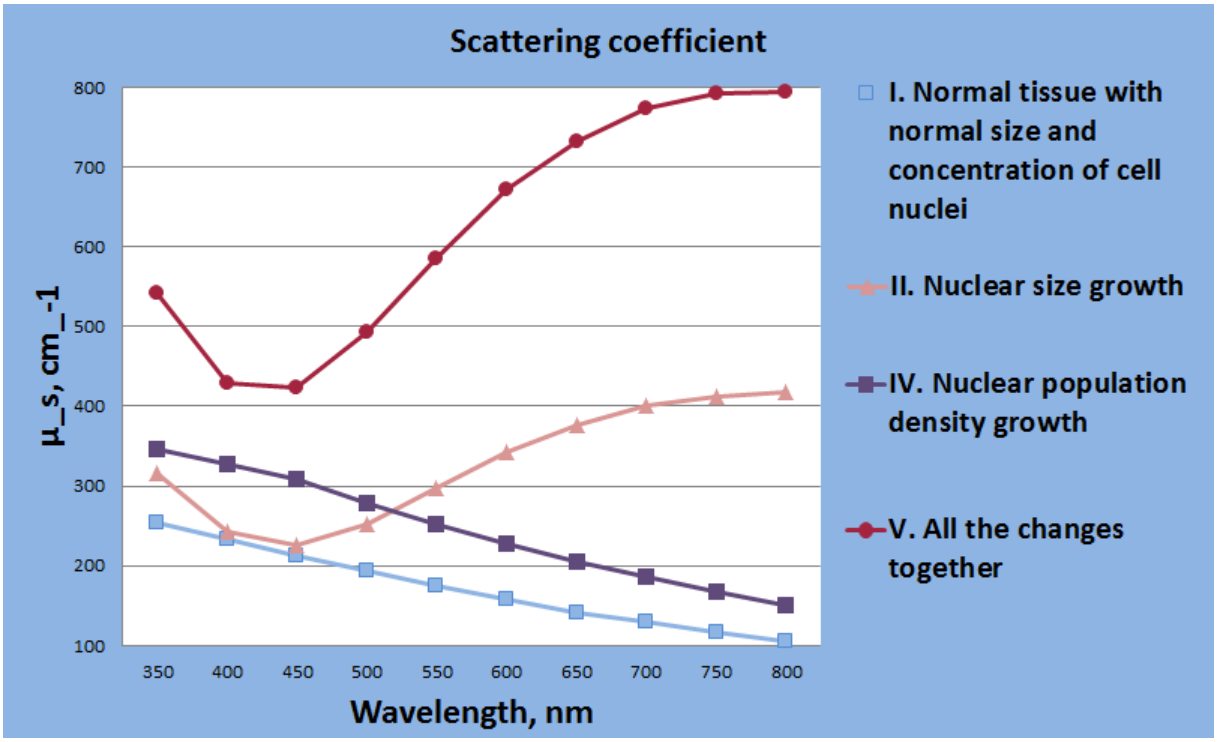

Figure 5.4 *Dependence of scattering coefficient on the wavelength calculated by the Mie theory for five different bladder tissue types.*

Increase in scatterers (nuclei) number (tissue state type IV) did not change the lowering character of the wavelength dependence of the scattering coefficient in comparison to the normal tissue state. However, the values of the scattering coefficients of the tissues with increased nuclei number were higher than those for the normal tissue. On the contrary, in the

case of nuclear size doubling from 5 µm to 10 µm (tissue state type II) the behaviour of the curve of scattering coefficient dependence on the wavelength shows significant differences to compare with the curve for the normal tissue (type I). This curves show contrasting behaviour in the range from 450 nm to 800 nm, which can be taken as a basis for characterising the internal changes of the tissue at the cellular level. Thus, the increase in scattering coefficient values with the wavelength (starting from 450 nm) indicates an increase in the nuclear size. Such scattering coefficient increase is reflected in the DR signal by the growth of the laser spot area on the tissue surface (see Sections 3.5.2.3 and 4.4.2).

5.5 Conclusion

The clinical analysis of the DR laser and fluorescent light showed that the method can be *in vivo* applied for detection of the tissue differences. It was also found that the DR light responses to the tissue changes can be well-detected, however the specificity of these changes cannot be determined. On that reason, the mathematical studies of multi-wavelengths mode of the DR-analysis method were performed. They revealed that almost not-differing signals from different tissues at one wavelength (for example, for the normal state (type I), and the nuclear size increase (type II) at the wavelength of 450 nm), can show a big difference at another wavelength (for example, at 650 nm). In the same time, for one tissue type, the DR signal can increase with the wavelength (for the tissue types II and V), while decreasing for another type (for the tissue types I, III, and IV). The totality of these two kinds of DR signal behaviour can potentially allow to determine the particular character and type of the changes, arisen in tissue.

References:

[1] Koenig; Frank McGovern; Francis J. Schomacker; Kevin T.” Methods and apparatus for distinguishing inflamed and tumorous bladder tissue”, US Patent number US6289236B1, 2001.

[2] Kawauchi S., S. Sato, H. Ooigawa, H. Nawashiro, K. Shima, and M. Kikuchi, Correlation between light scattering and reduction level of cytochrome oxidase in perfused brains of rats, Vol. 2 Track 08, p. 1281, at IFMBE Proceedings S. I. Kim and T. S. Suh (eds.), World Congress on Medical Physics and Biomedical Engineering, Vol. 14/2, 2006.

[3] Kim KB, Shanyfelt LM, Hahn DW.; Analysis of dense-medium light scattering with applications to corneal tissue: experiments and Monte Carlo simulations, J Opt Soc Am A Opt Image Sci Vis., 23(1):9-21, 2006.

[4] Nilsson A.M. K., Christian Sturesson, David L. Liu, and Stefan Andersson-Engels, Changes in spectral shape of tissue optical properties in conjunction with laser-induced thermotherapy, Appl. Opt. Vol. 37, No. 7, pp. 1256-1267, 1998.

6

CHAPTER

Perspectives and Conclusion

6.1 Conclusion

6.2 Special Features of the Diffuse-Reflectance Light Diagnosis and Possible Problems

6.3 Future Prospects

"Science never solves a problem without creating ten more."

G. B. Shaw

6.1 Conclusion

One of the main objectives of the presented work was the DR light analysis for detecting pre-cancerous and early-stage cancerous differences occurring in bladder, by means of determining the changes of optical scattering and absorption tissue properties. The sensitivity tests of the presented method on the phantoms with different scatterers sizes in the first layers, allowed to reveal that the method is suitable for detecting of tissue changes on cellular and intercellular level. It was revealed that the introduced image analysis algorithms can allow the data processing in a real time mode.

The analysis of light distribution at the surface of multi-layered phantoms with different scattering and absorption properties showed that the changes in the optical properties lead to increase or decrease of the DR light spot area. Such surface light responses on the micro changes appeared to be useful for improving the diagnostic analysis of tissue state. It was also determined, that the presented method is capable of detection of the photosensitizer accumulation.

The calculation results of Mie simulations allowed to obtain the optical parameters of three-layered biological media (the phantoms), and of bladder tissues at different states. These parameters served as inputs for the Monte Carlo simulations, which provided us with the DR light distribution matrices. The results of the mathematical modelling showed positive correlations with the experimental studies. By both, experimental and simulation studies, it was revealed that the difference in the DR signal between the media with normal absorption properties, sizes and concentration of the scatterers, and the media with increased scatterers sizes, or absorption, or all the changes together, can be well-detected by the presented method. However, the changes in the population density were less detectable.

The clinical studies showed that the analysis of the DR light signals can be non-invasively *in vivo* applicable for bladder tissues, thus the technique does not affect on natural dynamics of internal biological processes. It was found that the DR signals appear different for different tissue states, however, they cannot be uniquely interpreted. Nevertheless, the mathematical estimations revealed that the multi-wavelength excitation mode furthers the

discriminative analysis of the DR signals, and is potentially capable to characterize the DR light changes according to tissue changes at pre-cancer or cancer neoplasms.

The present study showed that not only interferometric light measurements can provide useful information on the tissue state (like the one, forming a base of the OCT technique), but also the measurements of non-polarized back-scattered laser light. Back-scattered light, distributed on the surface, reflects unique tissue properties at the cellular level, which simplifies the diagnostic instrumentation. Besides, the method of the surface DR light analysis does not require deep light penetration depth, as the initial cancerous neoplasms appear mostly in the top epithelial layer (of several hundred microns thick) of the urinary bladder. Moreover, the shorter wavelengths (of blue or green ranges) can allow to reduce the background DR noise signal. Nevertheless, the clinical studies showed that the wavelengths of a red range appear also suitable for bladder cancer diagnosis.

Finally, in order to resume, we presented following conclusions of this thesis:

- The presented method or the DR light analysis is sensible enough to be applicable for detection of bladder cancerous and pre-cancerous neoplasms;
- The presented diagnostic technique is applicable at *in vivo* form;
- The method does not require high laser power (the laser output power (for the visible wavelengths range) of 15 mW (up to 300 mW) is enough);
- The method does not require the photosensitizer agents application, nevertheless it can be used for fluorescence analysis without the use of any additional devices;
- The presented algorithms of mathematical simulations can be applied for forward problem solutions for DR light matrices construction. They can also be potentially used in an inverse form for interpreting the surface light distributions, and for obtaining tissue scattering and absorption parameters;
- The presented method showed higher sensibility to fluorescence measurements than to the spectroscopic or imaging methods of DR light analysis;
- Application of the method at a multi-wavelength excitation mode can potentially characterize each kind of tissue changes, thus it can be helpful for raising the specificity of bladder diagnosis at early-stages of cancer and pre-cancer formations;

6.2 Special Features of the Diffuse-Reflectance Light Diagnosis and Possible Problems

Some points of mathematical modelling have to be discussed for avoiding misunderstanding of interpretation errors when using the DR light analysis. Due to a big variety of the scattering and absorption tissue optical parameters given in literature (scattering coefficient, anisotropy factor, absorption coefficient, refractive indices, and sizes and shapes of the scatterers), the results of the mathematical modelling, can differ from one simulation to another. Globally such variations do not influence much the final result of determination of differences in the modelled surface light distributions, as the values of the DR signals should be normalised by a "normal" signal (or compared with it). Thereafter, the basic idea of the "markers" detection (of the changes in scatterers size and density, and absorption properties) does not change, and the method can be applied to different tissues and patents. The variations in the optical parameters are rather important for measurement calibrations.

Moreover, there is a specific feature of the imaging method of the DR light analysis: the technique should be applied at the plane surface. This constraint is due to necessity of counting and comparing the DR light spot areas, which is impracticable for the fold- or tubular- shaped organ surfaces. However, the diminution of the laser illuminating spot diameter, leading to decrease in under investigation area, allow to obtain more accurate and easier-to-process results by our method.

6.3 Future prospects

The analytical method for DR light analysis, presented in this thesis, was addressed to the bladder diagnosis, however it can be rearranged for diagnosis of other internal and external organs, according to their structure and peculiarities of tumour formation.

After being fitted and calibrated for clinical or experimental measurements, the presented mathematical method may be used at inverse form for non-invasive determination of the optical parameters of the urinary bladder wall.

The analytical study and clinical application of the method of surface diffuse-reflected light analysis at the multi-wavelength form is a voluminous work which still needs routine experimental investigations. However, the mathematical estimations revealed that such multi-wavelength measurements can be useful for diagnosis of pre-cancerous bladder states by obtaining more precise information on tissue micro changes afterwards the analysis of the optical parameters from the DR light signals.

APPENDIX

Program for Calculation of Scattering Parameters for “Coated” Spheres in MathCAD software.

INPUT DATA:

n1:= %% n1- index of refraction of a sphere (nucleus)

n2:= %% n2- index of refraction of a coat (cell)

n:= %% n- index of refraction of membrane/extracellular fluid

λ_vac:=

$\lambda\_med := \frac{\lambda\_vac}{n}$

$k = \frac{2\pi}{\lambda}$ %% k-const for all, (k=2π/λ), 1/μm

a:= %% a, b - radii of a sphere and of a coat, μm

b:=

$w1 := \pi a^2$

$w2 := \pi b^2$

$x := ka$ %% x, y - size parameters

$y := kb$

$m1 := \frac{n1}{n2}$

$m2 := \frac{n2}{n}$

$z1 := m1x$

$z2 := m2x$

$z3 := m2y$

ρ:= %% spheres per μm^3

ALGORITHM:

$$n\_max := \mathrm{round}\left(y + 4\cdot y^{\frac{1}{3}} + 2\right)$$

$$n\_mm := n\_max - 1$$

n:=1..n_max o:=2..n_max

$$h1(n,y) := js(n,y) + i\,ys(n,y)$$

$$A_n := \frac{(m2)^2\,js(n,z2)\cdot\left[\frac{d}{dz1}(z1\cdot js(n,z1))\right] - (m1)^2\cdot js(n,z1)\cdot\left[\frac{d}{dz2}(z2\cdot js(n,z2))\right]}{-(m2)^2\cdot ys(n,z2)\cdot\left[\frac{d}{dz1}(z1\cdot js(n,z1))\right] + \left(m1^2\right)\cdot js(n,z1)\cdot\left[\frac{d}{dz2}[(z2)\cdot ys(n,z2)]\right]}$$

$$B_n := \frac{\left[js(n,z1)\cdot\left[\frac{d}{dz2}(z2\cdot js(n,z2))\right] - js(n,z2)\cdot\left[\frac{d}{dz1}(z1\cdot js(n,z1))\right]\right]}{-js(n,z1)\cdot\left[\frac{d}{dz2}(z2\cdot ys(n,z2))\right] + ys(n,z2)\cdot\left[\frac{d}{dz1}(z1\cdot js(n,z1))\right]}$$

$$a_n := \frac{js(n,y)\cdot\left[\frac{d}{dz3}(z3\cdot js(n,z3)) + A_n\frac{d}{dz3}[(z3)\cdot ys(n,z3)]\right] - (m2)^2\cdot\left[\frac{d}{dy}(y\cdot js(n,y))\right]\cdot\left(js(n,z3) + A_n\cdot ys(n,z3)\right)}{h1(n,y)\cdot\left[\frac{d}{dz3}(z3\cdot js(n,z3)) + A_n\frac{d}{dz3}[(z3)\cdot ys(n,z3)]\right] - (m2)^2\cdot\left[\frac{d}{dy}(y\cdot h1(n,y))\right]\cdot\left(js(n,z3) + A_n\cdot ys(n,z3)\right)}$$

$$b_n := \frac{js(n,y)\cdot\left[\frac{d}{dz3}(z3\cdot js(n,z3)) + B_n\frac{d}{dz3}(z3\cdot ys(n,z3))\right] - \left[\frac{d}{dy}(y\cdot js(n,y))\right]\cdot\left(js(n,z3) + B_n\cdot ys(n,z3)\right)}{h1(n,y)\cdot\left[\frac{d}{dz3}(z3\cdot js(n,z3)) + B_n\frac{d}{dz3}(z3\cdot ys(n,z3))\right] - \left[\frac{d}{dy}(y\cdot h1(n,y))\right]\cdot\left(js(n,z3) + B_n\cdot ys(n,z3)\right)}$$

$$Q1\_sca := \left(\frac{2}{x^2}\right)\cdot\sum_{n=1}^{n\_max}\left[(2\cdot n + 1)\cdot\left[\left(|a_n|\right)^2 + \left(|b_n|\right)^2\right]\right]$$

$$Q2\_sca := \left(\frac{2}{y^2}\right)\cdot\sum_{n=1}^{n\_max}\left[(2\cdot n+1)\cdot\left[\left(\left|a_n\right|\right)^2+\left(\left|b_n\right|\right)^2\right]\right]$$

$$Q1\_2sca(n) := \left(\frac{2}{x^2}\right)\cdot\left[(2\cdot n+1)\cdot\left[\left(\left|a_n\right|\right)^2+\left(\left|b_n\right|\right)^2\right]\right]$$

$$Q2\_2sca(n) := \left(\frac{2}{y^2}\right)\cdot\left[(2\cdot n+1)\cdot\left[\left(\left|a_n\right|\right)^2+\left(\left|b_n\right|\right)^2\right]\right]$$

$\sigma 1\_sca := Q1\_sca\cdot w1$

%% σ_sca- scattering cross- section

$\sigma 2\_sca := Q2\_sca\cdot w2$

$\mu 1\_s := \rho\cdot\sigma 1\_sca\cdot 10000$ %% scattering coefficient [cm-1]

$$Q1\_ext := \frac{2\cdot\sum_{n=1}^{n\_max}\left[(2\cdot n+1)\cdot Re\left(a_n+b_n\right)\right]}{x^2}$$

$$Q2\_ext := \frac{2\cdot\sum_{n=1}^{n\_max}\left[(2\cdot n+1)\cdot Re\left(a_n+b_n\right)\right]}{y^2}$$

$\sigma 1\_ext := Q1\_ext\cdot w1$ %% σ_ext- extinction cross- section

$\mu 1\_t := \rho\cdot\sigma 1\_ext\cdot 10000$ %% extinction coefficient [cm-1]

$\mu 1\_a := \mu 1\_t - \mu 1\_s$ %% absorption coefficient [cm-1]

$$A_{n+1} := \frac{(m2)^2 \cdot js(n+1,z2) \cdot \left[\frac{d}{d\,z1}(z1 \cdot js(n+1,z1))\right] - (m1)^2 \cdot js(n+1,z1) \cdot \left[\frac{d}{d\,z2}(z2 \cdot js(n+1,z2))\right]}{-(m2)^2 \cdot ys(n+1,z2) \cdot \left[\frac{d}{d\,z1}(z1 \cdot js(n+1,z1))\right] - \left(m1^2\right) \cdot js(n+1,z1) \cdot \left[\frac{d}{d\,z2}[(-z2) \cdot ys(n+1,z2)]\right]}$$

$$B_{n+1} := \frac{js(n+1,z1) \cdot \left[\frac{d}{d\,z2}(z2 \cdot js(n+1,z2))\right] - js(n+1,z2) \cdot \left[\frac{d}{d\,z1}(z1 \cdot js(n+1,z1))\right]}{js(n+1,z1) \cdot \left[\frac{d}{d\,z2}[(-z2) \cdot ys(n+1,z2)]\right] + (ys(n+1,z2)) \cdot \left[\frac{d}{d\,z1}(z1 \cdot js(n+1,z1))\right]}$$

$$a_{n+1} := \frac{js(n+1,y) \cdot \left[\frac{d}{d\,z3}(z3 \cdot js(n+1,z3)) - A_{n+1} \frac{d}{d\,z3}[(-z3) \cdot ys(n+1,z3)]\right] - (m2)^2 \cdot \frac{d}{dy}(y \cdot js(n+1,y)) \cdot \left(js(n+1,z3) + A_{n+1} \cdot ys(n+1,z3)\right)}{h1(n+1,y) \cdot \left[\frac{d}{d\,z3}(z3 \cdot js(n+1,z3)) - A_{n+1} \frac{d}{d\,z3}[(-z3) \cdot ys(n+1,z3)]\right] - (m2)^2 \cdot \frac{d}{dy}(y \cdot h1(n+1,y)) \cdot \left(js(n+1,z3) + A_{n+1} \cdot ys(n+1,z3)\right)}$$

$$b_{n+1} := \frac{js(n+1,y) \cdot \left[\frac{d}{d\,z3}(z3 \cdot js(n+1,z3)) - B_{n+1} \frac{d}{d\,z3}[(-z3) \cdot ys(n+1,z3)]\right] - \left[\frac{d}{dy}(y \cdot js(n+1,y))\right] \cdot \left(js(n+1,z3) + B_{n+1} \cdot ys(n+1,z3)\right)}{h1(n+1,y) \cdot \left[\frac{d}{d\,z3}(z3 \cdot js(n+1,z3)) - B_{n+1} \frac{d}{d\,z3}[(-z3) \cdot ys(n+1,z3)]\right] - \left[\frac{d}{dy}(y \cdot h1(n+1,y))\right] \cdot \left(js(n+1,z3) + B_{n+1} \cdot ys(n+1,z3)\right)}$$

$\theta := 0..\pi$

$$Q1\_cos\theta := \left(\frac{4}{x^2}\right) \cdot \left[\sum_{n=1}^{n\_max} \left[\left[n \cdot \frac{(n+2)}{n+1}\right] \cdot Re\left[a_n \cdot \left(\bar{a}\right)_{n+1} + b_n \cdot \left(\bar{b}\right)_{n+1}\right]\right] + \sum_{n=1}^{n\_max} \left[\left[\frac{(2 \cdot n+1)}{n \cdot (n+1)}\right] \cdot Re\left[a_n \cdot \left(\bar{b}\right)_n\right]\right]\right]$$

$$Q2\_cos\theta := \left(\frac{4}{y^2}\right) \cdot \left[\sum_{n=1}^{n\_max} \left[\left[n \cdot \frac{(n+2)}{n+1}\right] \cdot Re\left[a_n \cdot \left(\bar{a}\right)_{n+1} + b_n \cdot \left(\bar{b}\right)_{n+1}\right]\right] + \sum_{n=1}^{n\_max} \left[\left[\frac{(2 \cdot n+1)}{n \cdot (n+1)}\right] \cdot Re\left[a_n \cdot \left(\bar{b}\right)_n\right]\right]\right]$$

$$Q1\_2cos(\theta) := \left(\frac{4}{x^2}\right) \cdot \left[\left[\left[n \cdot \frac{(n+2)}{n+1}\right] \cdot Re\left[a_n \cdot \left(\bar{a}\right)_{n+1} + b_n \cdot \left(\bar{b}\right)_{n+1}\right]\right] + \left[\left[\frac{(2 \cdot n+1)}{n \cdot (n+1)}\right] \cdot Re\left[a_n \cdot \left(\bar{b}\right)_n\right]\right]\right]$$

$$Q2\_2cos(\theta) := \left(\frac{4}{y^2}\right) \cdot \left[\left[\left[n \cdot \frac{(n+2)}{n+1}\right] \cdot Re\left[a_n \cdot \left(\bar{a}\right)_{n+1} + b_n \cdot \left(\bar{b}\right)_{n+1}\right]\right] + \left[\left[\frac{(2 \cdot n+1)}{n \cdot (n+1)}\right] \cdot Re\left[a_n \cdot \left(\bar{b}\right)_n\right]\right]\right]$$

g 1:= $\frac{Q1\_cos}{Q1\_sca}$ =

%% average cosine

o := $\sum_{n=1}^{n\_max}\left[(2\cdot n+1)\cdot(-1)^{n}\cdot\left(a_{n}-b_{n}\right)\right]$

o _ 1:= |o| :

Q 1 _: $\left(\frac{1}{x^{2}}\right)\cdot(o\_)^{2}$:

%% Q_b- backscattering efficiency

Q 2 _: $\left(\frac{1}{y^{2}}\right)\cdot(o\_)^{2}$:

σ1 _ b:= w 1 Q 1 _ b :

%% σ_b- backscattering cross- section, [μm^2]

g _ : $\frac{Q\ 1\ \_}{Q\ 1\ \_}$:

Q 1 _ a b= Q 1 _ e x Q 1 _ s :

Q 2 _ a b= Q 2 _ e x Q 2 _ s :

OUTPUT PARAMETERS:

λ=

n_max=

μ1_s= %% scattering coefficient [cm-1]

Q1_b=

%% backscattering efficiency

Q2_b=

σ1_b= %% backscattering cross-section, [μm^2]

g1= %% average cosine

Q1_sca=

%% scattering efficiency

Q2_sca=

μ1_t= %% extinction coefficient, [cm-1]

μ1_a= %% absorption coefficient, [cm-1]

σ1_sca= %% scattering cross-section, [μm^2]

Q1_ext=

%% extinction efficiency

Q2_ext=

σ1_ext= %% extinction cross-section

Summary

Diffuse Reflectance Endoscopic Imaging for Bladder Early-Stage Cancer and Pre-Cancer Diagnosis: Instrumentation, Modelling and Experimental Validation

The present thesis aimed to evaluate the performance of non-invasive optical method for bladder pre- and early- cancer detection by means of diffuse-reflected laser light analysis. The analysis of light distribution at the surface of multi-layered bladder phantoms with different scattering and absorption properties showed that the changes in the optical properties lead to increase or decrease of the diffuse-reflected light spot area, detectable by a video camera. It was also determined, that the presented method is capable of detection of the photosensitizer accumulation, and can be applied for both (diffuse-reflected laser and fluorescence) studies simultaneously. The calculations for spherical and "coated"-spherical tissue scatterers, based on the electromagnetic wave theory, allowed for obtaining optical parameters of three-layered biological phantoms and of bladder tissues at different states. These parameters served as inputs for Monte Carlo simulations, which provided us with matrices of diffuse-reflected light distributions. The study showed that the measurements of non-polarized back-scattered laser light can provide useful information on the tissue state.

Keywords: optical analysis, light scattering, bladder cancer, Mie scattering, Monte Carlo modeling, fluorescence analysis.

Résumé

Imagerie Endoscopique de Réflectance Diffuse pour le Diagnostic des Pré-Cancers et Cancers Précoces de la Vessie: Instrumentation, Modélisation et Validation Expérimentale

L'objectif de cette thèse est d'évaluer les performances d'une méthode d'imagerie optique non-invasive pour la détection de précancers et cancers précoces de la vessie, à l'aide d'une analyse de lumière laser rétro-diffusée. L'analyse de la distribution spatiale de la lumière à la surface de fantômes multi-couches imitant l'épithelium de vessie avec différentes propriétés d'absorption et de diffusion nous a permis de montrer les modifications de ces propriétés optiques entraînent des changements de la taille de la surface du spot de lumière rétro-diffusée, mesurables par une caméra vidéo. La méthode développée est également sensible à l'accumulation d'un photosensibilisateur et est applicable aussi bien pour des études en réflectance diffuse qu'en fluorescence induite. Les paramètres optiques des fantômes synthétiques tri-couches imitant différents états des épithéliums de vessie ont été calculés à partir de la théorie des ondes électromagnétiques appliquée aux diffuseurs sphériques sans et avec une couche. Ces paramètres ont servi comme entrées aux simulations de Monte Carlo qui ont permis d'obtenir les matrices des distributions d'intensité de réflectance diffuse. Notre étude démontre que les mesures en imagerie de réflectance diffuse non-polarisée permettent de fournir des informations utiles au diagnostic tissulaire.

Mots clés: analyse optique, diffusion de lumière, cancer de vessie, diffusion de Mie, simulations Monte Carlo, analyse de fluorescence.